Extended X-ray Emission in Spiral Galaxy Disks

Richard Owen

Supervisor:
Robert Warwick

Thesis to be submitted for the degree of

Doctor of Philosophy

at the University of Leicester.

X-ray & Observational Astronomy Group

Department of Physics and Astronomy

University of Leicester

November 3, 2009

Declaration

I hereby declare that no part of this thesis has been previously submitted to this or any other University as part of the requirement for a higher degree. The work described herein was conducted by the undersigned, except for contributions from colleagues as acknowledged in the text.

Richard Owen.

November 2009.

ABSTRACT

We have studied the extended X-ray emission observed in the disks of seven nearby face-on spiral galaxies using *XMM-Newton* archival observations. Using a novel technique to remove the bulk of the contamination from bright X-ray point sources, we have isolated a residual disk component in each galaxy, comprising diffuse gas plus the integrated population of faint point sources. We have found soft X-ray emission from this component to be strongly correlated with FUV emission, unambiguously establishing a close link with recent star formation.

We have found the residual X-ray/star formation rate (SFR) ratio across our sample to range from $1-5\times10^{39}$ erg s^{-1} ($\mathrm{M}_{\odot}$ yr^{-1})$^{-1}$, with the ratio highest in regions with the highest SFR. This is consistent with the models of Ranalli et al. (2003), and matches the predicted X-ray emission ≈ 10 Myr after an extended burst of star formation.

Our spectral analysis of the residual disk components indicates that a two-temperature thermal plasma fits the data well, with derived temperatures of 0.2 keV and 0.65 keV. This is consistent with previously derived results for spiral and starburst galaxies (*e.g.* Fraternali et al. 2002). We have shown the emission to be well modelled by a clumpy thin-disk distribution, with bubbles of hot gas and collections of faint point sources tracing the galactic spiral arms.

We have found the excised bright point source populations to be evenly divided between old and young sources with the exception of M33, where young sources dominate. We have derived the residual X-ray/mass ratio in the inner disk of this system to be 4×10^{28} erg s^{-1} $\mathrm{M}_{\odot}{}^{-1}$. This is 5-10 times higher than the equivalent ratio in low star formation rate systems (Revnivtsev et al. 2008), with the excess attributed to contributions from the young point source population and diffuse gas.

Our results have demonstrated a quantifiable link between diffuse X-ray emission and recent star formation in spiral galaxies. Further study is necessary to better constrain this relationship, in particular its dependence on the local environment.

Acknowledgements

I would like to thank all those who made the last four years of my life such an amazing and exciting experience. First of all to my supervisor Bob Warwick, thank you for your endless patience and encouragement. I truly appreciate the time you have spent helping me. We have done some great science together and I look forward to continuing to work with you in the years ahead. To Gordon Stewart and Steve Gurman, my thesis committee, many thanks for keeping me on track and for all your assistance. Throughout my time here, many friends and colleagues have given up their time to give useful advice. In particular, I would like to thank Andy, Jenny and Tim for their valuable contributions.

I have been very lucky to share offices with many wonderful people here. All of them were great fun to work with and very supportive in stressful times, especially when writing up! Mark, Cheryl, Simon, Kristiina, Phil, Evert, Klaas, Valentina and Yueheng, thank you for making my time at work so enjoyable. I thank my housemates for the past few years for helping to make life outside work so great as well: Ewan, Antonio, Eleonora, Megan, Richard, Tricia, Merel, Pawel and Oli.

To my friends here in Leicester and those who have moved on, I am profoundly grateful. From the Old Horse quiz to poker at Jay's, DVD nights and Friday pub trips, your company, friendship and support is invaluable to me. In no particular order, thanks to Dave, Lucy, Pete, Chris, Sophie, Pippa, Charly, Sean, Jay, Elizabeth, Nathan, Paul, Ann-Marie, Becks, Rhian and Amy.

Two teachers at school inspired me to pursue a career in science, and it is in no small part due to them that I have achieved this goal. I thank Mike Clugston and Paul Todd for starting me down this road.

Finally, and most importantly, my family. Their support and love at all times is beyond measure, and I would not be in this position without their encouragement and faith in me. This thesis is dedicated to them: my parents, my brother and sister, Martin and Sara, and my nieces, Rhiannon and Niamh. Thank you.

CONTENTS

LIST OF FIGURES

LIST OF TABLES

Chapter 1

Introduction

1.1 A Brief History of X-ray Astronomy

1.1.1 The Earliest X-ray detectors

The field of X-ray astronomy is still extremely young. Due to the absorption of X-ray radiation by the Earth's atmosphere, we are only able to observe X-ray emission from cosmic sources if the detector is above an altitude of ≈ 80 km, which was only achievable with the advancement of rocket technology at the end of World War II. The first flights to carry X-ray telescopes were conducted in 1948 using American V2 rockets. These carried crude detectors which consisted of photographic plates covered with beryllium filters, and only reached altitudes sufficient for carrying out measurements for a few minutes before returning to Earth. These first experiments detected X-rays produced in the Sun's corona. Over the next decade, several more rocket flights were made using similar detectors as well as geiger counters. The first detection of an X-ray source outside the Solar System was made by Giacconi in 1962, using a geiger counter attached to an Aerobee rocket. The source was unresolved and was in the constellation of Scorpius (Sco X-1). This came as a massive surprise since nearby stars, if they radiated with the same X-ray luminosity as the Sun, would be several orders of magnitude too faint to be detected. The X-ray flux from this source was calculated to be 10^3 times its optical flux, compared with a factor of 10^{-6} for the Sun. The same flight also detected the X-ray background for the first time. Many subsequent rocket and high altitude balloon flights detected more extra-solar X-ray sources, with

Bowyer et al. (1964) detecting pulsed X-ray emission from the centre of the Crab Nebula.

These discoveries marked the birth of X-ray astronomy, and plans were made to launch a "scanning satellite", which would not be constrained by the short time-scales of the rocket and balloon observations. These plans were realized in 1970 with the launch of *UHURU* (Giacconi et al. 1971), which detected 300 new X-ray sources with a spatial precision of up to $1'$ –$2'$, including supernovae, galaxies and quasars. This was the first observatory to carry out an all-sky survey in X-rays. The first sources with variable X-ray output were identified, with Her X-1 and Cen X-3 found to pulsate with periods of a few seconds (Schreier et al. 1972), with a slight modulation of this period over a period of a few days. These "pulsars" were found to be binary systems consisting of a neutron star and a main sequence star, the first neutron star X-ray binary systems discovered.

Over the next 5-10 years, several more satellites were launched to study X-ray sources, including *Ariel-5*, *SAS-3*, *OSO-8* and *HEAO-1*. The detectors on board spanned an energy range of 0.2 keV – 10 MeV, with spatial resolution comparable to *UHURU*. Bright point sources could typically be located to within $1 - 2'$, although extended emission regions could only be spatially resolved on a scale of $30'$ or more.

1.1.2 The next step: *Einstein* to *ROSAT*

A large step forward was made in 1978 with the launch of the first fully imaging X-ray telescope on board *Einstein* (Giacconi 1979). Using this telescope, the first morphological studies of extended sources such as supernova remnants (SNRs) with arcminute-scale spatial resolution became possible (*e.g.* Long & Helfand 1979; Mathewson et al. 1983), along with spectral analysis. The improved spatial resolution allowed identification of optical counterparts to these sources to be achieved with far greater certainty. The number of galaxies observed in X-rays increased from four to well over 100, and extended unresolved X-ray emission was observed from face-on galactic disks for the first time (Trinchieri et al. 1985; Palumbo et al. 1985; Trinchieri et al. 1988). Additionally, studies of X-ray binary systems in external galaxies found that they dominated the X-ray emission observed from the galaxy as a whole (Fabbiano et al. 1982; Stewart et al. 1982). The *EXOSAT* telescope (de Korte et al. 1981), launched in 1983, provided the first evidence for Quasi Periodic Oscillations (QPOs) in X-ray binary systems (van der Klis 1989). The Japanese *Ginga* satellite (1987; Tsunemi et al. 1989) discovered transient black hole candidates (Tsunemi et al. 1989) and cyclotron features in X-ray pulsars (*e.g.* Makishima et al. 1990).

The next stage in X-ray astronomy came with the *Röntgen Satellite* (*ROSAT*) in 1990 (Trümper 1991). This carried a wide-field camera with which the first all-sky survey was conducted in the soft 0.1–2.4 keV band. Through its 9 years of operation it catalogued more than 150,000 new sources, using an imaging capability 1000 times as sensitive as *UHURU*. Populations of X-ray binary sources in galaxies were detected to far lower flux limits than previous missions, and the improved spatial resolution of $\approx 15''$ allowed separation of the X-ray components present in such complex systems. Unambiguous evidence was found for the presence of diffuse hot X-ray emitting gas in several nearby face-on and edge-on spiral galaxies as well as the LMC and SMC (*e.g.* Pietsch & Truemper 1993; Vogler et al. 1996; Vogler & Pietsch 1996). *ASCA*, which launched in 1993 to replace *Ginga*, was the first X-ray telescope to operate using CCD detectors. This would become the standard for future missions.

1.1.3 The current observatories

There are four X-ray telescopes currently imaging the sky in soft X-rays: *Chandra* (Weisskopf et al. 2000), *XMM-Newton*, *Suzaku* (Bautz & Suzaku Team 2006) and the *Swift* X-ray Telescope (XRT) (Burrows et al. 2003), with the latter primarily intended for detection of gamma-ray burst X-ray afterglows. The comparative properties of these missions are shown in Table 1.1. All of these telescopes use CCDs to detect X-ray photons, with *Chandra* providing angular resolution of less than one arcsecond at low energy. This brings X-ray imaging capability far closer to that of optical and radio astronomy than any previous detectors. The angular resolution of *XMM-Newton* is on the scale of $5''$, whereas *Suzaku* and the *Swift* XRT have significantly poorer resolution.

The collecting area of *XMM-Newton* is significantly superior to that of *Chandra*. As a result, low surface brightness targets (such as areas of diffuse emission in galaxies) can be detected with significantly better signal-to-noise in *XMM-Newton* compared to *Chandra* for a given observation time. Additionally, the spectral resolution for the *XMM-Newton* detectors is superior to that of *Chandra*, especially at low energy. The large collecting area of *Suzaku* also allows detection of faint sources with good spectral resolution, although its spatial resolution is significantly worse than for the other telescopes.

These improvements in both spectral and spatial resolution over the previous generation of detectors have allowed significant progress to be made in the field. Populations of X-ray sources in galaxies have been identified as distant as the Virgo Cluster and it has become possible to successfully distinguish between these sources and the unresolved extended emission in the galaxy (Young et al. 2002). Several extensive surveys have been completed using both *XMM* and *Chandra*, covering both wide angle studies and deep "pencil beam" observations. Examples of wide-angle surveys include the XMM Serendipitous Source Survey (Watson et al. 2009), which covers $360\mathrm{deg}^2$ of the sky with a median source flux (0.2–2 keV) of 5.8×10^{-15} erg cm^{-2} s^{-1}, and consists of 191,000 distinct source detections, and the *Chandra* ChaMPlane survey of Galactic source populations (Grindlay et al. 2005), covering an area of $23\mathrm{deg}^2$ to a depth of 1.3×10^{-15} erg cm^{-2} s^{-1} (0.5–8 keV). Examples of deep pencil beam surveys conducted include the *Chandra* Deep-Field South survey (CDF-S; Giacconi et al. 2001; Rosati et al. 2002), which covers a $20' \times 20'$ area to a flux limit of 5.5×10^{-17} erg cm^{-2} s^{-1} (0.5–2 keV), and the *XMM-Newton* Lockman Hole observation (Hasinger et al. 2001), which examines an area of $30' \times 30'$ to a limiting flux of 3.4×10^{-16} erg cm^{-2} s^{-1} (0.5–2 keV).

The main purpose of the work presented in this thesis is study of the morphological and spectral properties of the extended emission emanating from the disks of galaxies. In particular we focus on the detection of X-ray emission at relatively low surface brightness, for which we primarily rely on *XMM-Newton* data.

1.2 X-ray Emission and Absorption Mechanisms

High energy astrophysics involves the study of X-ray and γ-ray photons and cosmic ray particles. These reveal evidence of the highest-energy events occurring in the cosmos such as supernova explosions and emission by active galactic nuclei, as well as events where the acquired energy per nucleon or temperature of the system is extremely high. This latter class includes infall or accretion of matter onto a compact object, the interaction of relativistic particles with magnetic fields and emission from high-temperature plasmas. Through examination of X-ray spectra, it is possible to deduce the processes occurring and hence the nature of the systems producing this radiation (Seward & Charles 1995).

There are several main mechanisms for the emission and absorption of X-ray radiation in a cosmic setting, which can be divided into two main classes: continuum processes and line processes. Continuum emission processes include: *magneto-bremsstrahlung*, which includes cyclotron and synchrotron radiation (depending on the energy of the particles involved), *thermal bremsstrahlung*, *black-body radiation*

Table 1.1: Comparison of currently operating soft X-ray telescopes.

Detector (Instrument)	*Chandra* (ACIS-I)	*XMM-Newton* (pn)	*Suzaku* (XIS)	*Swift* (XRT)
Energy range (keV)	$0.4 - 10.0$	$0.2 - 15.0$	$0.2 - 12.0$	$0.2 - 10.0$
Effective area (cm^2 at 1.0keV)	385	1227	1600	110
Energy Resolution (eV at 1.0keV)	56	55	50	55
Angular Resolution (FWHM)	$1''$	$\sim 6''$	$\sim 1.5'$	$\sim 18''$
Field of View diameter	$17'$	$30'$	$19'$	$24'$

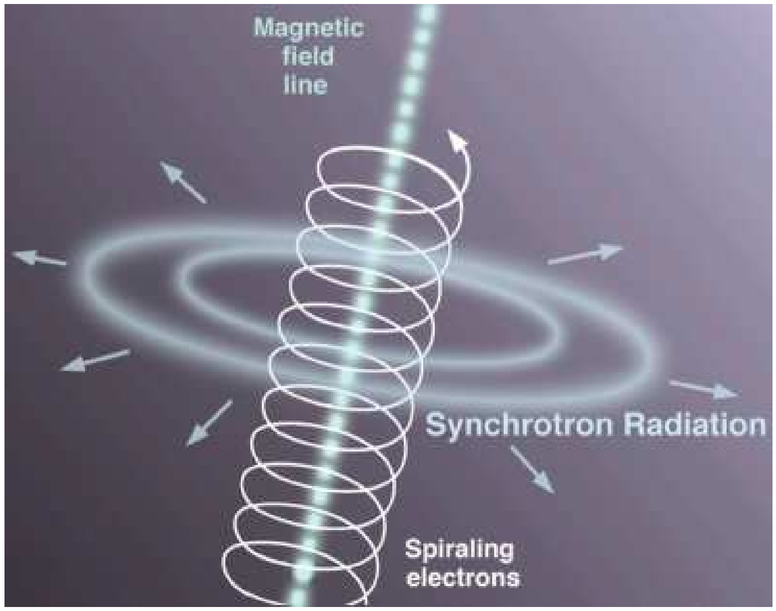

Figure 1.1: Illustration of synchrotron radiation produced by an ultrarelativistic electron accelerating in a magnetic field. Image courtesy of http://astronomyonline.org.

and *inverse Compton scattering*. *Photoelectric absorption* of X-ray photons along the line of sight is an example of a continuum absorption process. On the other hand, sharp spectral line features result from atomic processes such as ionization, recombination and de-excitation. In the following section, we describe these processes in detail and examine their impact on the X-ray spectral shape of sources.

1.2.1 Synchrotron and Cyclotron radiation

Bremsstrahlung, or "braking radiation" is produced by the acceleration of a charged particle in a direction perpendicular to its direction of motion. If an electron crosses a magnetic field, it will also experience a perpendicular force, leading to the emission of radiation. The electron follows a spiral path around the magnetic field with frequency dependent on the energy of the electron, its velocity relative to the magnetic field and the strength of the field (illustrated in Fig. 1.1). This is termed magneto-bremsstrahlung, or "magnetic braking radiation". The energy emitted by electrons travelling at ultrarelativistic speeds is termed synchrotron radiation, with that from slower-moving electrons termed cyclotron radiation.

The power radiated by a relativistic electron moving in a magnetic field is given by the following

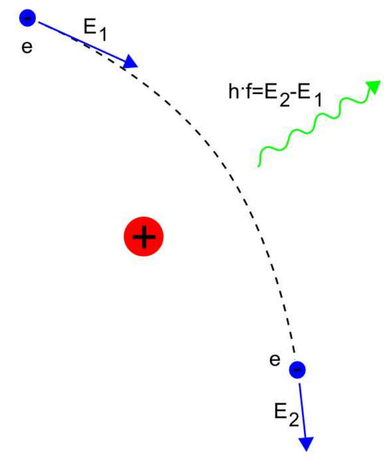

Figure 1.2: Illustration of bremsstrahlung radiation emitted by an electron accelerated in an electric field. Public Domain image courtesy of http://commons.wikimedia.org

equation for an isotropic distribution of electron velocities:

$$P_X \approx 1.1 \times 10^{-15}(E_e/m_0c^2)^2\beta^2\mathrm{B}^2 \ \ \mathrm{erg\,s^{-1}} \tag{1.1}$$

(Tucker 1977), where P is the power of the radiation produced, E_e amd m_0 are the electron energy (in keV) and rest mass, β is the electron's speed as a fraction of the speed of light and B is the magnitude of the magnetic field. In this case, the majority of the energy is radiated near the peak energy:

$$E_X \approx 6.6 \times 10^{-21}E_e^2\mathrm{B}\,\sin\alpha\;\mathrm{keV} \tag{1.2}$$

(Tucker 1977) where E_e is the electron energy in keV and α is the angle between the electron direction of motion and the magnetic field B. When the distribution of electron energies is a power law, the resulting radiation spectrum is also a power-law:

$$F(E) = AE^{-\alpha} \tag{1.3}$$

with index α=(β-1)/2, where β is the power law index of the electron energy distribution, A is a normalisation constant and E the energy of the photon. The spectrum of cyclotron radiation follows a similar profile, but the lower energy of the electrons makes a cyclotron spectral signal far more difficult to detect.

Due to the mechanism of energy release, the synchrotron radiation is expected to be highly polarised. Observation of a polarised jet emanating from the nucleus of M87 in optical light by Burbidge (1956) confirmed the presence of synchrotron radiation and hence an extremely strong magnetic field in the system.

1.2.2 Thermal Bremsstrahlung

When a gas is heated to temperatures above 10^5K ionization occurs, resulting in a combination of positive ions (which are largely protons) and free electrons. The spread in energy of these thermal electrons is well described by the Maxwell-Boltzmann distribution. As shown in Fig. 1.2, when an electron passes close to a positive ion, the electrostatic force between them accelerates the electron. As in the case of synchrotron radiation, this acceleration causes the electron to radiate energy. The energy of the photon released is dependent on the distance between the electron and the ion and the speed of the electron. For gas with a temperature above $\approx 10^6$K, the majority of photons produced are in the X-ray band. As the electrons have a thermal distribution of energies, the bremsstrahlung spectrum is also thermal with the following dependence on energy (E) and temperature (T) (Kaastra et al. 2008):

$$\epsilon_{ff} = AZ_{eff}^2 n_e n_i (kT)^{-1/2} g_{ff} e^{-E/kT} \tag{1.4}$$

where ϵ_{ff} is the number of photons emitted per unit volume, time and energy (or emissivity), Z_{eff} is the effective charge of the ion, n_e and n_i are the electron and ion densities and g_{ff} is the "Gaunt factor", which evolves slowly with energy and is of order unity. Its purpose is to correct the classical approximations used here to agree with quantum mechanical effects. A is a constant involving the mass of the electron, the Thomson cross section of the ion and the fine-structure constant. The exponential dependence on energy results in a spectral shape which decreases rapidly at high energies, as shown in Fig. 1.3. The temperature shown is 0.2 keV, which is typical of the hot gas present in interstellar galaxy disks.

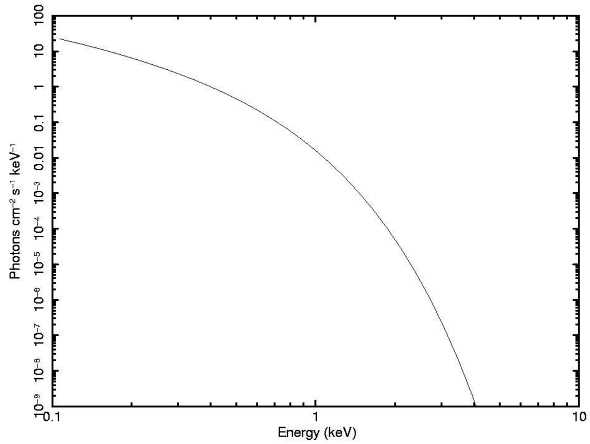

Figure 1.3: Simulated energy spectrum of thermal bremsstrahlung emission from gas at a temperature of 2.3×10^6 K (0.2keV).

1.2.3 Black-body radiation

A black body is an object which completely absorbs all electromagnetic radiation incident upon it. For energy to be conserved, this object must also radiate from its surface. Its spectrum is well described by Planck's law of black-body radiation:

$$I(E,T) = 2E^3[h^2c^2(e^{E/kT} - 1)]^{-1} \tag{1.5}$$

with h being Planck's constant. The higher the temperature of the black-body, the shorter the peak wavelength of the light emitted according to Wien's displacement law:

$$\lambda_{max} = b/T \tag{1.6}$$

where b is a constant, 2.898×10^{-3}m K^{-1}. For stars, this peak ranges from the infrared (red dwarf at 2500K) to the near ultraviolet (O stars at 40,000K). For newly formed neutron stars, which have temperatures exceeding 10^6K, the peak wavelength will be in the X-ray range. A model spectrum of black-body radiation at a temperature of 1 keV is shown in Fig. 1.4.

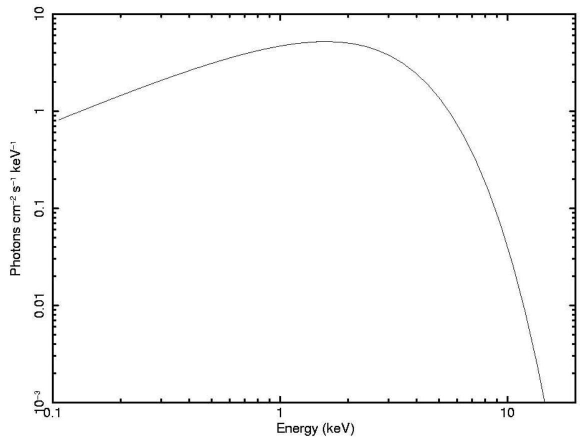

Figure 1.4: Simulated energy spectrum of black-body radiation from an object with a surface temperature of 1.1×10^7 K (1keV).

1.2.4 Inverse Compton Scattering

Compton scattering is the process by which a high energy photon interacts with a particle of much lower energy. In the collision, energy is imparted to the particle. Inverse Compton scattering is the reverse of this, in that a low energy photon interacts with a high energy relativistic particle, usually an electron in ionized material. As a result of the interaction, the photon is energized and if the electron is energetic enough, the resultant photon may be in the X-ray band. An illustration of the process is given in Fig. 1.5. The relationship between the initial and final energy of the photon (E_i and E_f) and the energy of the electron (E_e) is as follows (Tucker 1977):

$$E_f \approx (E_e/m_0c^2)^2 E_i \tag{1.7}$$

If the distribution of electron energies is a power-law with index β, the spectrum produced by Inverse Compton scattering should also be a power law with index κ, where κ = (β-1)/2. The gradient being the same as that produced by synchrotron radiation, the spectral shape produced is also the same. This radiation is commonly observed from the coronal regions above accretion disks, where high energy electrons in ionized material up-scatter low energy photons to X-ray energies. This forms a significant contribution to the X-ray spectrum observed from accretion-driven objects.

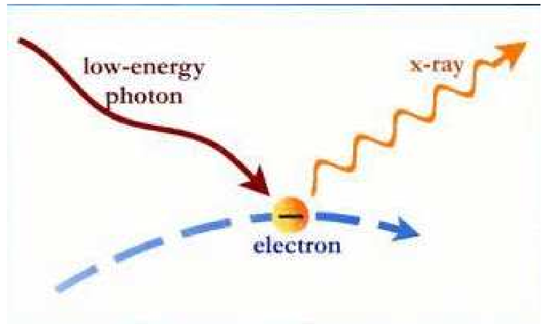

Figure 1.5: Illustration of inverse Compton emission. Image from http://www.astro.wisc.edu/.

1.2.5 Line Emission

Sharp line features are an extremely important component of X-ray spectra. In thermal plasmas, the majority of line emission is caused by collisional excitation and ionisation. A bound electron in an ion in its ground state may be brought into a higher energy level or removed completely through a collision with a free electron. In the situation where the bound electron is not removed completely, it will decay back to the ground state, either directly or through intermediate levels. As a result of these transitions photons are released at specific energies, which leads to emission lines in the spectrum of the source. Emission lines can also be produced by radiative recombination, the process by which a free electron is captured by an ion, releasing a photon. The rate of recombination in a plasma is highly dependent on the temperature, as low temperature plasmas are hard to ionise and high temperature plasmas form ions readily.

Line emission is observed in the accretion disks of low-mass X-ray binary systems. The material surrounding such systems is often iron-rich, due to the supernova which caused the production of the neutron star or black hole in the system. Free electrons collide with iron ions, exciting electrons in the K shell to a higher level. This creates gaps in the electronic structure, which are filled when other electrons fall through the energy levels to take their place. This results in strong emission features in the spectrum around this energy. For plasmas emitting through thermal bremsstrahlung at energies below 1 keV, there is a substantial contribution to the X-ray spectrum from oxygen (OVII and OVIII) and iron (FeXVII-XXI) emission lines (Kaastra et al. 2008) caused by collisional excitation.

As these features are based on atomic spectral transitions, they are extremely narrow. Their width is dependent on the velocity distribution of the atoms (which causes Doppler broadening) and gravitational

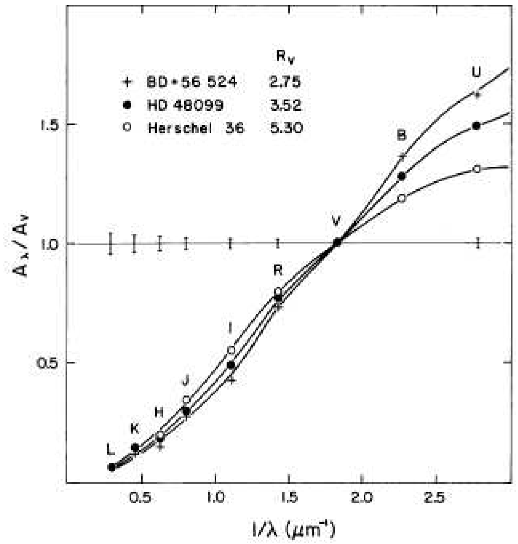

Figure 1.6: Comparison of dust extinction curves for emission ranging from 300nm to 3000nm (Cardelli et al. 1989) for several different values of $R_V = A(V)/E(B-V)$. Optical and near UV emission is shown to be preferentially absorbed by dust in comparison to infrared emission.

redshift (if they originate close to a massive object). Because of this, observation of a known spectral line at a different energy to that observed at rest can be used to find the redshift of a source, and hence its distance.

1.2.6 Absorption processes

A significant fraction of the X-ray emission may be absorbed in its surroundings or along its line of sight path to us. Photoelectric absorption of X-rays by the interstellar medium is the primary factor in limiting the distance X-rays can travel before they are absorbed. It is a continuum process and thus affects photons of all energies. Different ions have different absorption coefficients, and for soft X-rays below 1 keV most absorption is due to carbon, nitrogen, oxygen and neon ions. The effective absorption cross-section summed over all ions can be expressed as (Tucker 1977):

$$\sigma_{eff}(E) = \sum_Z \frac{N_Z}{N_H} \sigma_Z(E) \tag{1.8}$$

where N_Z is the density of ion Z, N_H is the proton density and σ_Z is the cross-section of ion Z.

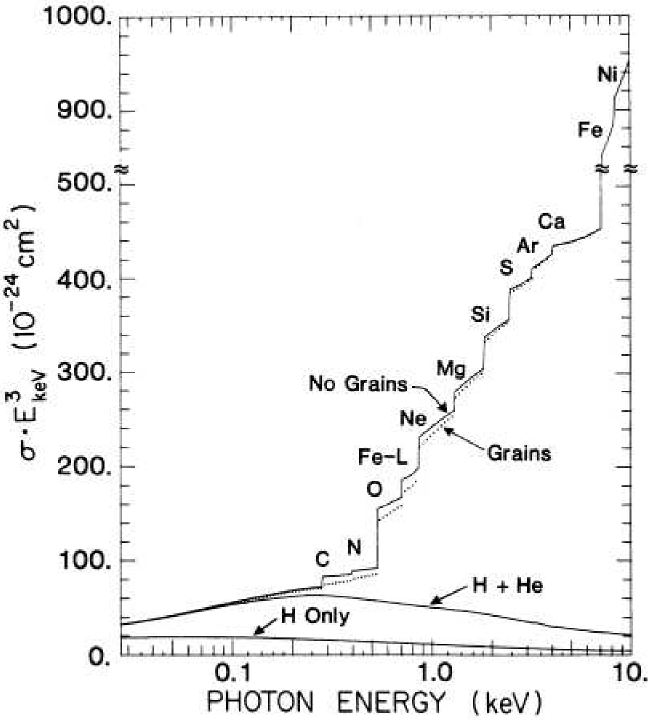

Figure 1.7: Net photoelectric absorption cross sections per hydrogen atom as a function of energy, scaled by $(E/1\text{ keV})^3$ for clarity of presentation. The contributions of hydrogen and hydrogen plus helium to the total cross section are also shown. Image courtesy of Morrison & McCammon (1983).

The relative abundances of different ions in the vicinity of a source has a considerable impact on the absorption of soft X-rays (Fig. 1.7). As the energy of X-ray photons increase, absorption edges arise as more elements in the ISM contribute to the total absorption. The curve shown is normalized by dividing by E^3 so as to give a flat absorption curve for hydrogen. It can therefore be seen that absorption due to hydrogen alone has in general an E^{-3} dependence on energy, with soft X-rays absorbed preferentially (Morrison & McCammon 1983).

From the above equation, we can express the total continuum opacity τ_{cont} as:

$$\tau_{cont}(E) = N_H \sigma_{eff}(E) \tag{1.9}$$

where N_H is the proton density and σ_{eff} is the effective continuum cross-section for absorption at that energy by all ions present. The corresponding transmission coefficient for the light to pass through such a clump of matter is:

$$T(E) = e^{-\tau_{cont}(E)} \tag{1.10}$$

A thermal bremsstrahlung spectrum with a continuum absorption component is shown in Fig. 1.8 (lower curve). In comparison with the unabsorbed bremsstrahlung spectrum (upper curve), there is significant absorption of soft X-ray photons leading to a downturn in the energy spectrum at low photon energies.

Dust absorption in the interstellar medium is strongly dependent on wavelength, with shorter wavelength emission affected much more strongly than at longer wavelengths. The shape of the absorption curve from infrared to ultraviolet emission is shown in Fig. 1.6 (Cardelli et al. 1989), and shows that ultraviolet emission is prefentially absorbed by dust for a range of R_V values.

X-ray photons at energies corresponding to an ionic transition are absorbed more strongly than in continuum absorption, leading to absorption line features in the observed spectrum. As in the case of continuum absorption, the transmission in a spectral line of a given wavelength λ is:

$$T(\lambda) = e^{-\tau(\lambda)} \tag{1.11}$$

with

$$\tau(\lambda) = \tau_0 \, \phi(\lambda) \tag{1.12}$$

where τ_0 is the opacity at the line centre, and $\phi(\lambda)$ is the line profile. The natural line profile is a Lorentzian, but significant Doppler broadening can produce a Gaussian profile. Commonly observed absorption lines in thermal plasmas below 1 keV are the 1s-2p transition in OVII and the OVIII Lyα doublet at around 0.5 keV.

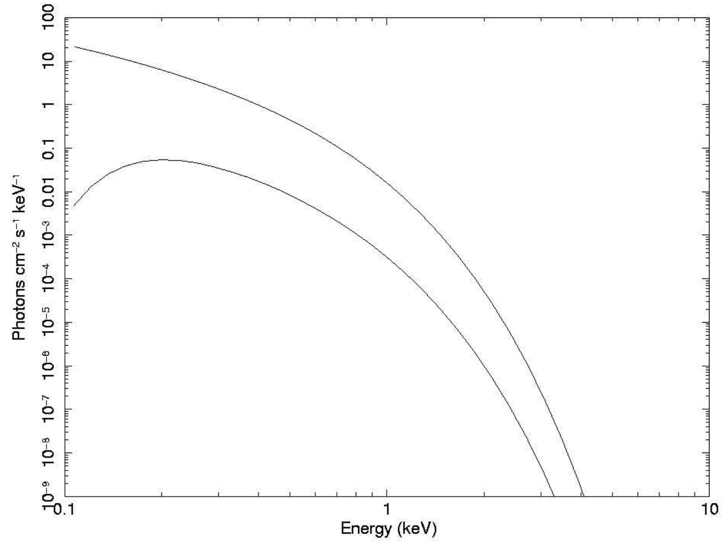

Figure 1.8: Simulated energy spectrum of thermal bremsstrahlung emission from gas at a temperature of 2.3×10^6 K (0.2 keV) with a foreground hydrogen absorption column of $1 \times 10^{20}\mathrm{cm}^{-2}$ (lower curve). Upper curve shows unabsorbed bremsstrahlung emission spectrum at the same temperature.

1.3 Accretion

Accretion is by far the most efficient method for conversion of mass to energy in nature, with an efficiency of $\approx 10\%$ compared to a maximum of 0.7% for nuclear fusion. As material falling onto a compact object loses gravitational energy faster than it loses angular momentum, it is forced into a series of decreasing circular orbits around it, forming an accretion disk. As mass accretes onto the compact object, the luminosity of the emitted radiation is related to the mass transfer rate as follows:

$$L_{acc} = \eta \frac{GM\dot{M}}{R} \tag{1.13}$$

where η is the efficiency of conversion of the infalling mass into energy, G is the gravitational constant, M is the mass of the object being accreted onto and $\dot{M}$ is the rate at which mass is being accreted onto the compact object at a radial distance R. The maximum stable luminosity achievable from this process is determined by the balance between the force of the radiation pressure and the gravitational force between a proton and an electron in the accreting gas, which is assumed to be ionized hydrogen. The point at which these forces become equal is the Eddington limit:

$$L_{Edd} = \frac{4\pi GMm_pc}{\sigma_T} \quad (1.14)$$

where σ_T is the Thomson cross-section of the electron, m_p is the mass of a proton and c is the speed of light. From this, it is clear that the maximum stable accretion luminosity is solely determined by the mass of the body accreted onto.

Depending on the magnetic field of the compact object, radiation is released from the accretion disk through several mechanisms. In the presence of a strong magnetic field, synchrotron radiation from electrons interacting with the field will be detected as a power law. Inverse Compton scattering also occurs in the coronal regions outside the disk, scattering photons to X-ray energies and also producing a power law spectrum. Thermalization of the accretion disk will produce a series of black-body spectra at different radii, which can be modelled as a "disk-blackbody" spectrum. This last component is most often observed in systems with a very high accretion rate, such as ultraluminous X-ray sources (ULXs).

1.4 X-ray Sources in Galaxies

The work detailed in this thesis focuses on the extended X-ray emission observed from the disks of nearby normal spiral galaxies. This X-ray emission consists of several components: X-ray emitting point sources associated with the galaxy, diffuse thermal emission from the galactic disk and halo, emission observed from foreground stars and background sources such as AGN, and the soft X-ray background. In order to isolate and study the properties of the thermal emission, it is necessary to understand the different components which contribute to the overall X-ray emission from the galaxy.

1.4.1 Low Mass X-ray Binaries (LMXBs)

Low mass X-ray binary systems consist of two stars in close orbit with each other: a neutron star or black hole (compact object) and a low-mass donor star (M$<$ $\mathrm{M}_{\odot}$). The donor star is of spectral type A or later, and donates mass onto the compact object. This process occurs when the separation of the objects is small enough that the Roche lobe of the compact object encompasses part of the photosphere of the donor star, such that matter from the donor can directly flow through the inner Lagrangian point

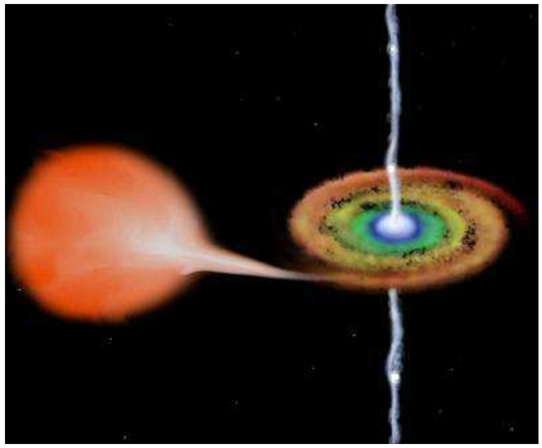

Figure 1.9: Illustration of direct mass transfer to a compact object by Roche Lobe overflow in a low-mass X-ray binary system. Image courtesy of NASA/CXC/SAO.

of the system and form an accretion disk. This is illustrated in Fig.1.9. If the compact object is a neutron star with a strong magnetic field, the accretion disk may be disrupted at the magnetospheric radius. Material then falls through magnetic field lines onto the poles of the neutron star, leading to very localised X-ray emission from that region. If the magnetic and rotational axes of the star are not aligned, this leads to observations of pulsed X-ray emission with a period equal to the spin period of the neutron star (a pulsar).

As for these systems the donor star is small and long-lived, the lifetime of the system will be on the scale of $10^8 - 10^9$yr. These systems are likely to be found preferentially in the bulge and intermediate stellar disks of spiral galaxies, as they are not associated with recent star formation activity. Studies of early-type galaxies with low star formation rates (SFR) which do not contain a large amount of hot X-ray emitting gas have found these sources to dominate the X-ray output in the 0.3-8 keV range (Sarazin et al. 2000; Sivakoff et al. 2003). The X-ray luminosity function (XLF) of these sources in early-type galaxies have shown a cumulative slope of -0.8–1.2 to fit the data well (Kim & Fabbiano 2004) up to the Eddington limit for a 3 $M_{\odot}$ neutron star, above which a fall-off occurs reflecting the mass function of black holes. A similar luminosity distribution is expected for these sources in late-type spiral galaxies. An example of this type of source is Scorpius X-1 (Kahn et al. 1984), the first X-ray source detected outside the Solar System.

1.4.2 High-mass X-ray binaries (HMXBs)

For systems with ongoing star formation activity, such as late-type spiral galaxies, there are far more massive young stars present than in elliptical galaxies. This results in a population which includes a second type of X-ray binary system. High-mass X-ray binaries consist of a massive early type (O or B) star and a neutron star or black hole in a binary system. Material is accreted either from the stellar wind of the donor star or through Roche Lobe overflow onto the compact object through the inner Lagrangian point, depending on the mass of the donor star. This is enough to power the X-ray output up to a significant fraction of the Eddington limit. As the donor star in HMXB systems is significantly more optically luminous than in LMXBs, the optical counterparts of these systems are expected to be of comparable luminosity to the X-ray luminosity of the compact object. An identifying characteristic of these sources is the presence of a bright blue optical counterpart. Both LMXBs and HMXBs typically exhibit power law X-ray spectral shapes modified by scattering, absorption and emission features. Photoelectric absorption of soft X-rays is higher in HMXBs than LMXBs, due to the dense circumstellar shell of material formed by the stellar wind of the donor star.

As the donor star in this case is extremely massive, HMXB systems are short-lived ($10^6 - 10^7$yr) and are preferentially found in regions of recent star formation, especially in the spiral arms of their host galaxy. In galaxies with high star formation rates, the HMXB population dominates the overall X-ray luminosity observed (Helfand & Moran 2001). A population study by Grimm et al. (2003) across several nearby star-forming galaxies has found the log N - log S cumulative luminosity function of these sources to be approximated by a power law with index -0.6, indicating that the most luminous ($L_X > 10^{38}$ erg s^{-1}) HMXBs dominate the observed luminosity. HMXB sources discovered in the Galaxy include Cygnus X-1 (Liu & Li 2004) and Vela X-1 (Kreykenbohm et al. 2008).

In both classes of X-ray binary systems, short-scale and long-scale variability of X-ray emission is observed. There are several different reasons for variability of an X-ray source, including eclipsing of an X-ray source by its donor and variation of the accretion rate. The second of these is thought to cause the difference between the two main spectral states observed in X-ray binary systems: the low/hard state and the high/soft state (Miyamoto & Kitamoto 2001). In addition to this, Quasi Periodic Oscillations (QPOs) are sometimes observed from neutron star and black hole binary systems, oscillations in the X-ray lightcurve close to a particular frequency. They may be caused by the buildup of material in the accretion disk around a compact object in a pattern which varies periodically (from 1-1000Hz). This periodicity is detected as a QPO. In the work presented here however, we consider the average spectral profile and luminosities of the point source population averaged across *XMM-Newton* exposures, and do not study source variability in depth.

1.4.3 Ultraluminous X-ray Sources (ULXs)

ULXs are defined as X-ray sources with a luminosity in the X-ray bandpass exceeding 10^{39} erg s^{-1}, which are not nuclear supermassive black holes. Their nature is a subject of significant debate. Some argue they are X-ray binary systems containing black holes with masses above $1000\ \mathrm{M}_{\odot}$ (Intermediate Mass Black Holes (IMBH); Madau & Rees 2001; Volonteri et al. 2003). Miller (2005) argues that accretion disks found at lower temperatures indicate that the disk extends to a greater distance from the compact object. These larger, cooler disks might be found around a more massive black hole. If this argument is valid, the observations of bright sources with accretion disks at temperatures of 0.2-0.3 keV suggest the presence of a compact object with mass above $1000\ \mathrm{M}_{\odot}$. Others claim that this emission originates in a stellar-mass black hole either in a very high state (King et al. 2001; Roberts 2007) or emitting through relativistic jets (Körding et al. 2002). Models developed by Done et al. (2007) suggest that at high luminosity, the accretion disk around a compact object is strongly distorted by Comptonization, leading to the observed spectral shape. These models also allow for variable accretion rates which periodically exceed the Eddington limit, explaining the very high luminosity observed should the compact object be a stellar-mass black hole. The observed population of ULX sources is correlated with star forming regions (Swartz et al. 2004; Liu & Mirabel 2005), which suggests that a possible model for these objects is a young HMXB-type system in a very high accretion state. The spectra of these objects are generally well-modelled by a combination of power law and disk black-body components, as stated in §1.3. No sources with sufficient luminosity to be classified as a ULX have been discovered in the Galaxy, but an increasing population is being discovered in nearby galaxies. This population includes Holmberg II X-1 (Goad et al. 2006), which has been observed in different accretion states and NGC1313 X-1 (Turolla et al. 2006), which was singled out as a good candidate for an IMBH.

1.4.4 Supernova Remnants (SNRs)

Supernova remnants are observed with X-ray luminosities (0.3-6 keV) of up to 10^{38} erg s^{-1}, and are the product of excitation of gas surrounding a supernova explosion to X-ray emitting temperatures. They can be divided into three categories, depending on the type of supernova event. Type Ia supernovae arise as a result of accretion onto a white dwarf until electron degeneracy pressure is overcome, and their remnants are found to be associated with the old stellar population of a galaxy. Type Ib and type II supernovae, both originating with the explosion of a massive evolved star, are found preferentially in areas of star formation. Recent SNRs in galaxies outside the Local Group are detected as point sources in X-rays, as their angular extent is too small to be resolved successfully with current detectors.

Studies of nearby SNR in the LMC have found the X-ray spectrum of the hot gas inside the remnants to be well-modelled by thermal plasmas with temperatures of 0.2 keV and 0.7 keV (Borkowski et al. 2001; Williams et al. 2004), depending on the age of the remnant. Very young remnants observed are characterised by a hotter spectrum, with temperatures of 0.8-1 keV and 3-5 keV, caused by the expanding shockwave interacting with material closer to the centre of the supernova event (Immler 2003). Synchrotron emission from some young remnants has also been observed, due to the extremely strong magnetic fields associated with the supernova event (Ballet 2006). This produces a complex X-ray spectrum, with a combination of power-law and thermal components present. Well-known SNR sources include SN 1987A in the LMC (Haberl et al. 2006) and Cassiopeia A in the Galaxy (Patnaude & Fesen 2007), both of which originated in type II events.

1.4.5 Lower luminosity X-ray point sources

The majority of bright ($L_X > 10^{37}$ erg s^{-1}) X-ray sources observed in spiral galaxies are X-ray binary systems and bright supernova remnants. In external galaxies outside the Local Group, this is the limit for identification of individual sources using present day techniques. The residual X-ray emission detected includes diffuse X-ray emitting gas and the integrated emission from a complex population of lower luminosity point sources. These include faint X-ray binaries and SNRs as well as the following emission sources:

Cataclysmic variables (CVs) are similar to X-ray binary systems, as they involve accretion from a donor star onto the surface of a compact object. In this case however, the compact object is a white dwarf. The X-ray properties of these systems are highly dependent on the magnetic field of the white dwarf. In systems with a strong field no accretion disk is formed, with material accreting along the field lines directly onto the magnetic poles of the star. After a critical amount of material has built up, a shock is formed, expelling the material and heating the surrounding plasma to X-ray temperatures. Cyclotron emission is observed in this case. In systems where the magnetic field is weak, steady low-accretion rate sources are expected. The X-ray luminosity of these sources is about $10^{31} - 10^{32}$ erg s^{-1}, with the brightest magnetic CVs in outburst observed at 10^{35} erg s^{-1}. The integrated X-ray luminosity of CVs in our own Galaxy has been estimated to be 4×10^{38} erg s^{-1} (Mukai 2003), and the thermal plasma in the area surrounding these sources has been detected at a temperature of 0.65 keV (Fujimoto & Ishida 1997), with shock temperatures of 15-30 keV. CVs are expected to significantly contribute to the unresolved hard X-ray emission observed from galaxies (Revnivtsev et al. 2008).

Below X-ray luminosities of 10^{31} erg s^{-1} the X-ray emission from Active Binaries (RS CVn stars) as well as coronal emission from O and B stars must be considered. These sources are extremely faint individually, but their large number in galactic disks makes their contribution significant (Revnivtsev et al. 2007).

1.4.6 Diffuse Gas in Spiral Galaxy Disks

The hot X-ray emitting gas in galactic disks is believed to originate from shock heating of gas in the interstellar medium (ISM) to temperatures of $\approx 10^6$K by supernovae and stellar winds (*e.g.* Cox & Smith 1974; Bregman 1980; Chevalier & Clegg 1985). Its abundance and distribution is dependent on the rate of supernovae and the evolution of SNRs in a galaxy. In galaxies such as our own, the hot gas produced by supernova explosions may be transferred from the disk into the halo via galactic fountains and chimneys (Shapiro & Field 1976; Norman & Ikeuchi 1989). This gas subsequently cools and falls back to the disk. In spiral galaxies, the emission from this hot gas has been detected with X-ray luminosities of $10^{37} - 10^{41}$ erg s^{-1} (Fabbiano & Trinchieri 1987; Read et al. 1997), and makes up a significant fraction of the total X-ray emission observed in the soft band (0.3-1 keV). In a number of face-on spiral galaxies, a qualitative correlation has been found between the unresolved emission present and recent star formation activity, as traced through mid-infrared and Hα emission (Pietsch et al. 2001; Tyler et al. 2004; Trudolyubov et al. 2005). In edge-on starburst galaxies, extraplanar diffuse emission has been detected correlated with estimates of the star formation rate (Strickland et al. 2004a; Strickland et al. 2004b). This indicates a possible proportional relationship between diffuse X-ray emission and star formation rate in galaxies exhibiting significant recent star formation. Exploring this relationship is the primary goal of the analysis performed in this thesis.

As stated in §1.2.2, gas heated to temperatures above 10^5K will be ionized, producing a gas consisting of free electrons and ions. Interactions between the electrons and ions cause the electrons to radiate by bremsstrahlung. If the gas is at temperatures above 10^6K, this emission is detected in the soft X-ray band. The X-ray spectrum of this emission has been found to be well fit for several nearby galaxies with a two-temperature *MEKAL* model, with characteristic temperatures of kT≈ 0.2 keV and $\approx 0.6-0.7$ keV (Fraternali et al. 2002; Kuntz et al. 2003; Warwick et al. 2007). This model comprises continuum emission from bremsstrahlung along with scattering, absorption and emission line features resulting from atomic processes in the plasma (Mewe et al. 1986).

1.5 Overview of the Thesis

In this thesis, we examine the extended X-ray emission observed from a sample of seven nearby face-on, late-type spiral galaxies using *XMM-Newton* archival data. We explore the morphological and spectral properties of the unresolved X-ray emission observed in the galactic disks after exclusion of the bright point source population in each galaxy, in order to explore the linkage between this emission and recent star formation. The primary goals of the study are: to identify any trends in spectral properties and spatial distribution of the unresolved X-ray emission in galactic disks, to examine the spatial correlation of this emission with FUV emission (which we use as a tracer of star formation), and to derive a quantitative relationship between the unresolved X-ray luminosity and star formation rate in late-type spiral galaxies. Having separated the bright point sources in each galaxy from the residual emission, we also attempt to classify the nature of this population of sources through analysis of their hardness ratios, according to a classification scheme devised by Prestwich et al. (2003). By this method we try to find whether the bright point sources arise primarily from the young or old stellar population in the galaxies.

To achieve these aims, the thesis is structured as follows. Chapter 2 provides details of instruments used in the analysis and data analysis techniques. We concentrate primarily on the *XMM-Newton* observatory, but also briefly mention *GALEX*, which is used for comparative UV analysis. We describe the novel methods used for reduction and analysis of *XMM-Newton* data. Chapter 3 details the analysis of extended X-ray emission from a sample of six nearby face-on spiral galaxies: M51, M74, M83, M101, NGC300 and NGC3184. We study the spectral properties of this emission across the sample, and explore its spatial relationship with UV emission in the galaxy disks. A relationship is derived between soft X-ray emission and star formation rate in the sample. Chapter 4 describes the bright point source populations in the same set of galaxies. We classify the sources according to their hardness ratios and infer the relative contributions from the old and young stellar populations. Chapter 5 extends our analysis to one further nearby galaxy: M33. We examine the relationship between the extended X-ray emission present and SFR in the inner disk of the galaxy and compare it to the results derived in our previous study. Through study of the point source X-ray luminosity function, we predict how much of the unresolved emission observed is due to diffuse gas as opposed to faint point sources. Chapter 6 summarises the results of the thesis, describes our conclusions and discusses potential future work in this area.

Chapter 2

Instrumentation and Data Analysis

2.1 The *XMM-Newton* Observatory

2.1.1 Properties of the *XMM-Newton* observatory

The *XMM-Newton* observatory was launched on December 10, 1999 aboard an Ariane-5 rocket into a highly elliptical 48-hour orbit, ranging from 7,000 km to 114,000 km from Earth. An artist's impression of the observatory in orbit is shown in Fig. 2.1. On board are three Mirror Modules with focal length 7.5m, each composed of 58 nested Wolter-I-type shells. At the primary focal point of these Mirror Modules lie the EPIC (European Photon Imaging Camera) detectors. Two of the three cameras consist of an array of seven MOS (metal-oxide semiconductor) CCDs (Turner et al. 2001), with the third consisting of an array of 12 back-lit pn (positive-negative) CCDs (Strüder et al. 2001). The arrangement of the CCDs on each of the detectors is shown in Fig. 2.2. Incoming X-ray photons incident on these detectors are tagged with their positions and energies such that imaging and spectral analysis can be performed. In the case of two of the Mirror Modules, the X-ray radiation is partly intercepted by a grating, which deflects some of the photons onto a reflection grating spectrometer (RGS), for the purpose of high-resolution spectroscopy. The configuration of the telescope is shown in Fig. 2.3. An Optical Monitor (OM) telescope is co-aligned with the X-ray instruments for simultaneous observation of targets in several UV and optical wavebands.

Figure 2.1: Artist's impression of *XMM-Newton* . Image taken from http://xmm.esac.esa.int/

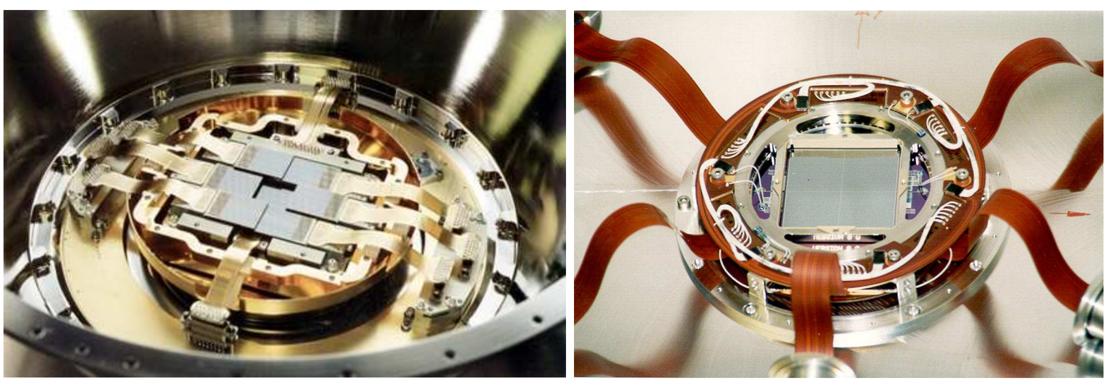

Figure 2.2: *Left panel:* The arrangement of the CCDs on one of the MOS cameras. The relative orientation of the two MOS cameras is such that the chip gaps between the outer CCDs in one camera are covered in the other. *Right panel:* The arrangement of the CCDs on the pn camera. Images taken from http://xmm.esac.esa.int/

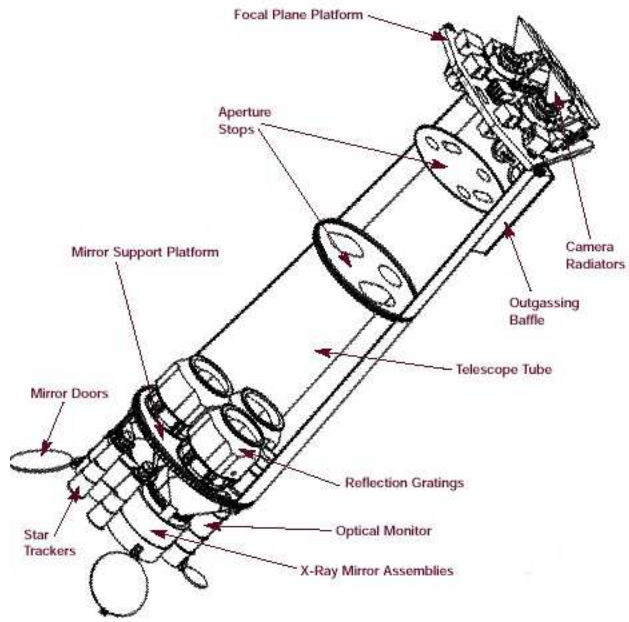

Figure 2.3: The configuration of *XMM-Newton* . Image taken from http://xmm.esac.esa.int/

Details of the properties of the EPIC cameras are given in Table 2.1. There are several different modes of operation of the MOS and pn cameras, each suitable for analysis of different targets. The "full-frame" mode is useful for imaging and spectral analysis of multiple and extended sources within the field of view. Alternatively, for the same analysis of an isolated bright point source or a bright source with small spatial extent, "large window" or "small window" modes can be used. For these restricted modes, only a small area of the central MOS CCD is used to read out data in each case. In the pn camera, half of the total CCD area is read out in "large window" mode, with only a small part of one CCD read out in "small window" mode. Use of these modes allows brighter sources to be analysed than full-frame mode without deterioration of the signal due to photon "pile-up". For high resolution timing analysis of a particular source, either MOS or pn camera can also be used in "timing" mode, with a "burst" mode also available for the pn camera for even higher time resolution. In this mode, some information about the source position is lost. The different operating modes are illustrated for MOS and pn in Fig. 2.4. For the X-ray analysis performed in this thesis, we have primarily utilised data from the EPIC MOS and pn detectors in full-frame mode, appropriate to our study of the spatial and spectral distribution of point sources and extended X-ray emission across a large area of the *XMM-Newton* FOV.

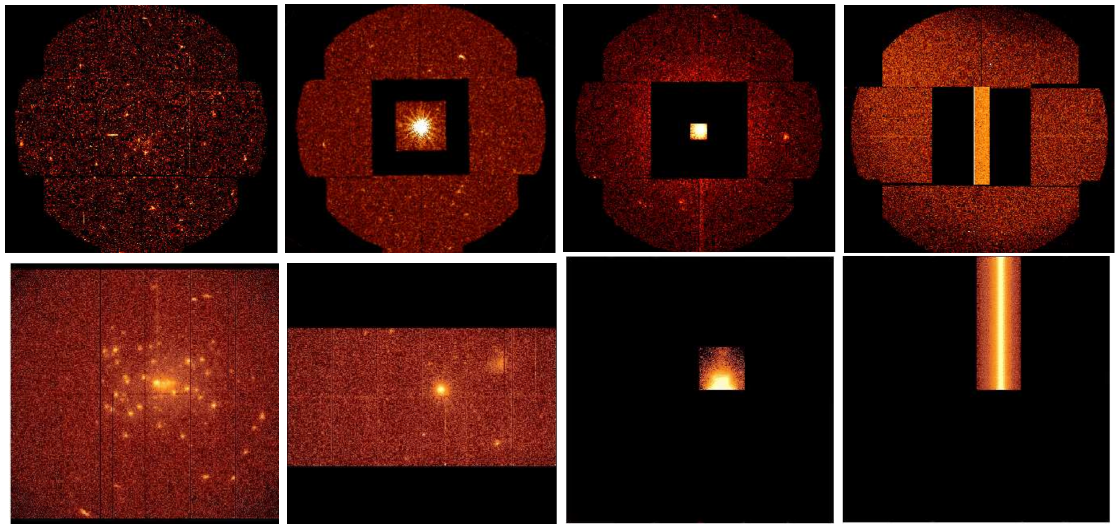

Figure 2.4: *Top panels:* Images recorded by a MOS camera operating in different modes. From left to right: Full frame mode, Large window mode, Small window mode, Timing mode. *Bottom panels:* Images recorded by the pn camera operating in different modes. From left to right: Full frame/extended full frame mode, Large window mode, Small window mode, Timing mode. Images courtesy of the *XMM-Newton* Users' Handbook.

Table 2.1: Properties of the EPIC MOS and pn cameras.

	MOS	pn
Bandpass	$0.15 - 12$ keV	$0.15 - 15$ keV
Sensitivity	10^{-14} erg cm^{-2} s^{-1}	10^{-14} erg cm^{-2} s^{-1}
Linear FOV	$30'$	$30'$
PSF (FWHM/HEW)	$5''$ /$14''$	$6''$ /$15''$
Timing sensitivity	1.5 ms	0.03 ms
Spectral resolution	70 eV	80 eV

2.1.2 X-ray imaging using *XMM-Newton*

A limiting factor in the spatial resolution of the EPIC cameras is the extent of the point spread function (PSF) of the mirror modules. For the *XMM-Newton* cameras, the PSF varies little over a wide energy range (0.1-6.0 keV). Images of the model PSF for an on-axis point source are given in Fig. 2.5, with the encircled energy function (EEF) as a function of radius shown in Fig. 2.6. The on-axis PSF is mathematially described by a King function, which we describe later in this chapter. The star-like pattern evident in the MOS PSF image, and to a lesser extent in the pn image, is due to the structure supporting the mirrors of the telescope. This is faint enough to have little impact on the majority of observations. The EEF of the cameras shows that approximately $65-70\%$ of photons from a point source will lie within $15''$ of its true position on the sky, with 90% of photons within $1'$. The EEF plots at different energies show that the PSF does not vary greatly with energy across the entire range of the detector. However, at large off-axis angles, the PSF becomes elliptical due to astigmatism of the mirrors.

Another factor which affects the detection of X-ray photons is the mirror effective area, which has a very strong dependence on energy (see Fig. 2.7). The large differences in effective area are dependent on the quantum effiency of the detector changing with energy, as well as the ability of the mirror to focus photons of different energies. The effective area also changes with position on each detector, with largest effective area at the centre, an effect known as vignetting. In order to perform spectral analysis of a source, these factors must be corrected using an appropriate Area Response Function specific to the position on the detector.

For each observation, an optical blocking filter is also used to stop optically generated photo-electrons from causing spurious detections. There are three filters in use of varying thicknesses, with the thickest of these minimizing the contamination from optical light. However, the use of this filter leads to a decreased sensitivity to soft X-rays. Therefore, the majority of observations of targets expected to have a soft X-ray spectrum are carried out using the medium or thin filters. The effective areas of the pn camera for each filter are shown in Fig. 2.7.

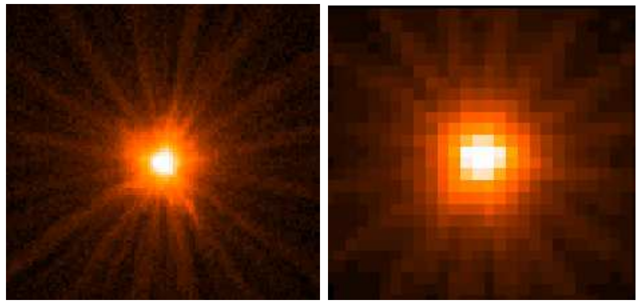

Figure 2.5: The on-axis PSF of one of the MOS cameras (left panel) and the pn camera (right panel), extending to a radius of $55''$. The resolution of the MOS image is $1.1''$, whereas that of the pn is $4.1''$.

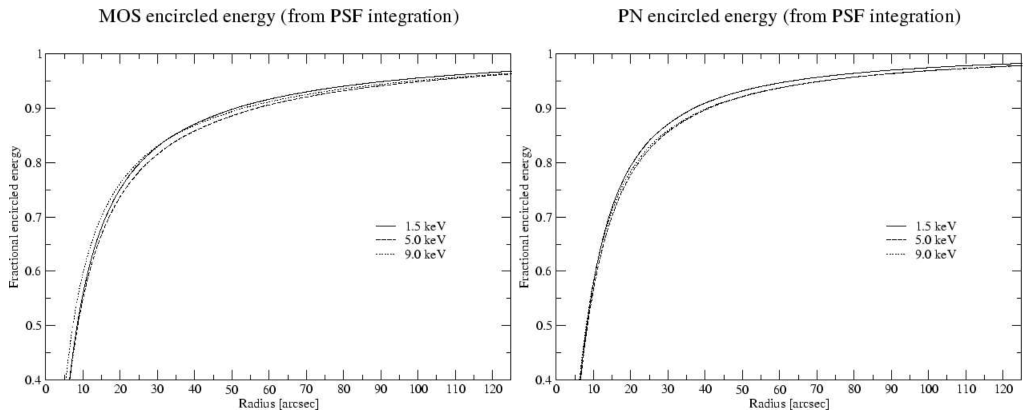

Figure 2.6: *Left panel:* The encircled energy within a given radius for the PSF of a MOS camera at three different energies. *Right panel:* The encircled energy within a given radius for the PSF of the pn camera. Images courtesy of the *XMM-Newton* Users' handbook.

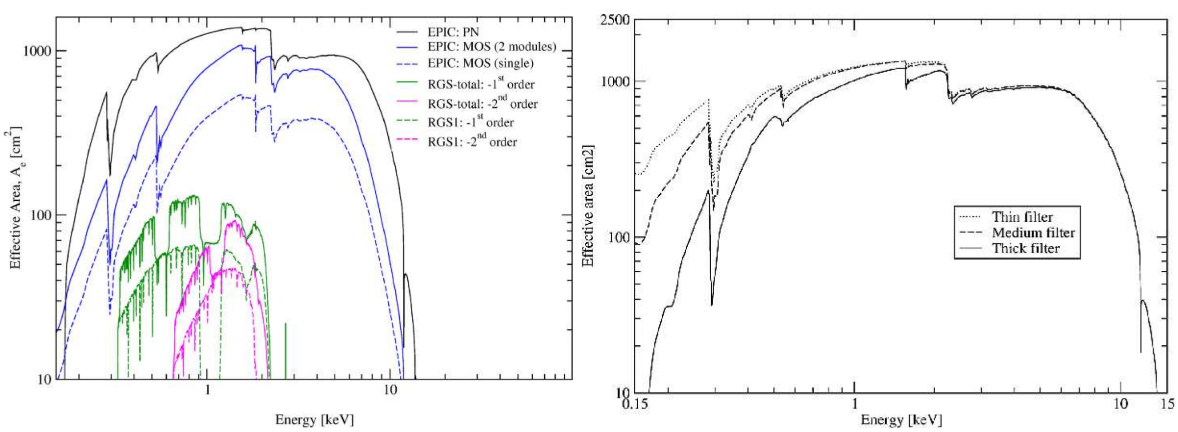

Figure 2.7: *Left panel:* The effective area of each of the *XMM-Newton* detectors as a function of photon energy. *Right panel:* The effective area of the pn camera using each of the three filters. Images courtesy of the *XMM-Newton* Users' handbook.

2.1.3 Other detectors used for analysis

In addition to the X-ray analysis performed using the *XMM-Newton* EPIC cameras, we have utilised ultraviolet observations from two other instruments, with the goal of comparing extended emission from galactic disks between different wavebands: the *XMM-Newton* OM and the Galaxy Evolution Explorer (GALEX) observatory.

The OM is a modified Richey-Chrétien telescope co-aligned with the three *XMM-Newton* Mirror Modules, with a primary mirror diameter of 30 cm (Mason 2001). It can be used for optical and UV imaging with a resolution limit of $1''$, covering a wavelength range of 180-600nm (depending on the filter in use). It has a field of view of $17' \times 17'$ and can detect sources ranging between optical B magnitudes of 20.7-7.4, the upper limit corresponding to the maximum brightness observable without causing permanent damage to the telescope. Our OM observations in this thesis are limited to the UVW1 bandpass ($\lambda_{central} \approx 2675$ Å).

GALEX is an observatory which consists of a Richey-Chrétien telescope with mirror diameter of 50 cm, and was launched in 2003 (Morrissey et al. 2007). It is currently in a circular low-Earth orbit at an altitude of 690 km. A beam splitter focuses the incident light on two detectors, sensitive to NUV ($\lambda \approx 2271$ Å) and FUV ($\lambda \approx 1528$ Å) photons. The field of view for a single observation is $\approx 1.25^{\circ} \times 1.25^{\circ}$. Similar to the OM, there is an upper AB magnitude limit for targets of 9.5 for the FUV detector and 8.9 for the NUV detector, with limiting lower magnitudes for source detection ranging between 24-20. The image resolution is $4-5''$ (FWHM), comparable to that of the *XMM-Newton* EPIC cameras. In this thesis, we have primarily used FUV-band catalogue images to investigate the relationship between X-ray and UV emission in our sample of spiral galaxies, along with processed GALEX FUV data from Muñoz-Mateos et al. (2007).

2.2 Data Analysis

For analysis of our sample of spiral galaxies, we have used *XMM-Newton* archival data which has already been subject to standard pipeline processing using the XMM Science Analysis System (SAS) (for details see http://xmm2.esac.esa.int/sas/). The pipeline products include event lists and exposure maps in several energy bands for both MOS and pn cameras, which were used as the starting point for our analysis. The majority of the analysis was performed using Q, a general purpose data analysis system based on Fortran 77 (for details, see http://www.star.le.ac.uk/~rw/q_v6/index.html). Using this, we were successfully able to apply event filtering criteria to event lists in the same way as the SAS tool *evselect*. In addition, it was possible to separate the components of the galactic X-ray emission from each other using complex image analysis, as well as to extract different spectral components for external analysis using the spectral fitting program XSPEC. In the following section, unless otherwise indicated, Q was used to conduct all procedures mentioned.

2.2.1 Filtering *XMM-Newton* Event Lists

We filtered the pipeline product *XMM-Newton* event lists for MOS and pn cameras in two ways. First, to identify the time in the exposure when soft proton flaring dominates the observation, we extracted lightcurves for each camera individually in the 10-15 keV band, separated into 100 second bins. Each of these lightcurves was inspected and a cutoff imposed at a level significantly above the quiescent level. In this way, a Good Time Interval (GTI) file was produced for each camera, flagging the times during the exposure where the flaring was too great. In our sample of observations, anywhere from 0-25% of the on time of the pn and MOS cameras was affected by this flaring, and the data from those time periods was excised. The entire event list was then filtered using several criteria. The pattern of the event was chosen to allow only single or double pixel events through for the pn camera ($PATTERN = 0-4$), whereas for each MOS camera single through quadruple pixel events were allowed ($PATTERN = 0-12$). These represent the set of calibrated X-ray generated patterns. We used the conservative $FLAG = 0$ criterion to remove hot columns, hot pixels and events from the corners of the detector not exposed to the sky, with a separate FLAG criterion used to isolate the X-ray events in these corner areas. The event lists were further filtered by the event time (through the GTI file) and by energy. The energy bands chosen were 0.3-1 keV, 1-2 keV and 2-6 keV so as to be consistent with previous studies. Images were created for both central field and corner regions in each of these energy bands for MOS1, MOS2 and pn cameras, with the MOS camera data coadded to improve signal-to-noise. A constant value was subtracted from these images, corresponding to the particle rate from the corners of the detector (assumed to be flat across the entire detector), and the image divided by the relevant pipeline exposure map. The resulting count-rate images could then be used for further analysis. All *XMM-Newton* images extracted in our analysis have been binned to a pixel size of $4'' \times 4''$, so as to be commensurate with the HEW of the point source PSF.

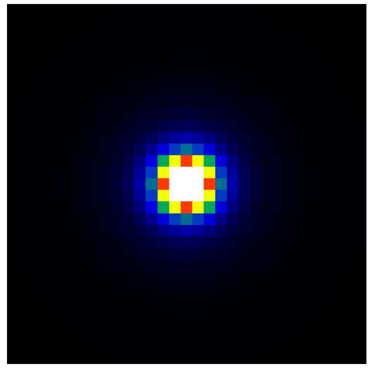

Figure 2.8: Simulation of the soft-band PSF extracted from the pn camera extending to a radius of $1'$. Each pixel covers an area of $4''\ \times 4''$.

2.2.2 Simulation of the *XMM-Newton* Point Spread Function

The extent of each of the X-ray point sources in the X-ray images produced is dependent on the Point Spread Function of the camera, as mentioned in §2.1.2. The *XMM-Newton* calibration files show the profile of the MOS and pn PSFs close to the centre of the FOV to be well-approximated by a King function of the form:

$$PSF(r) = \frac{A}{(1 + (r/r_0)^2)^\alpha} \tag{2.1}$$

The values of r_0 and α vary depending on the camera, energy and position on the detector. We chose to use the on-axis PSF for each camera, at the energies closest to the midpoint of each of our three energy bands. For each band and camera, we then simulated the extent of the PSF to a radius of $1'$ from the centre of the source (extended to $2'$ for analysis of M33). Each PSF was scaled such that the correct fraction of counts lie within $1'$ of the source, as indicated by the EEF. An image of the pn soft-band simulated PSF is shown in Fig. 2.8. All of the simulated PSFs used in this thesis are circularly symmetric. For sources detected significantly off-axis, the circular approximation to the PSF is not as good. For the majority of our galaxy sample, the galaxy is the target of the observation, so most of the detected sources are within $8'$ of the on-axis position. At this distance off-axis at a photon energy of 1.5 keV, 90% of photons fall within $60''$ of the source position, compared with a spread of $52''$ for an on-axis source. This is a small enough difference that our approximation of the PSF profile is valid.

2.2.3 Identification of Bright Point Sources

We used the images created in §2.2.1, along with the source list from the Second *XMM-Newton* Serendipitous Source Catalogue (2XMM) for the relevant observation to identify the bright point source population in each galaxy studied. Although the superior spatial resolution of *Chandra* observations would allow better identification of the point source population present in our images, we primarily used the 2XMM catalogue for two main reasons. Firstly, long-term variability of sources between *Chandra* and *XMM-Newton* observations affected the source population identified with each observatory for each system. In addition, the observation times for each of the galaxies in our sample with *Chandra* varied significantly, whereas the *XMM-Newton* observations across the sample were comparable in length. Therefore, in order to achieve a consistent flux threshold for bright point sources across the sample, we decided to use 2XMM data drawn from these observations. Information from deep *Chandra* observations of nearby galaxies was used to define the X-ray luminosity function of point sources in these systems, which served to extrapolate the luminosity of the point source population below the 2XMM threshold.

In order to find the luminosity of the bright point sources in each observation, it was necessary to evaluate the surface brightness of the X-ray emission due to the galactic disk. This was achieved by imposing a surface brightness cut on the raw count-rate MOS and pn images in each band to remove the influence of bright point sources, then heavily smoothing the remainder with a $20''$ gaussian mask. This had the effect of setting a local background level for each source. Next, for each source position in the 2XMM catalogue, we analyzed the raw count-rate image and the smoothed background image out to a radius of $16''$ in each band and camera, extracting the background-subtracted count-rate in each band. This was scaled to account for the extent of the PSF beyond the $16''$ analysis region. We then created a simulated image of the point source in each band, using the appropriate simulated PSF detailed in §2.2.2, scaled to the detected count-rate. This was repeated for each point source in the catalogue for the observation in both MOS and pn cameras, with each simulated PSF centred on the 2XMM position of the source, to build up a simulated image of all point sources in the field for the combined pn+MOS image.

As a final iteration, count rates were extracted from the simulated images within a $16''$ cell centred on each source position and compared to those obtained from the actual data, with any differences attributable to the PSF spreading of signal from adjacent sources. Based on this analysis, the nominal

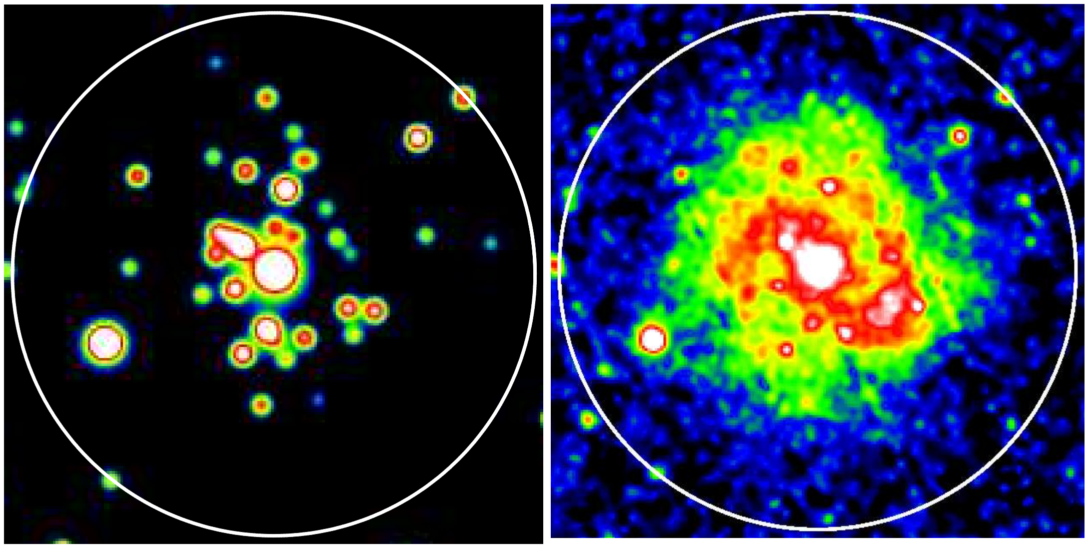

Figure 2.9: *Left panel:* The modelled “bright source” image constructed for M83 from a set of count-rate scaled PSF sub-images. *Right panel:* The broad-band adaptively smoothed pn+MOS image of M83 for comparison. In each case the circle has a diameter of $12.9'$.

source count rates were adjusted to compensate for this source confusion effect and a new version of the simulated images was produced. The simulated source image for M83 is shown in Fig. 2.9, alongside a smoothed broad-band image of the galaxy.

With the final count-rates extracted in each band and camera for each source in the catalogue, the count-rates were converted to unabsorbed fluxes and hence luminosities using *WebPIMMS*, assuming a source spectral model of a power law with $\Gamma = 1.7$. This was selected to correspond to the average spectrum of an X-ray binary system (Fabbiano 2006), and is consistent with the spectra found in the source regions of the galaxies studied. A luminosity cut was imposed to exclude sources below a given luminosity from our sourcelist in each galaxy, and this defined our “bright source population”. The level of the luminosity cut was chosen such that our source sample in each galaxy was assumed complete to that level. This new sourcelist was used to perform another iteration of the entire process and derive our final count-rates and luminosities for each source.

2.2.4 Separation of Point sources from unresolved emission

First, for each galaxy in the sample we defined an ellipse corresponding to its D_{25} extent (the approximate optical extent of the galaxy, as measured in the B band). This was chosen with reference to the

RC3 galaxy catalogue (de Vaucouleurs et al. 1991). As the galaxies studied in Chapter 3 all have almost face-on inclination, the region was approximated as a circle for simplicity. However, for M33 (Chapter 5) the inclination is too large for this approximation to be valid, so an elliptical region was used.

Using the broad-band pn+MOS simulated images created in §2.2.3, it was possible to separate the areas within the D_{25} region of each galaxy dominated by X-ray emission from bright point sources from areas where unresolved X-ray emission is more prominent. A source mask was created by imposing a surface brightness cut on the simulated image such that $\approx 90\%$ of the incident photons attributable to the bright source population lay within the mask. Any higher percentage would result in a source mask which filled too large a fraction of the galactic disk, making observation of the residual emission far more difficult. The remaining source counts escaping the mask were dealt with in two ways. For imaging analysis, the source mask was imposed after direct subtraction of the simulated image from the relevant raw count-rate image. In this way, the bright source PSFs extending beyond the source mask were removed. Fig. 2.10 shows the simulated soft-band image and combined MOS+pn soft-band image, both with the source mask imposed. The source mask also marks the areas of each galaxy used for extraction of the "bright source" and "residual galaxy" spectra. To account for the overspill of bright source counts into the residual galaxy in spectral analysis, the relevant percentage of the bright source spectrum was included in the residual galaxy fit.

2.2.5 Spectral fitting

As detailed in §2.2.4, the source mask and D_{25} regions divide the galaxy into two areas: a "bright source" region and a "residual galaxy" region. The observed emission from the former is dominated by X-ray emission from the brightest source population, whereas that from the latter comprises a combination of truly diffuse X-ray emitting gas, the faint point source population in the galaxy and the aforementioned spillover of the bright source population. There is some contamination of the bright source spectrum from the underlying residual galaxy emission, but we show that its contribution is comparatively small (as shown in 3.4.1).

The procedures to extract the spectra described here were utilised for the analysis in Chapter 3. A slightly modified method was used for M33, which we describe in more detail in Chapter 5.

The event lists for each galaxy were filtered by flag, pattern and GTI in the same way as §2.2.1, with a

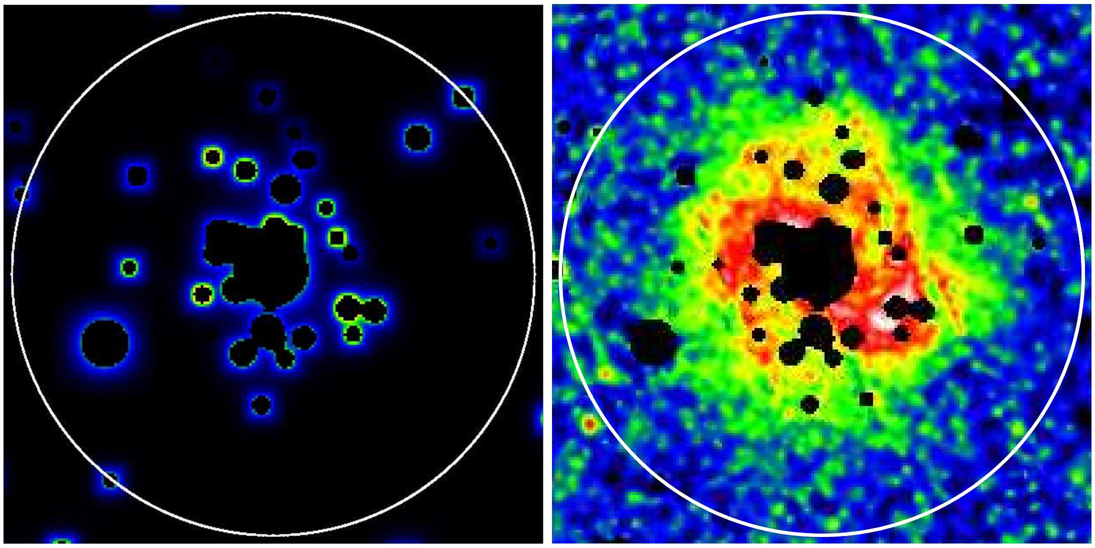

Figure 2.10: *Left Panel:* Soft-band (0.3-1.0 keV) pn+MOS simulated image of M83 with the source mask imposed, showing the spillover of source counts into the residual galaxy. *Right panel:* Soft-band pn+MOS image of the residual emission in M83, produced by subtraction of the model source image and imposition of the source mask. The outer circle in each case has a radius of $6.4'$ and corresponds to the D_{25} extent of the galaxy.

wider range of energies chosen (0.2-12 keV). The source mask and D_{25} regions were used to spatially filter the event list into the "bright source" region and "residual galaxy" regions, and the spectrum of each of these regions was extracted. SAS tools *arfgen* and *rmfgen* were used on the D_{25} region of the galaxy to produce appropriate ARFs and response matrix functions (RMFs) for each galaxy. The resultant spectra were binned in energy with a minimum of 20 counts per bin, in order to ensure that Gaussian statistics were valid when performing the spectral fits.

The main difficulty in fitting the spectrum of an extended emission region is the calculation of an appropriate background. As the soft X-ray background varies considerably across the sky, the use of "blank-sky" observations is not ideal. We therefore used a scaled combination of the particle background spectra from the corners of the detectors (PBG) and from an annular region outside the D_{25} region of the galaxy as a measure of the local background (LBG). The true background beneath the galaxy is made up of a combination of X-ray sky photons (which are vignetted) and particle events (which are not vignetted). The LBG spectrum will also contain these two components but, as the annulus is generally more off-axis than the galaxy region, the ratio of these components is different between the two regions. To correct for the different vignetting effects between the two regions (as well as the different areas used), we scaled the LBG and PBG spectra as follows:

$$LBG = (A_C/A_L) \times (V_C/V_L) \tag{2.2}$$

$$PBG = (A_C/A_P) \times (1 - \frac{V_C}{V_L}) \tag{2.3}$$

A_C, A_L and A_P are the areas of the central source, local background and particle background regions, with V_C and V_L the average vignetting functions within the central source and LBG regions. The background spectrum used for each fit was the sum of the LBG and PBG spectra, each scaled by the above factors.

The same procedures are applicable to both MOS and pn spectral fitting. For our analysis, we have primarily used pn spectral data, since the signal-to-noise obtained in the soft energy band was far superior than for either of the MOS cameras.

2.2.6 Radial analysis

A major focus of our analysis is the relationship between the unresolved soft X-ray emission in galactic disks and star formation rate, as measured through emission in the FUV band. Throughout this thesis, we study this both qualitatively (through examination of the visual correlation between emission in the two bands) and quantitatively. To do the latter, we extract radial profiles of the soft X-ray data for each galaxy and compare them with FUV radial analysis performed by Muñoz-Mateos et al. (2007).

The 0.3-1.0 keV X-ray image used for this analysis is constructed by the method detailed in §2.2.4, with the simulated image subtracted and source mask imposed. We evaluate the mean soft X-ray count-rate per pixel from concentric annuli extending from the galactic nucleus at intervals of $20''$. This count-rate is converted to flux on the basis of the derived spectral model for the unresolved emission in the target galaxy, and is finally converted to an X-ray luminosity per unit area (pc^2) in the target galactic disk, so as to be directly comparable to the SFR density derived in the FUV band.

Muñoz-Mateos et al. (2007) contains radial profiles of the GALEX FUV magnitude of each of the galactic disks studied at intervals of $6''$, along with the best exponential SFR fit to this profile (quoted in units of $\mathrm{M_{\odot}pc^{-2}yr^{-1}}$). The relationship between the SFR and FUV magnitude is taken from Kennicutt (1998):

$$log(SFR)(\mathrm{M_{\odot}}/yr) = 2log\ d(pc) - 0.4FUV + 9.216 \tag{2.4}$$

where FUV is the FUV AB magnitude and d is the distance to the galaxy. In order to obtain the accurate SFR density (in units of $\mathrm{M_{\odot}pc^{-2}yr^{-1}}$) across the disk, we convert the derived exponential SFR fit (from Muñoz-Mateos et al. (2007)) to the predicted FUV magnitude at that radius. This predicted magnitude is compared to the observed magnitude, and the difference is evaluated as a ratio. This ratio is applied to the exponential SFR fit for each radius point to give the observed SFR per unit area at that radius. Finally, we resample the SFR density to the same radial resolution as the X-ray data. This allows us to obtain a valid measurement of the X-ray/SFR ratio with radius across each of the galactic disks.

Chapter 3

XMM-NEWTON analysis of X-ray emission from the Extended Disks of Spiral Galaxies

3.1 Introduction

The first detailed studies of the X-ray emission from nearby late-type galaxies were carried out with the *Einstein* observatory and revealed both individual luminous X-ray sources, as well as an extended, often complex, underlying structure (Fabbiano 1989). In a number of near edge-on star-forming systems. such as M82 (Watson et al. 1984), evidence was also found for hot outflowing winds. The superior spatial resolution and enhanced soft X-ray response of *ROSAT* greatly extended this work, leading to the detection of substantial numbers of discrete sources as well as establishing a much clearer picture of the diffuse emission components (*e.g.* Read et al. 1997). More recently the advent of *XMM-Newton* and *Chandra* has extended our knowledge of the discrete X-ray source populations and the ultrahot ISM in nearby galaxies to unprecedented luminosity and surface brightness thresholds (*e.g.* Strickland et al. 2004a; Colbert et al. 2004; Pietsch et al. 2004; Fabbiano 2006; Yang et al. 2007; Bogdán & Gilfanov 2008; Bauer et al. 2008).

The diffuse X-ray emission associated with the disks of spiral galaxies is believed to arise in gas heated by shocks generated as a result of supernova explosions and stellar wind interactions (Chevalier & Clegg 1985; Strickland et al. 2000; Suchkov et al. 1994; Grimes et al. 2005). This is supported by

Table 3.1: Properties of the sample of galaxies.

Galaxy	Hubble Type [a]	Distance [b] (Mpc)	D_{25} [a] ($'$)	Inclination [b] ($^{\circ}$)	Foreground N_H [c] (10^{20} cm^{-2})	Nucleus
NGC300	SA(s)d	2.0	21.8	30	3.6	-
M74	SA(s)c	11.0	10.5	7	4.8	-
NGC3184	SAB(rs)cd	11.6	7.2	< 24	1.0	-
M51	SA(s)bc	8.4	7.3	20	1.8	Sy 2
M83	SAB(s)c	4.5	12.9	24	3.9	Starburst
M101	SAB(rs)cd	7.2	26.9	18	1.1	-

[a] - Hubble type and the major-axis diameter (D_{25}) from the RC3 catalogue (de Vaucouleurs et al. 1991).

[b] - See §3.4.2 for references.

[c] - N_H values based on Dickey & Lockman (1990).

analysis of the X-ray spectra of individual shell-type supernova remnants (SNRs) of reasonable age, which are often characterised by plasma temperatures in the range 0.2-0.8 keV, similar to the values obtained when studying larger-scale structures in galactic disks. Strickland et al. (2004a) showed that the luminosity of the diffuse X-ray emission observed in star-forming galaxies is proportional to the rate of mechanical energy injection into the ISM from young stars. Mas-Hesse et al. (2008) further found that the ratio of the soft X-ray luminosity to far infrared luminosity, taking the latter as a proxy for the star-formation rate (SFR), is strongly dependent on the efficiency with which mechanical energy is converted into soft X-rays and also the evolutionary status of the star formation episode. This all argues for a close connection between soft X-ray emission and star formation in late-type galaxies.

A recent study of a sample of 12 nearby spiral galaxies using *Chandra* (Tyler et al. 2004) has shown strong correlation between soft diffuse X-ray emission and sites of recent star formation in spiral arms traced by mid-infrared and Hα emission. A similar investigation has not been completed using *XMM-Newton*, but a number of studies of individual spiral galaxies have been reported (Pietsch et al. 2001; Takahashi et al. 2004; Trudolyubov et al. 2005; Warwick et al. 2007), which again demonstrate the strong linkage between tracers of star formation and diffuse X-ray emission. Furthermore, a dual-component thermal model, with characteristic temperatures of ~ 0.2 keV and 0.6–0.7 keV, very often provides a good description of the spectrum of the diffuse X-ray emission. Studies of the point source X-ray luminosity function (XLF) in spiral galaxies (Tennant et al. 2001; Soria & Wu 2003; Colbert

Table 3.2: Details of the *XMM-Newton* observations of the five new galaxies in our sample.

Galaxy	Observation ID	Start Date	Filter [a]	Target co-ordinates [b]		Useful exposure (ks)	
		(yyyy-mm-dd)	pn/MOS1/MOS2	RA (J2000)	Dec (J2000)	pn	MOS 1+2
NGC300	0112800201	2000-12-26	M/M/M	$00^h54^m55.0^s$	$-37^\circ\ 41'\ 00''$	29.4	65.1
	0112800101	2001-01-01	M/M/M			40.4	88.4
	0305860401	2005-05-22	M/M/M			27.2	64.9
	0305860301	2005-11-25	M/M/M			30.4	68.2
M74	0154350101	2002-02-02	T/T/T	$01^h36^m23.9^s$	$+15^\circ\ 45'\ 13''$	23.3	49.9
	0154350201	2003-01-07	T/T/T			23.5	50.2
NGC3184	0028740301	2001-11-02	T/T/T	$10^h18^m40.0^s$	$+41^\circ\ 25'\ 11''$	19.9	49.9
M51	0112840201	2003-01-15	T/T/T	$13^h29^m51.9^s$	$+47^\circ\ 10'\ 32''$	18.8	40.6
	0212480801	2005-07-01	M/M/M			20.4	56.7
	0303420101	2006-05-20	T/T/T			32.3	77.3
	0303420201	2006-05-24	T/T/T			14.1	43.0
M83	0110910201	2003-02-18	T/M/M	$13^h37^m00.4^s$	$-29^\circ\ 52'\ 04''$	18.3	38.2

[a] - T = thin filter, M = medium filter.

[b] - Assumed position of the galactic nucleus.

et al. 2004) have shown that the brightest point sources contain the bulk of the integrated point source luminosity, suggesting that, provided a sufficient number of the brightest point sources are excluded, it should in principle be possible to probe the underlying structure of the galaxy to relatively low levels of surface brightness.

In this chapter, we focus on the spectral and morphological properties of the diffuse X-ray emission emanating from the extended disks of late-type normal galaxies, as deduced from *XMM-Newton* observations. In §3.2, we identify a sample of nearby galaxies with close to face-on disks of sufficient angular extent so as to be readily amenable for study with *XMM-Newton*. We then outline the data reduction methods employed (§3.3). Using image analysis, we sub-divide the total X-ray luminosity of each galaxy into the contribution of spatially resolved bright sources and a *residual* component comprising the integrated emission of unresolved point sources and the diffuse galactic emission (§3.4). On the basis of published source luminosity functions, we estimate the likely contribution of truly diffuse emission to this *residual* signal. We go on to investigate spectral properties of both the bright source and the unresolved (residual) components (§3.5). We also consider the morphology of the residual emission in the context of the star formation evident in the galactic disks (§3.6). Finally we discuss the implication of our results (§3.7) and briefly summarise our conclusions (§3.8). The research presented in this chapter has been published in Owen & Warwick (2009).

3.2 Galaxy Sample and Observations

In this chapter we investigate the large-scale spatial and spectral properties of the X-ray emission emanating from the extended disks of six nearby late-type spiral galaxies. The galaxies in question are NGC300, M74, NGC3814, M51, M83 and M101, brief details of which are given in Table 3.1. In a previous paper (Warwick et al. 2007; hereafter W07), we reported the results of an *XMM-Newton* study of one of these galaxies, namely M101, and here we apply a similar methodology to extend the sample, thereby allowing the intercomparison of the galaxy X-ray characteristics based on *XMM-Newton* observations.

When dealing with X-ray spectral imaging data of only moderate spatial resolution (as afforded by *XMM-Newton*), the presence of a number of very bright point sources has the potential to obscure the properties of the underlying galaxy. Since our goal is to study the latter rather than the former, we have limited our galaxy sample to nearby face-on systems of Hubble type Sbc-Sd with major-axis D_{25} extent greater than $7'$, thereby ameliorating the source confusion problem. In order to study the soft X-ray emission present, we also required a low foreground Galactic column density ($< 10^{21}$ cm^{-2}). 30-40 galaxies in the RC3 catalogue (de Vaucouleurs et al. 1991) met the requirements to be included in our sample, of which only the above sample had significant enough *XMM-Newton* exposure time to be utilised here. We have excluded M33 from our initial study since this galaxy has a D_{25} diameter of $70'$ and thus extends well beyond the EPIC field of view. M33 is the subject of a specific *XMM-Newton* programme utilising multiple pointings (Pietsch et al. 2004; Misanovic et al. 2006) and more complex methods are therefore necessary for performing imaging and spectral analysis. We undertake an individual study of this galaxy in Chapter 5.

Details of the *XMM-Newton* EPIC observations of the five new additions to our galaxy sample are summarised in Table 3.2.

3.3 Data Reduction

The data reduction was based on SAS v8.0. The datasets were initially screened for periods of high background by accumulating full-field 10–15 keV light curves. MOS data were excluded during periods when the 10-15 keV count rate averaged over 100 s bins exceeded 0.2 $\mathrm{ct\ s^{-1}}$, and the pn data were similarly excised when the pn count rate exceeded 2 $\mathrm{ct\ s^{-1}}$. As summarised in Table 3.2, the exposure times after event filtering within individual observations ranged from 14 to 40 ks in the pn camera (with typically slightly greater exposure in the MOS cameras).

3.3.1 Image Construction

A set of pn+MOS images were produced in three energy bands (0.3-1 keV, 1-2 keV and 2-6 keV) using the methodology detailed in §2.2. Where there was more than one observation, the images pertaining to a given instrument and band were combined into a single mosaiced image.

Figures 3.1 - 3.3 show the soft-band images derived for each of the five new galaxies, together with the corresponding data for M101 from W07. In the case of M74, NGC3184, M51 and M83 our analysis pertains to circular regions centred on the galactic nucleus of diameter equal to the major-axis D_{25} dimension, whereas for NGC 300, given the relatively low X-ray surface brightness, we restrict our attention to a central $10'$ diameter region (0.46 of the D_{25} extent). Similarly for M101 the X-ray analysis reported in W07 applies to a central $20'$ diameter region (0.74 of the D_{25} dimension). Hereafter we refer to these galaxy-centred circular regions as the "X-ray extraction regions".

3.3.2 Spatial masking of bright sources

In order to produce a spatial mask to suppress the bright source contamination it was necessary to construct a catalogue of the bright sources associated with each galaxy. The starting point was a preliminary source-list for each galaxy derived from the second *XMM-Newton* Serendipitous Source Catalogue (2XMM; Watson et al. 2009), encompassing those sources located within the galaxy extraction region (as defined above). A master source-list for each galaxy was produced following the method described in §2.2.3.

In the case of both M83 and NGC 300 two additional sources, not included in the 2XMM catalogue, but clearly present in the images at count-rates above the threshold were added by hand. Similarly in the case of M51 one additional source was added. These sources were missed by the 2XMM catalogue due to confusion between the source and surrounding extended galactic emission. The number of sources included in each master source-list is given in Table 3.3, together with the threshold setting (quoted as the equivalent unabsorbed source luminosity in the 0.3–6 keV band on the basis of a source spectrum consisting of a power-law continuum with $\Gamma = 1.7$ absorbed by the Galactic foreground N_H). At this stage we also determined the count rates for each source in the soft, medium and hard bands by applying the above process to the appropriate pn+MOS sub-band images.

The next step involved the creation of the spatial mask, using the method illustrated in §2.2.4. Figure 3.4 shows the simulated "bright source image" derived using the above procedure for M83. In this example, the bright source mask was obtained by applying a surface brightness cut to the image at a level of 0.07 pn+MOS1+MOS2 $\mathrm{ct\ ks^{-1}\ pixel^{-1}}$, leading to a "spillover" fraction, (*i.e.,* the fraction of the bright source signal not contained within the masked region) of 9%. Similar surface brightness cuts were applied to the other galaxies resulting in spill-over fractions in the range 9-12%.

The derived spatial masks were used to separate the "bright source region" from the "residual emission

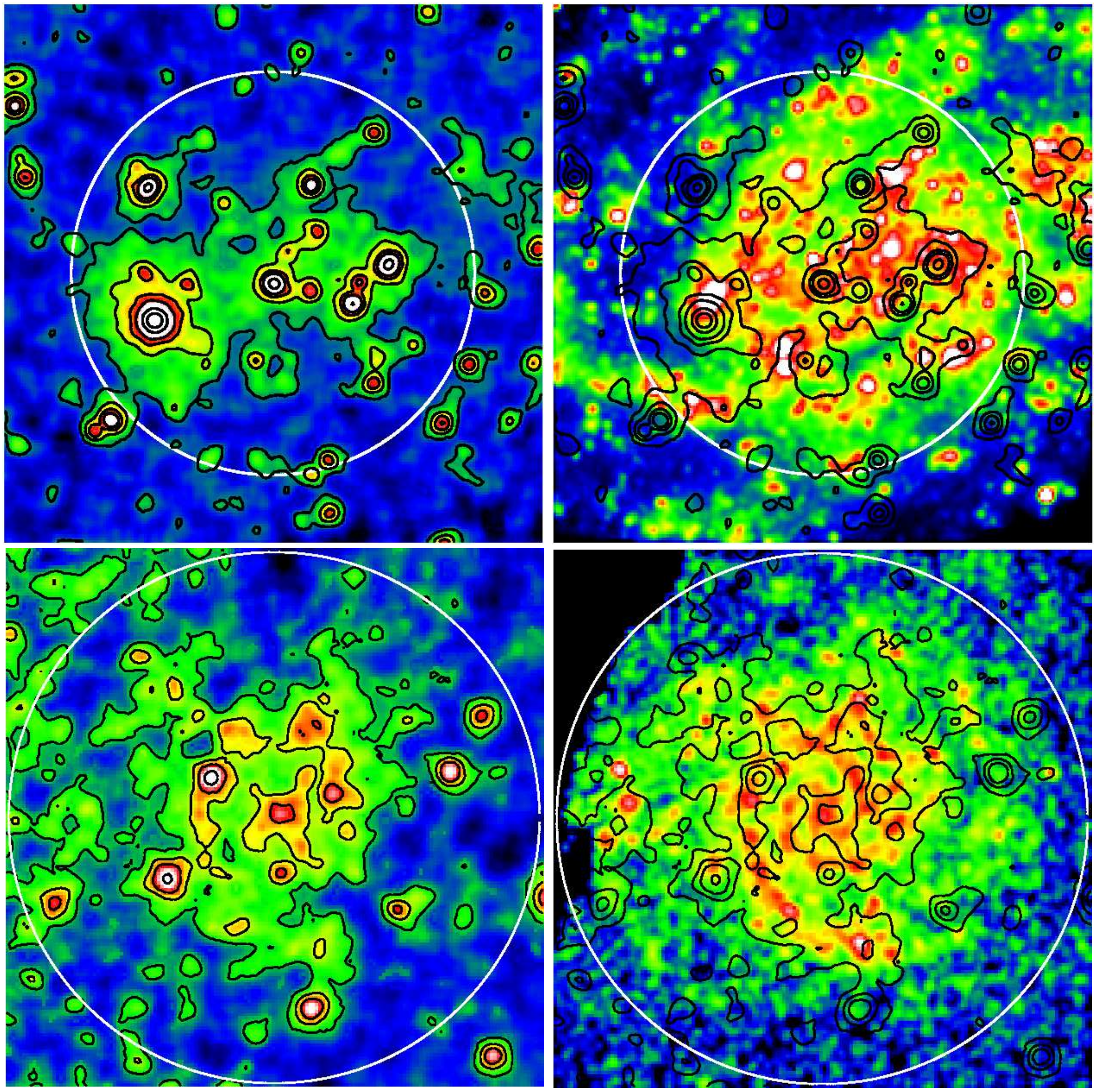

Figure 3.1: Comparison of the soft X-ray and far-ultraviolet images of three galaxies. *Left-hand panels:* Adaptively smoothed versions of the *XMM-Newton* pn+MOS images in the soft (0.3-1 keV) band. The amplitude scaling in all cases is logarithmic with the contour levels representing factor two steps in the soft X-ray surface brightness. *Right-hand panels:* The *GALEX* FUV ($\lambda_{eff} = 1528$ Å) image on the same spatial scale as the X-ray data (except for NGC 3184 where the UV data are from the *XMM-Newton* Optical Monitor in the UVW1 (≈ 2680 Å) band. The amplitude scaling is again logarithmic. The contours show the soft X-ray morphology for comparison purposes. *Top panels:* NGC 300. The circle has a diameter of $10'$. *Bottom panels:* M74. The circle has a diameter of $10.5'$.

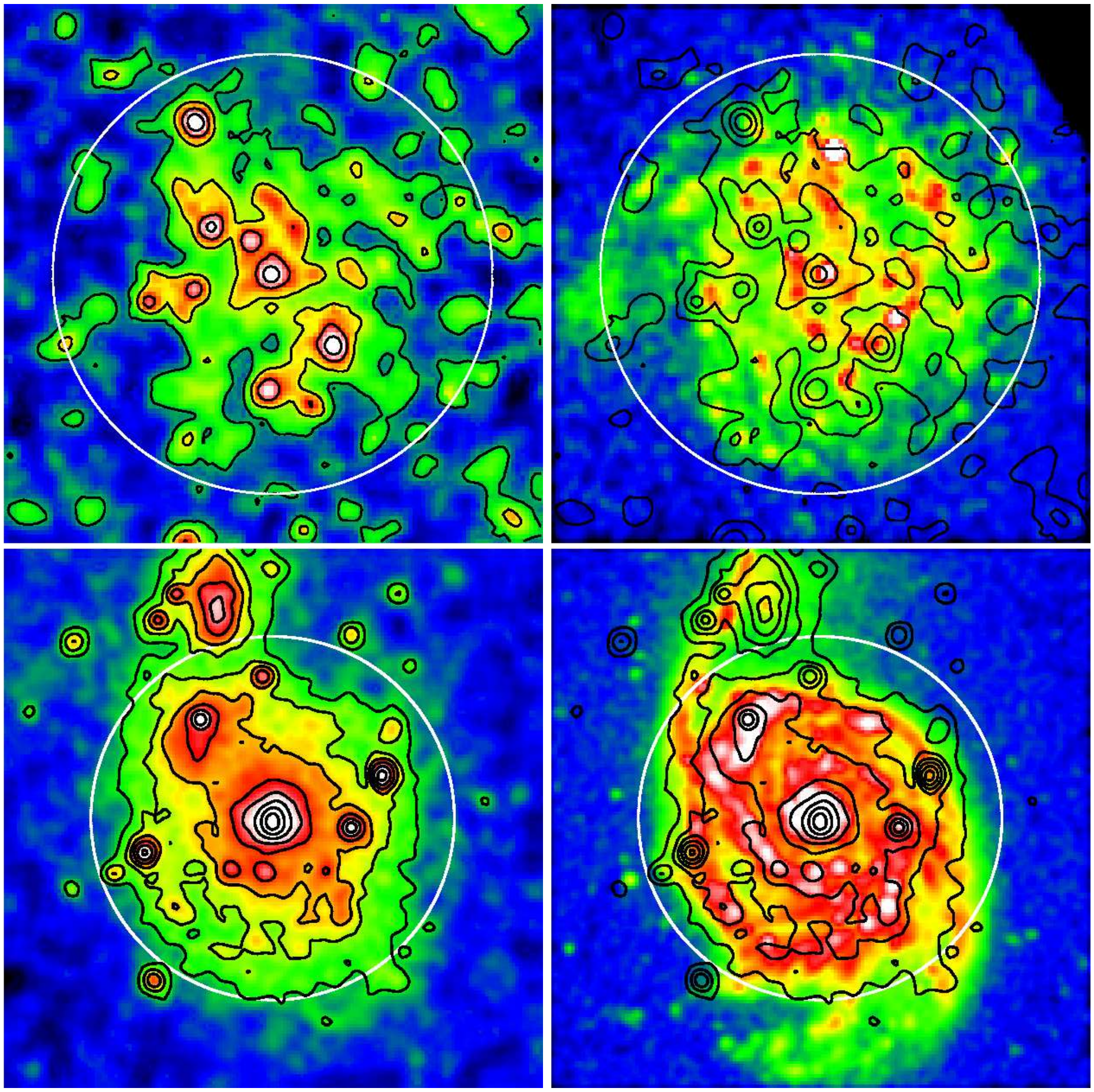

Figure 3.2: As for Fig. 3.1. *Bottom panels:* NGC3184. The circle has a diameter of 7.2′. *Bottom panels:* M51. The circle has a diameter of 7.3′.

region" in both the spatial and spectral analysis. In order to study the spatial distribution of the residual emission (see §3.6), a simulated image representative of the soft band data was subtracted from the corresponding pn+MOS image and the source mask imposed - see Figure 3.4. This process serves to suppress much of the "contamination" arising from the brightest sources in the galaxy, including the bulk of the spillover into the residual galaxy region. Note that a slightly different approach is necessary in the spectral analysis; here we take account of the bright source signal spilling into the residual emission region by including an appropriate fraction of the bright source spectral model in the spectral fit of the residual emission - see §3.5.2.

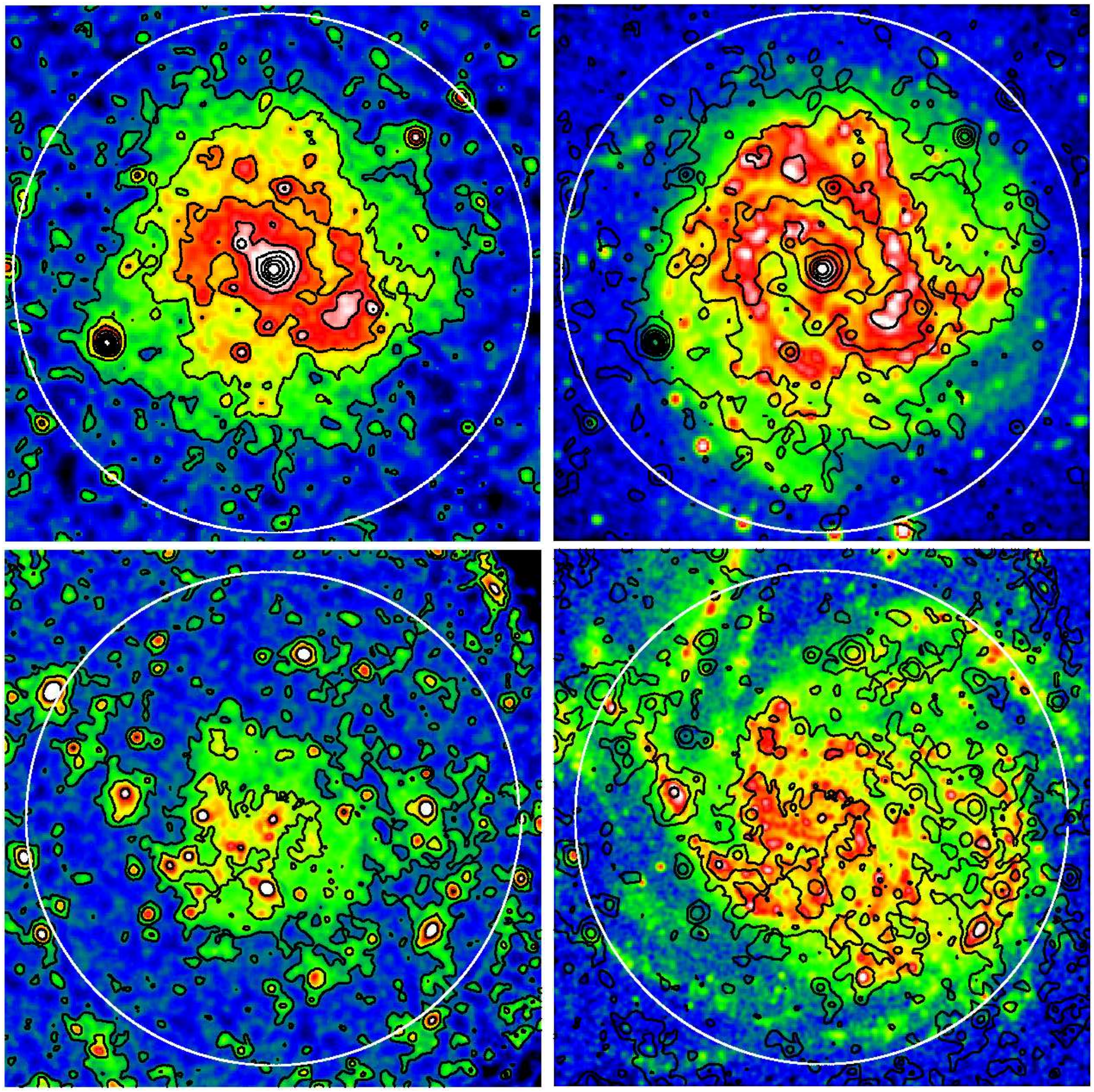

Figure 3.3: As for Fig. 3.1. *Top panels:* M83. The circle has a diameter of 12.9′. *Bottom panels:* M101. The circle has a diameter of 20′.

3.3.3 Spectral Extraction

The soft-band images shown in Fig. 3.1–3.3 demonstrate the existence of an extended emission component in addition to the population of bright point sources. On the basis of the approach described earlier, we extracted the integrated spectrum of both the bright source region (bounded by the spatial mask) and the residual emission region (corresponding to the full X-ray extraction region less the masked area).

The relatively large extent and complicated shapes of the bright source and residual emission regions makes the evaluation of the background subtraction somewhat more complicated than with most *XMM*-

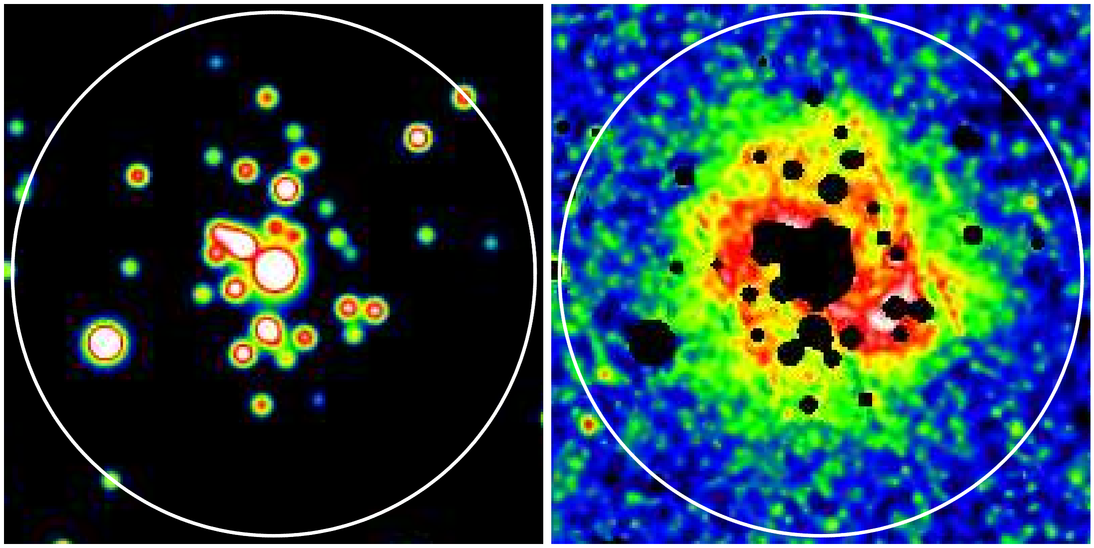

Figure 3.4: *Left panel:* The modelled "bright source" image constructed for M83 from a set of count-rate scaled PSF sub-images. A source mask was produced by thresholding this image at a surface brightness level such that 91% of the source signal was contained within the resulting mask. *Right panel:* The soft-band image of the residual emission in M83 obtained from the full image by subtracting the bright source model and then applying the spatial mask. Much of the "contamination" due to bright sources is suppressed by this process. In both panels the circle has a diameter of $12.9'$.

Table 3.3: Characteristics of the bright X-ray source population in each galaxy.

Galaxy	X-ray Region^a ($'$)	Threshold $L_X{}^b$ (10^{37} erg s^{-1})	Number in Source List	Number of high L_X sources ($L_X > 5 \times 10^{38}$ erg s^{-1})
NGC300	10.0	0.2	22	0
M74	10.5	5.0	20	4
NGC3184	7.2	6.0	18	4
M51	7.3	4.0	26	6
M83	12.9	2.0	40	2

^{a} - Diameter of the "X-ray extraction region".

^{b} - Nominal L_X threshold applied in the 0.3–6 keV band in defining sample.

Table 3.4: Contribution of point sources to the total X-ray luminosity.

Galaxy	Spillover/Area Factors (%)	Component	$L_X(10^{39}$ erg s$^{-1})$ (0.3-1 keV)	(1-2 keV)	(2-6 keV)	(0.3-6 keV)
NGC300	12/7	Bright Sources	0.19	0.07	0.25	0.51
		Unresolved Sources	[0.02]	[0.01]	[0.03]	
		Residual Galaxy	0.05	-	-	0.05
		Total Measured	0.24	0.07	0.25	0.56
M74	11/24	Bright Sources	1.4	1.3	3.0	5.7
		Unresolved Sources	[0.5]	[0.4]	[0.8]	
		Residual Galaxy	1.4	0.7	-	2.1
		Total Measured	2.8	2.0	3.0	7.8
NGC3184	9/22	Bright Sources	1.2	1.4	3.4	6.0
		Unresolved Sources	[0.6]	[0.5]	[0.9]	
		Residual Galaxy	2.0	0.5	-	2.5
		Total Measured	3.2	1.9	3.4	8.5
M51	12/24	Bright Sources	6.8	3.8	6.5	17.1
		Unresolved Sources	[0.5]	[0.4]	[0.8]	
		Residual Galaxy	6.3	0.9	-	7.2
		Total Measured	13.1	4.7	6.5	22.3
M83	9/30	Bright Sources	2.5	2.0	3.1	7.6
		Unresolved Sources	[0.5]	[0.4]	[0.9]	
		Residual Galaxy	3.3	0.7	-	4.0
		Total Measured	5.8	2.7	3.1	11.6

Newton data. In this context, the use of "blank-sky" *XMM* fields to produce a background spectrum would be far from ideal, because the sky X-ray background in the soft band varies from field to field, and this is a vital component of the total background signal we wish to subtract. Instead, we extracted spectra from both an annulus surrounding the defined galaxy region and also from the corner regions of each detector not exposed to the sky. By using an appropriate scaling of these spectra, using the method detailed in Chapter 2, an appropriate model background spectrum can then be produced. The SAS tools *arfgen* and *rmfgen* were used to produce appropriate Auxiliary Response File (ARF) and Response Matrix File (RMF) files for the source and residual galaxy regions. Finally, the counts recorded in adjacent (raw) spectral channels were summed to give a minimum of 20 counts per spectral bin in the final set of spectra.

3.4 Overview of the galactic X-ray properties

3.4.1 The contribution of luminous point sources

By application of the spatial mask described earlier, we are able to measure the count rates (above the local background) in the soft, medium and hard band images associated with both the "bright source regions" and the "residual emission regions" (hereafter we refer to the latter as the "residual galaxy"). Table 3.4 summarises the results for each of the five new galaxies in our sample. Here we have converted the measured count rates to equivalent fluxes in the band on the basis of a specific spectral model and then transposed from flux to luminosity using the distances quoted in Table 3.1. The tabulated count-rates and luminosities of the bright source populations in the sample (excluding M101, for which this information has been published in Warwick et al. (2007)) are given in the Appendix. For the bright source regions we assume a spectral model consisting of a power-law continuum with photon index $\Gamma = 1.7$ modified by the foreground absorption in our Galaxy. For the residual galaxy we use the model which best fits the actual spectrum of this component, as derived in §3.5.2. The quoted X-ray luminosities (L_X) have been corrected for foreground absorption, that is they are unabsorbed values.

The L_X values reported in Table 3.4 have been corrected for two further effects. The first is the spillover of bright source flux into the residual galaxy region (discussed earlier). The second correction relates to the fact that the bright source mask obscures a sizeable fraction of the galaxy disk. To correct for this, we have scaled up the residual galaxy component by a factor derived from interpolating the azimuthally-averaged brightness distribution (as represented by the radial distributions of the X-ray surface brightness discussed in §3.6) into the masked regions. The spillover fraction and the area correction factor applicable to each galaxy are listed in Table 3.4.

The results in Table 3.4 demonstrate that whereas the set of very luminous sources represented by our bright source sample provide the dominant contribution to the total galactic X-ray luminosity above 2 keV, at lower energies, and particularly below 1 keV, the split between the bright source and residual galaxy contributions is more balanced, albeit with the exception of NGC 300. For the latter galaxy, we were able to set a much lower threshold for bright source removal than was possible for the other galaxies in the sample (on account of the relatively proximity of NGC 300 - see Table 3.1). In other words a higher fraction of the integrated X-ray flux from point sources was resolved in this galaxy. However, we show later (see §3.6) that the low surface brightness inferred for the underlying diffuse X-ray emission in NGC 300 is mostly likely due to the low SFR density in this Galaxy rather than being simply a consequence of a more stringent source rejection threshold. For M74, NGC 3184, M51 and M83 a broadly similar source detection threshold transposes to luminosity thresholds for source exclusion ranging from 2.0×10^{37} erg s^{-1} (for M83) up to 6.0×10^{37} erg s^{-1} (for NGC 3184). The likely contribution of unresolved sources to the residual galaxy emission in each case is investigated below and a correction to a fixed luminosity threshold is applied later in the analysis (see §3.7).

As a further exercise it is possible to estimate the likely contribution to the residual galaxy emission of an unresolved population of somewhat less luminous sources with spectral characteristics and distribution similar to the sources represented in the bright source list. Here we make use of recent results from *Chandra*, which show that the discrete source luminosity function appropriate to the disk regions of spiral galaxies typically takes the form of a power-law with a slope in the range -0.5 to -0.8 (in the cumulative form). For example, Tennant et al. (2001) quote a slope of -0.5 for the disk sources in M81, whereas Doane et al. (2004) measure -0.6 for NGC 3184 and Pence et al. (2001) report -0.8 for M101. Soria & Wu (2003) examine the $\log N - \log S$ relation for relatively faint HMXBs in the disk of M83 and find a broken power-law provides a reasonable fit to the data, with a low-luminosity index of -0.6. Also Colbert et al. (2004) measure a similar range of power-law slopes for the source luminosity function within a relatively large sample of spiral galaxies. The flatness of this form means that relatively small numbers of very luminous sources provide the bulk of the integrated luminosity residing in discrete sources. Furthermore, in the context of providing a rough estimate of the contribution of unresolved sources to the residual galaxy signal, it implies that we can, in principle, extrapolate below our source detection threshold to arbitrarily faint levels (assuming of course that the slope of the luminosity function remains constant over an appropriately wide range of source luminosity).

Here we make the assumption that the slope of the source luminosity function is -0.6 across the set of galaxies and over a wide luminosity range. We then use the number of bright sources actually observed in the galaxy from the threshold luminosity up to a fixed upper cut-off (set here as $\mathrm{L_X}= 5\times10^{38}$ erg s^{-1} - see Table 3.3), to define the normalization of the source luminosity function for that particular galaxy. We first calculate the integrated emission of unresolved sources in the broad 0.3-6 keV band and then, on the basis of the bright source spectral model noted earlier, split this into soft-, medium- and hard-band contributions. The entries in Table 3.4 under the heading "unresolved sources" summarises the results on a galaxy by galaxy basis. In the soft band, which is the focus of our attention in describing the X-ray morphology and the linkage of X-ray emission to star formation, the potential contribution of unresolved, but relatively luminous, source populations to the measured residual galaxy emission ranges from as low as $\sim 10\%$ in M51 up to $\sim 40\%$ in NGC300. By implication the bulk of the residual galaxy luminosity in this band must reside in some combination of: (i) truly diffuse X-ray emission associated with the galaxy disk presumably resulting from the energy input of supernova and stellar winds and (ii) the integrated emission of populations of relatively soft spectrum, lower-luminosity sources such as supernova remnants, cataclysmic variables, active binaries and stellar coronal sources, populations which are not well represented in the bright-source (*i.e.,* high $\mathrm{L_X}$) samples. There is also a potential contribution from a putative extended galactic halo, which is often seen in edge-on galaxies; however the face-on aspect of the present galaxies suggests that a very extended halo component will be difficult to distinguish from the components confined to the disk.

3.4.2 X-ray characteristics of the individual galaxies

Figures 3.1 - 3.3 compare the galaxy morphology observed in soft X-rays with that measured in the far ultraviolet FUV ($\lambda_{eff} \approx 1528$ Å) band by *GALEX*[1], although in the case of NGC 3184 we use the *XMM-Newton* Optical Monitor UVW1 (≈ 2680 Å) image recorded in the same observation as the X-ray data (see Table 3.2) to make this comparison. In all cases the the UV images were lightly smoothed with a circular gaussian mask with $\sigma = 4''$. In a number of the galaxies, particularly M74, M83 and M101,

[1]The *GALEX* images were obtained from the public archive at http://galex.stsci.edu/GR2/

the X-ray emission traces segments of the inner spiral arms which are delineated as very pronounced features in the FUV images. In all cases the central concentration of the soft X-ray emission and its fall-off with increasing galactocentric radius is quite well matched to the surface brightness distribution measured in the FUV channel. This general correlation of soft X-ray and FUV light immediately establishes the close connection of a significant component of the X-ray emission with recent star-formation in these late-type systems. We explore the linkage between the X-ray emission and star-formation in more detail in §3.6. Here we briefly comment on each of these galaxies, in the context of their extended X-ray emitting components.

NGC 300

NGC300 is an SA(s)d spiral seen at low inclination ($i = 30^\circ$; de Vaucouleurs et al. 1991) at a distance of 2.0 Mpc (Freedman et al. 2001). Many large HII regions are visible throughout the galaxy, and there is evidence that the galaxy has experienced many episodes of star formation. However, star formation in the central regions appears to be suppressed in recent times, with a small population of stars present in the central arcminute of the galaxy with ages below 1 Gyr (Davidge 1998). There is clear evidence of spiral structure, although the contrast between "arm" and "off-arm" regions in the galaxy is low. In X-rays NGC300 has been studied by *ROSAT* (Read & Pietsch 2001) and more recently by *XMM-Newton* (Carpano et al. 2005). Carpano et al. (2005) report the presence of diffuse emission in the galactic disk of NGC 300 with $\mathrm{L_X} < 10^{38}$ erg s^{-1} and temperatures of ≈ 0.2 and ≈ 0.8 keV. Its X-ray source population contains 86 sources detected by *XMM-Newton* above $\mathrm{L_X} > 10^{36}$ erg s^{-1} (0.3-6 keV), the brightest of which is detected with a luminosity of 1.8×10^{38} erg s^{-1}, close to the Eddington limit for a $1.4\ \mathrm{M_\odot}$ object. The optical counterpart of this latter source has been identified as a Wolf-Rayet star (Carpano et al. 2005). The source population includes 12 suspected SNRs, with the remainder attributed to X-ray binary systems or background AGN. In the current paper we determine the aggregate luminosity of the 20 brightest point sources within the central $5'$ of NGC300 to be $\mathrm{L_X} \approx 5 \times 10^{38}$ erg s^{-1}, in agreement with earlier studies. The count-rates for these sources are shown in Table A.1. We estimate the X-ray luminosity of the residual emission to be $\approx 5 \times 10^{37}$ erg s^{-1} (0.3–1 keV). The surface brightness of this component is extremely low but appears to trace a central bar-like structure and to extend out to at least a distance of 2.5 kpc ($4'$).

M74

M74 (NGC 628) is an SA(s)c spiral seen almost face-on ($i = 7°$; Shostak & van der Kruit 1984) at a distance of 11 Mpc (Gil de Paz et al. 2007). The nuclear region of the galaxy is characterised by strong HII emission with no evidence for the presence of an AGN. A grand-design twin-armed spiral structure is observed. In X-rays M74 has been studied by both *Chandra* (Krauss et al. 2005) and *XMM-Newton* (Soria & Kong 2002; Soria et al. 2004), albeit with little attention, to date, on the diffuse X-ray component. Its X-ray source population includes two ultraluminous X-ray sources (ULXs) with $L_X > 10^{39}$ erg s^{-1} (0.3-6 keV), which show long-term variability, and which represent the most luminous subset of a sample of ≈ 20 sources with $L_X > 10^{38}$ erg s^{-1} distributed across the galactic disk. Soria et al. (2004) report that the spectrum of the brightest X-ray source is consistent with a HMXB in an active star-forming region. Seven of the 74 point sources detected in either *XMM-Newton* or *Chandra* observations are found to have very soft spectra and to be candidate X-ray SNRs, with the remainder either X-ray binary systems or background AGN. These soft sources all have $L_X < 10^{38}$ erg s^{-1}. In the present analysis we confirm the presence of an extensive discrete source population in M74 with an aggregate luminosity in the 20 brightest point sources amounting to 5.7×10^{39} erg s^{-1}. The count-rates for these sources are shown in Table A.2. The underlying residual X-ray emission has a luminosity of 2.1×10^{39} erg s^{-1}. This component traces the inner spiral arm structure and is evident out to a distance of 9 kpc ($3'$), at which point it falls below the background level.

NGC 3184

NGC3184 is an SAB(rs)cd barred spiral seen at low inclination ($i < 24°$; Lyon-Meudon Extragalactic Database [LEDA][2]) at a distance of 11.6 Mpc (Leonard et al. 2002). The nuclear region of the galaxy is dominated by HII emission with no compelling evidence for an AGN (Doane et al. 2004). Grand-design twin spiral arms are observed, although the contrast in brightness between "arm" and "off-arm" regions in the galaxy is low. A type-II supernova, (SN1999gi) has been observed in the northern spiral arm close to the centre of the galaxy. In X-rays NGC3184 has been studied by *Chandra* with an emphasis on both the point source population (Colbert et al. 2004) and the diffuse X-ray emitting gas (Doane et al. 2004; Tyler et al. 2004). Its X-ray source population contains ≈ 15 sources with $L_X > 10^{38}$ erg s^{-1}, including two ULXs with $L_X > 10^{39}$ erg s^{-1} (0.3-6 keV). SN1999gi is detected

[2]at http://leda.univ-lyon1.fr

with $L_X \approx 10^{38}$ erg s^{-1}. The diffuse X-ray emission shows a strong correlation with regions which are bright in Hα (Tyler et al. 2004). Doane et al. (2004) report the presence of diffuse X-ray emission concentrated in areas of younger stellar populations and star-forming regions, with a surface brightness five times greater in spiral arm regions than in off-arm regions. The spectrum of the diffuse emission in the galactic disk can be well fitted with a two-temperature thermal model with kT of 0.13 keV and 0.43 keV (Doane et al. 2004). In the present study we measure the aggregate luminosity of the 18 brightest point sources to be $\approx 6 \times 10^{39}$ erg s^{-1}, consistent with earlier *Chandra* estimates (Colbert et al. 2004). The count-rates for these sources are shown in Table A.3. The residual X-ray emission has an X-ray luminosity of 2.5×10^{39} erg s^{-1} and extends from the nucleus out to a distance of 8 kpc ($2.5'$).

M51

M51 (NGC5194) is an SA(s)bc spiral seen almost face-on ($i = 20°$; Tully 1974) at a distance of 8.4 Mpc (Feldmeier et al. 1997). It hosts a low-luminosity active galactic nucleus, which shows optical emission lines and is classified as a Seyfert 2 (Stauffer 1982; Ho et al. 1997). Kohno et al. (1996) use observations of a nuclear molecular disk to constrain the dynamical mass within 70 pc of the nucleus to be $4 - 7 \times 10^6$ $M_\odot$, indicating the presence of a black hole with comparable mass to many AGNs. M51 is interacting tidally with a companion SB0/a galaxy (NGC5195), and both systems are seen to contain starburst activity. There is grand-design twin-arm spiral structure present. In X-rays M51 has been studied by *Einstein* (Palumbo et al. 1985), *ROSAT* (Marston et al. 1995; Ehle et al. 1995), *ASCA* (Terashima et al. 1998) and more recently by *Chandra* (Terashima & Wilson 2004; Colbert et al. 2004; Tyler et al. 2004) and *XMM-Newton* (Dewangan et al. 2005). Studies have also been carried out at higher X-ray energies by *BeppoSAX* (Fukazawa et al. 2001). In addition to the nuclear source, which has an X-ray luminosity of 6.9×10^{39} erg s^{-1} (0.3-10 keV, Dewangan et al. 2005), about 20 sources with $L_X > 10^{38}$ erg s^{-1} are detected including several ULX candidates (with $L_X > 10^{39}$ erg s^{-1}), the bulk of which are located in the spiral arms (Terashima & Wilson 2004). One of these is identified as a supersoft ULX, whilst the others show power-law or multicolour-disk spectra, consistent with stellar mass black holes accreting at super-Eddington rates. The diffuse X-ray emission is well correlated with the radio continuum and mid-infrared emission distributed in the spiral arms establishing a clear link with star formation (Ehle et al. 1995; Tyler et al. 2004). Terashima & Wilson (2004) find that the diffuse X-ray emission in the southern extranuclear cloud is well fitted with a single-temperature thermal model with kT of 0.58 keV. The current analysis confirms the general properties of the galaxy established by the *ROSAT* and *Chandra* observations. The aggregate luminosity of the brightest 25 point sources in M51 is 1.7×10^{40} erg s^{-1} (0.3–6 keV), 28% of which is attributable to the nuclear source. The count-rates for these sources are shown in Table A.4. The luminosity of the nuclear source is measured as $L_X = 4.7 \times 10^{39}$ erg s^{-1} (0.3-6 keV), consistent with previous determinations (Terashima & Wilson 2004; Dewangan et al. 2005). A further 4 sources have luminosities $L_X > 1 \times 10^{39}$ erg s^{-1} meriting a ULX classification. Our analysis reveals residual soft X-ray emission extending from the bright nucleus along the spiral arms out to a distance of 5 kpc ($2.5'$). Lower surface brightness emission from the extended disk is observed out to a radial distance of 9 kpc in all directions, with further X-ray emission joining M51 to its companion galaxy. The X-ray luminosity of the residual component is 7.2×10^{39} erg s^{-1}.

M83

M83 (NGC 5236) is an SAB(s)c barred spiral seen at low inclination ($i = 24°$; Talbot et al. 1979) at a distance of 4.5 Mpc (Thim et al. 2003). It harbours an active nuclear region undergoing a violent starburst, a circumnuclear starburst and grand-design twin-armed spiral structure. There are numerous sites of active star-formation coincident with the spiral arms (Vogler et al. 2005). In X-rays M83 has been studied by *Einstein* (Trinchieri et al. 1985), *ROSAT* (Ehle et al. 1998; Immler et al. 1999), *ASCA* (Okada et al. 1997 and more recently by *Chandra* (Soria & Wu 2002; Soria & Wu 2003; Colbert et al. 2004; Tyler et al. 2004). Its X-ray source population includes at least one ULX, roughly 20 sources with $L_X > 10^{38}$ erg s^{-1}, a luminous source coincident with the infra-red nuclear photometric peak, two bright supersoft sources, two luminous SNR candidates and two candidate X-ray pulsars (Immler et al. 1999; Soria & Wu 2003). On an arcminute scale both the *ROSAT* and *Chandra* X-ray observations trace apparently diffuse emission associated with the inner spiral-arms (Immler et al. 1999; Soria & Wu 2003; Tyler et al. 2004). Immler et al. (1999) report the diffuse emission associated with a cluster of bright HII regions embedded in the south-western spiral arm as having a two-temperature thermal characteristic with kT of 0.26 keV and 0.95 keV. In the present analysis we measure the aggregate luminosity of the bright point sources in M83 to be $L_X = 7.6 \times 10^{39}$ erg s^{-1}, which includes a contribution of 3.1×10^{39} erg s^{-1} from the central region. A comparable estimate of the luminosity is obtained when one sums over the 15 point sources detected by *Chandra* within $15''$ of the dynamical nucleus of the galaxy and include unresolved nuclear emission (Soria & Wu 2002). The bright source luminosity distribution also matches that established in Soria & Wu (2003), with 15 out of the 40 sources in our catalogue having $L_X > 10^{38}$ erg s^{-1} including one ULX. The count-rates for these sources are shown in Table A.5. The *XMM-Newton* soft band image traces emission from the bright nuclear region out along the twin spiral arms to a galactocentric distance of about 4 kpc ($3'$). Extended X-ray emission of relatively low surface brightness can then be further traced out to ~ 8 kpc. The X-ray luminosity of the residual component is 4×10^{39} erg s^{-1}.

3.5 Spectral Analysis

Using the methodology outlined in §3.3.3, spectral datasets were obtained for both the bright-source and the residual-galaxy regions for four galaxies, namely M74, NGC3184, M51 and M83. For simplicity, we based our analysis on a single observation for each galaxy, namely the observation with the deepest pn exposure (see Table 3.2). Due to limited signal-to-noise in the MOS channels, we focus on the spectra derived from the EPIC pn camera, except in the case of M83, where both pn and MOS spectra were fully utilised and in M74 where both datasets were employed in the spectral investigation of its bright-source region. Unfortunately the residual-galaxy emission in NGC 300 was too faint for detailed spectral analysis to be merited. The spectral fitting was carried out using the software package XSPEC Version 12.4.

3.5.1 Spectra of the bright-source regions

The spectra representative of the bright-source regions in M74, NGC3184, M51 and M83 were well fitted with either a simple power-law continuum or a power-law continuum plus an additional solar-abundance thermal plasma component (the MEKAL model in XSPEC). The best-fit photon indices were all in the range 1.55–1.9 with the temperature of the thermal emission typically ≈ 0.65 keV. Fig. 3.5 – 3.8 show the measured spectra, the best-fitting model and residual χ^2 to these best fits. Similarly, Table 3.5 summarises the details of the best-fitting models. After correcting for the flux spillover beyond the spatial mask, the inferred luminosities in the integrated bright-source spectra were found to be in general agreement with the estimates quoted previously based on the image analysis. The photon index observed is typical of the spectra of HMXB and LMXB found in the Local Group (Grimm et al. 2007). The thermal emission associated with the bright-source regions is of similar temperature to the “hot” component observed in the residual-galaxy emission (see below). However, where this component is detected in the bright-source spectra, namely in NGC3184, M51 and M83, it appears at a proportionately higher level than might be inferred based on a simple area scaling with respect to the residual-galaxy emission. There appears to be a genuine excess of hot gas in these regions, which may be attributable to the ISM being hotter in active star forming regions where the majority of the point sources are found.

3.5.2 Spectra of the residual-galaxy regions

Previously we estimated that 9-12 per cent of the counts from the bright sources overspill into the residual-galaxy regions. In carrying out the spectral analysis of the latter we have corrected for this spillover effect, by including an appropriate fraction of the best-fit bright-source model as a fixed component of the spectral model. Visual inspection of the residual-galaxy spectra revealed almost no emission above 1.5 keV in any of the galaxies. It was further found that thermal models comprising either one or two solar-abundance MEKAL components provided a reasonable fit to the residual-galaxy spectra. In all cases a "cool" thermal component was required at kT ≈ 0.2 keV. The spectra with the best signal-to-noise ratio, namely those for M51 and M83, also required a "hot" thermal component at kT ≈ 0.65 keV. These spectral characteristics appear to be quite typical of the diffuse components seen in normal and starburst galaxies (*e.g.,*, Fraternali et al. 2002) and consistent with previously published measurements for several of the galaxies in the sample (*e.g.,* Ehle et al. 1998; Soria & Wu 2003; Kuntz et al. 2003; Carpano et al. 2005; W07). The spectra of M51 and M83 also showed evidence for a "soft excess" which, via spectral fitting, was modelled as a soft power-law component with photon index $\approx$ 2.9. This latter component contributes 26% of the flux in the 0.3-2 keV band for M83 and 35% for M51. This soft excess may well relate to the contribution of populations of soft sources, most notably recent supernova remnants and, in fact, there is ample observational evidence that such sources are very often prominent in the spiral arms of late-type galaxies, for example IC342 (Kong 2003), M33 (Pietsch et al. 2004; Grimm et al. 2005) and M83 (Soria & Wu 2003). It is also possible that this soft excess may arise due to a low metallicity thermal component, but the quality of the spectra are insufficient to adequately constrain the abundances. Indeed, the fitting of low resolution spectra pertaining to a complex multi-temperature plasma with simple models can often result in the artifical requirement for strongly subsolar abundances (Dahlem et al. 1998; Strickland & Stevens 1998; Weaver et al. 2000). Evidence from studies of the metallicities of several galaxies in our sample (Bresolin et al. 2004; Bresolin 2007; Urbaneja et al. 2005) find the oxygen abundances present to be comparable to solar

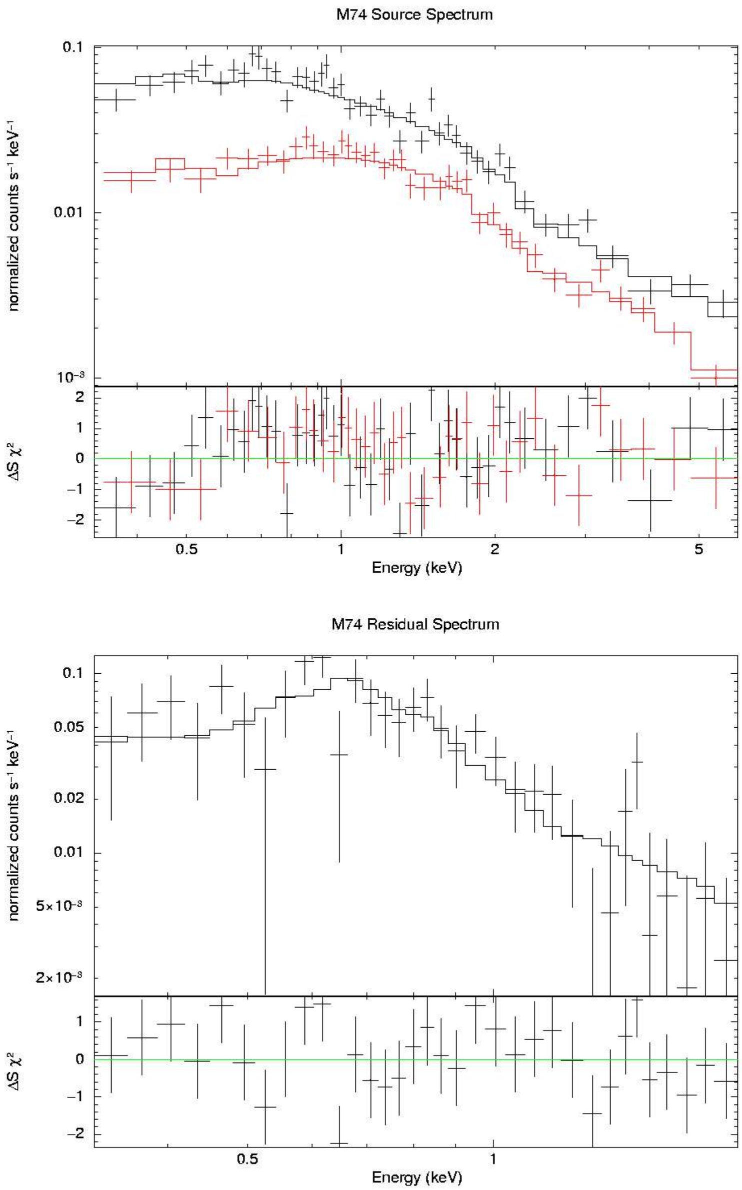

Figure 3.5: The EPIC spectra for M74. *Top panel:* The spectrum of the bright-source region. Black line - pn spectrum. Red line - combined MOS1 + MOS2 spectrum. *Bottom panel:* The spectrum of the residual-galaxy region. The solid line corresponds to the best-fit spectral model (see Table 3.5). The residual spectrum model includes a specified fraction of the best fit source spectrum model (see text). The χ^2 residuals with respect to the best-fitting model are also shown, and all spectra are shown with a minimum of 20 counts per bin.

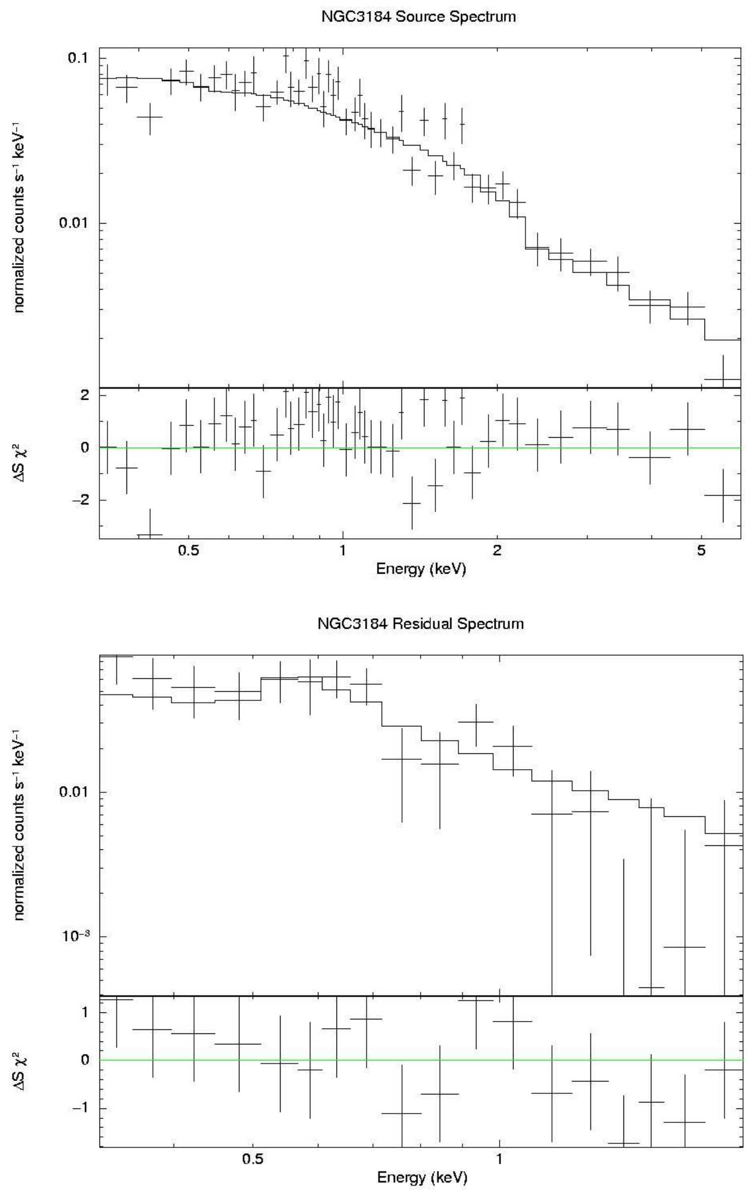

Figure 3.6: The EPIC spectra for NGC3184. *Top panel:* The spectrum of the bright-source region. *Bottom panel:* The spectrum of the residual-galaxy region. The solid line corresponds to the best-fit spectral model (see text). The χ^2 residuals with respect to the best-fitting model are also shown.

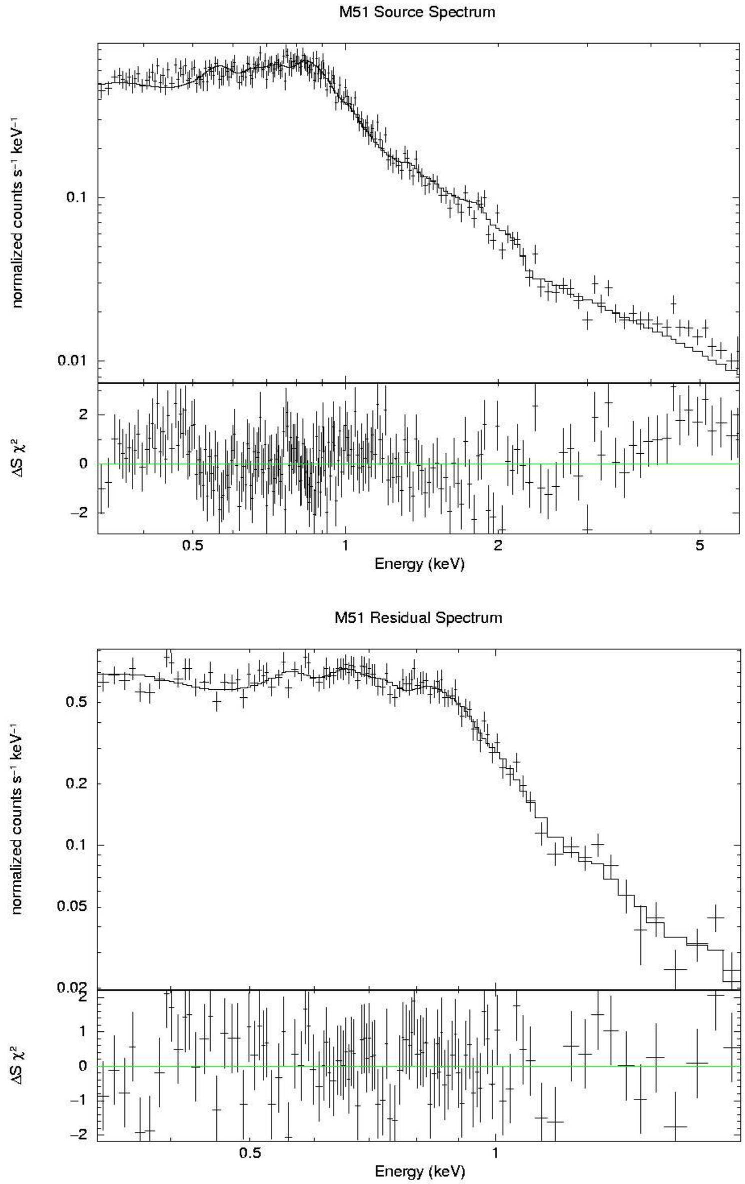

Figure 3.7: The EPIC spectra for M51. *Top panel:* The spectrum of the bright-source region. *Bottom panel:* The spectrum of the residual-galaxy region. The solid line corresponds to the best-fit spectral model (see text). The χ^2 residuals with respect to the best-fitting model are also shown.

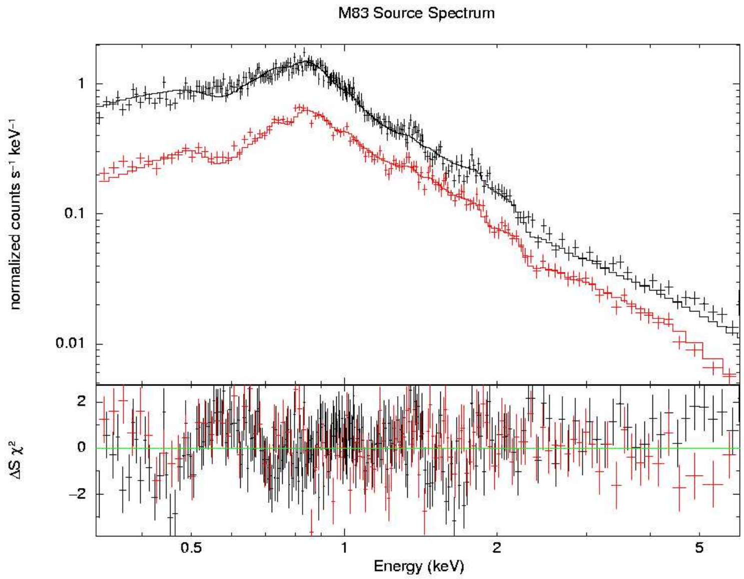

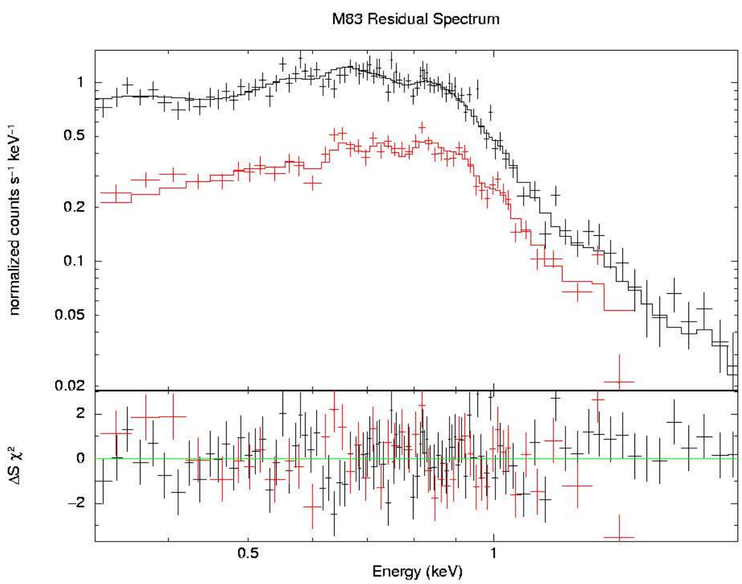

Figure 3.8: The EPIC spectra for M83. *Top panel:* The spectrum of the bright-source region. *Bottom panel:* The spectrum of the residual-galaxy region. The solid line corresponds to the best-fit spectral model (see text). The χ^2 residuals with respect to the best-fitting model are also shown. Black lines represent the pn spectra, red lines the combined MOS spectra.

Table 3.5: Parameters of the best-fitting models to the spectra of the bright-source and residual-galaxy regions.

Galaxy	Region	Power-law Cont. Photon Index Normalization	Cool MEKAL keV Normalization	Hot MEKAL keV Normalization	Goodness of Fit χ^2/dof	Cool:Hot Flux Ratio (0.3–2 keV)
M74	Bright Sources	1.64±0.06 5.62×10^{-5}	-	-	146/150	-
	Residual Galaxy	-	0.26±0.04 3.74×10^{-5}	$[0.65]^a$ $[< 5.5 \times 10^{-6}]^a$	197/202	> 5.4
NGC3184	Bright Sources	1.57±0.10 4.41×10^{-5}	-	0.71±0.13 6.63×10^{-6}	86/78	-
	Residual Galaxy	-	0.20±0.06 1.85×10^{-5}	$[0.65]^a$ $[< 3.5 \times 10^{-6}]^a$	122/105	> 4.1
M51	Bright Sources	1.57±0.05 2.65×10^{-4}	0.19±0.02 1.20×10^{-4}	0.61±0.05 1.48×10^{-4}	389/378	-
	Residual Galaxy	2.90±0.15 1.14×10^{-4}	0.24±0.02 1.63×10^{-4}	0.64±0.04 9.94×10^{-5}	210/260	1.3
M83	Bright Sources	1.86±0.02 5.42×10^{-4}	-	0.61±0.03 2.78×10^{-4}	796/679	-
	Residual Galaxy	2.92±0.15 1.12×10^{-4}	0.24±0.02 2.32×10^{-4}	0.64±0.03 1.19×10^{-4}	404/356	1.5

[a] - Upper bound on the normalization of a 0.65-keV thermal component (95% confidence interval).

Table 3.6: Physical properties of the diffuse gas present in each galaxy.

Galaxy	Radius[a] kpc	Component (keV)	Electron Density $10^{-3}\eta^{-1/2}$ cm^{-3}	Thermal Energy $10^{55}\eta^{1/2}$erg	Cooling Timescale $10^{8}\eta^{1/2}$ yr
M74	10.0	0.2	3.1	2.5	6.6
NGC3184	10.0	0.2	2.1	1.9	4.3
M51	7.5	0.2	6.7	2.4	1.9
		0.65	5.2	5.5	8.3
M83	6.5	0.2	4.9	2.5	4.2
		0.65	3.1	3.6	9.5

[a] - Assumed radius of a putative shallow halo component (see text)

abundances. Indeed in M83 (Dufour et al. 1980) the oxygen abundance ranges from 2-10 times solar. It appears therefore that thermal fits with subsolar abundances are not consistent with observations of these systems. After applying an appropriate area-correction factor, the luminosities derived from the spectral data were broadly consistent with those derived from the imaging analysis (see Table 3.4).

There are two points pertinent to the above spectral analysis. The first is that the spectral modelling did not require the inclusion of any absorption over and above the foreground Galactic N_H which was included as a fixed component in all the models. The implication is that any absorption intrinsic to the host galaxy must be relatively low, commensurate with the fact that we are studying systems which have a near face-on aspect. The second point is that there was no strong evidence in the residual galaxy spectra for a “hard-excess” component attributable to an unresolved population of relatively hard discrete sources. This confirms the conclusions in §3.4.1, namely that relatively luminous binaries (albeit below the applied luminosity threshold) do not provide a substantial contribution to the residual-galaxy emission. In fact the lack of clear evidence for hard emission in the spectra of the residual galaxy regions (and also in the corresponding hard-band images) suggests that the estimates in §3.4.1 of the potential contribution of relatively luminous discrete sources might be best considered as upper-limit values.

For each of the galaxies in the sample, we have measured the relative contribution of the 0.2 keV and 0.65 keV MEKAL components to the X-ray flux measured in the 0.3–2 keV band. The results are summarised in Table 3.5, where we include the upper limits derived for a fixed 0.65-keV component in the case of M74 and NGC 3184. For comparison, the corresponding flux ratio pertaining to the cool and hot MEKAL components in M101 (from the spectral fitting results in W07) is ≈ 3.8.

3.5.3 Physical properties of the diffuse gas

If we assume that all of the emission attributed to thermal components originates in truly diffuse plasma, then it is possible to infer some physical properties of the medium on the basis of a particular geometrical configuration. Here we assume that the thermal plasma is contained within a cylindrical region extending from the centre of the galaxy out to 75% of the D_{25} radius with a half-width perpendicular to the plane of 0.5 kpc, representing a shallow halo. Using this volume, we can infer the mean electron density n_e through the derived emission measure $\eta n_e^2 V$ (where η is the 'filling factor' - the fraction of the total volume V which is occupied by the emitting gas). Using the normalisation of the MEKAL components in our spectral fits (which we denote K), the electron density is given by:

$$n_e = (\frac{4\pi D^2 K}{10^{-14} V})^{1/2} \eta^{-1/2} \tag{3.1}$$

where n_e is the electron density (in cm^{-3}), D is the distance to the galaxy (in m) and V is the volume the gas is contained in (in m^3). The derived electron density combined with the volume and temperature (kT) then leads to an estimate of the thermal energy contained within the gaseous component:

$$E_t = 3 n_e kTV \mathrm{erg} \tag{3.2}$$

By dividing this thermal energy by the observed X-ray luminosity, an estimate of the cooling timescale of the gas can be derived. Based on the measurements from the spectral fitting, we derive the results summarised in Table 3.6. In the cases of M51 and M83, where the balance between the cool and hot thermal components is most strongly weighted towards the hot component, we find that the thermal energy contained in the hotter component is significantly greater than that in the cooler component and that these two components are not in pressure balance. Our spectral modelling of the residual emission in NGC3184 and M74, although not requiring a 0.65 keV spectral component, does not exclude the presence of such a component in rough pressure balance with the cooler plasma, consistent with the situation pertaining in M101 (W07). The cooling of these plasmas is dominated by line emission with radiative timescales in the range $2 - 10 \times 10^{8}\eta^{1/2}$ yr (Table 3.6).

Of course, as noted previously, a more likely scenario is that the bulk of the observed soft emission originates in the combination of diffuse emission closely associated with star-formation in the galactic disk and the integrated emission of the populations of soft sources within the disk.

3.6 The connection between soft X-ray emission and star-formation

As noted earlier, the general similarity of soft X-ray and FUV images establishes a close linkage between the X-ray emission and recent star-formation in these late-type systems. This connection has previously been demonstrated in many individual galaxies and also in samples of objects; for example Tyler et al. (2004) find a very strong correlation between X-ray emission and both Hα and mid-infrared emission in a set of spiral galaxies observed with *Chandra*. In our early study of M101 (W07), we further investigated how the overall point-to-point correlation varies when one contrasts the soft X-ray surface brightness with that measured in different wavebands extending from the FUV through to optical V band. The fact that the best match was between the soft X-ray and U band images was interpreted in terms of two spatial components, namely a clumpy thin-disk component which serves as a tracer of the spiral arms plus a more extended component, possibly located in the lower-halo with a larger filling factor, which produces the central concentration of the soft X-ray emission (W07). However, in the present study we focus on the relationship between the residual galaxy X-ray emission and the corresponding FUV emission in terms of their radial-averaged spatial distribution.

Using the masked pn+MOS soft band images (such as in Fig. 3.4), we have derived the radial profiles of the soft X-ray emission for all six galaxies in our sample. The results are shown in Fig. 3.9 (upper panels). These X-ray radial profiles are based on the signal extracted from *circular* annuli centred on the galactic nucleus, with suitable normalization to allow for the regions excluded by the spatial masking. Since we wish to compare the X-ray radial distributions with published FUV and star-formation profiles obtained using elliptical annuli (matched to the modest inclinations of these galaxies), we have stretched the scale of the X-ray radial axis by a factor of typically 5–10%, so as to account for the (marginally) different radial gradients obtained if one uses circular as opposed to slightly elliptical annuli.

Figure 3.9 also shows the corresponding FUV radial brightness distributions taken from the tabulations in Muñoz-Mateos et al. (2007) (Table 2 in their paper) except in the case of NGC 3184 where, since *GALEX* FUV data are not available, we use *XMM-Newton* Optical Monitor UVW1 (≈ 2680 Å) measurements (without any internal extinction correction). This waveband was chosen since it is the UV filter with the highest sensitivity, making comparison of the morphology of the extended emission easier. These *GALEX* FUV data have been corrected for both foreground and internal extinction as discussed in Muñoz-Mateos et al. (2007).

Visual comparison of the soft X-ray and FUV profiles suggest that radial fall-off seen in the soft X-ray regime is either very comparable to that seen in the FUV (*e.g.* NGC 3184 and M83) or somewhat steeper (*e.g.* NGC 300, M74, M51 and M101). We further use the results of Muñoz-Mateos et al. (2007) to compare our current soft X-ray measurements (after applying appropriate scaling factors to convert the X-ray measurements into luminosity per unit disk area) with the inferred radial dependence of the SFR density (*i.e.* SFR per unit disk area). The results are also shown in Fig. 3.9 (middle panels). We find that in the inner disks of our sample of late-type galaxies, the soft X-ray luminosity generated per unit SFR (hereafter the X-ray/SFR ratio) ranges from 2.5×10^{38} erg s^{-1} (M$_\odot$ yr^{-1})$^{-1}$ in the case of NGC 300 up to 4×10^{38} erg s^{-1} (M$_\odot$ yr^{-1}) for M74 and finally up to $\sim 10^{39}$ erg s^{-1} (M$_\odot$ yr^{-1})$^{-1}$ for M51, M83 and M101. Note that these measurements refer to the soft-band 0.3–1.0 keV luminosity *after excluding* the contribution of the most luminous point sources. There is also the suggestion that the X-ray/SFR ratio declines with galactocentric radius, at least in the case of NGC 300 and M51.

Whereas some correction has been applied to the FUV data to allow for the extinction intrinsic to the host galaxy, we have not applied a similar correction to the soft X-ray data. Earlier we established that based on the spectral fitting, there was no clear evidence for any soft X-ray absorption intrinsic to the host galaxies. Any intrinsic soft X-ray extinction would be most pronounced in the inner galaxy regions potentially giving rise to a central down-turn in the soft X-ray radial distributions - but again there is no compelling evidence for such an effect. It is possible however to predict the level of extinction expected to be observed in each galaxy from that observed in the FUV band. Using the FUV extinction estimates employed by Muñoz-Mateos et al. (2007), we convert this to the soft X-ray absorption using the scaling

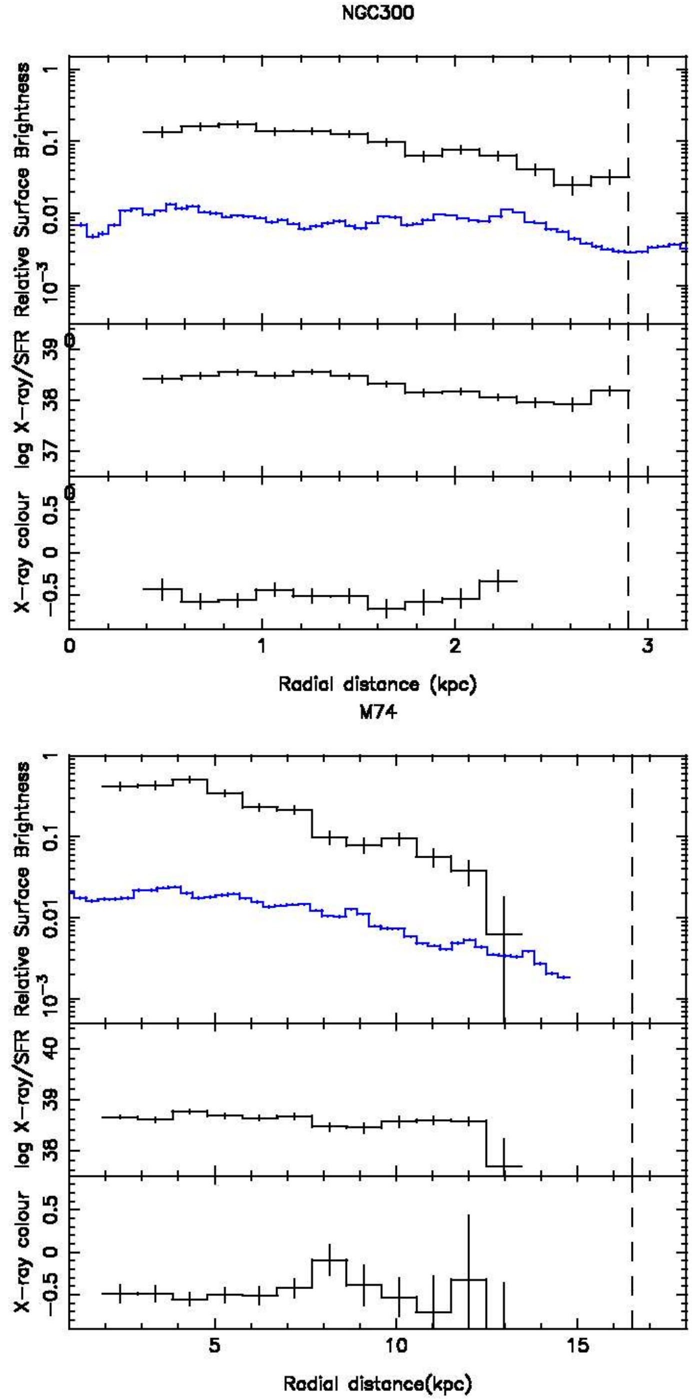

Figure 3.9: A comparison of various radial dependencies for each of the galaxies in the full sample. In these plots the x-axis refers to the major-axis radius scaled to kpc using the assumed distances quoted in Table 3.1. The vertical dashed line represents the extent of the X-ray extraction region scaled to kpc. For each galaxy, the following information is provided: *Top panel:* The soft X-ray surface brightness versus radius (upper curve). The radial profile of the FUV emission after correction for internal extinction - taken from Muñoz-Mateos et al. (2007) (lower curve). *Middle panel:* The ratio of the soft X-ray luminosity in $\mathrm{erg\,s^{-1}\,pc^{-2}}$ (0.3-1 keV) to the local SFR in units of $\mathrm{M_{\odot}\,yr^{-1}\,pc^{-2}}$. *Bottom panel:* Variation in X-ray spectral hardness, (H-S)/(H+S), versus radius, where H refers to the 0.8–1.2 keV band and S to the 0.3–0.8 keV band. *Top frame:* Radial profile of NGC300. *Bottom frame:* Radial profile of M74.

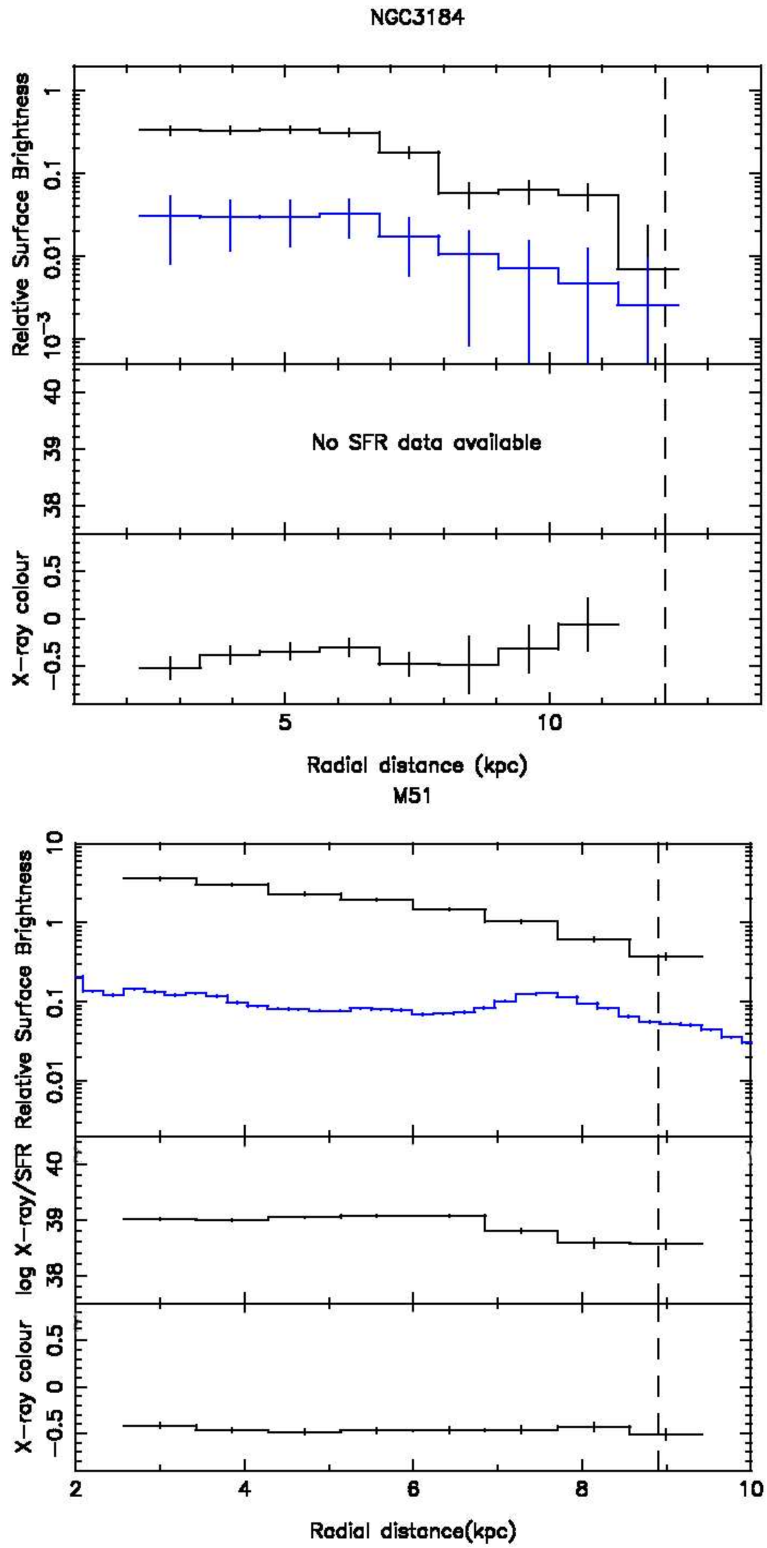

Figure 3.10: As for Fig. 3.9. *Top frame:* Radial profile of NGC3184. *Bottom frame:* Radial profile of M51.

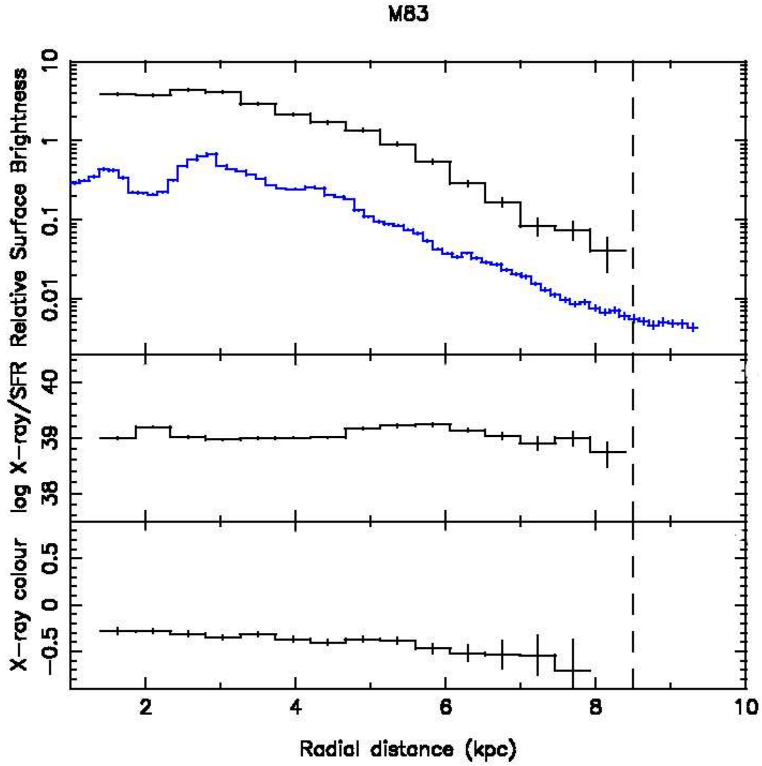

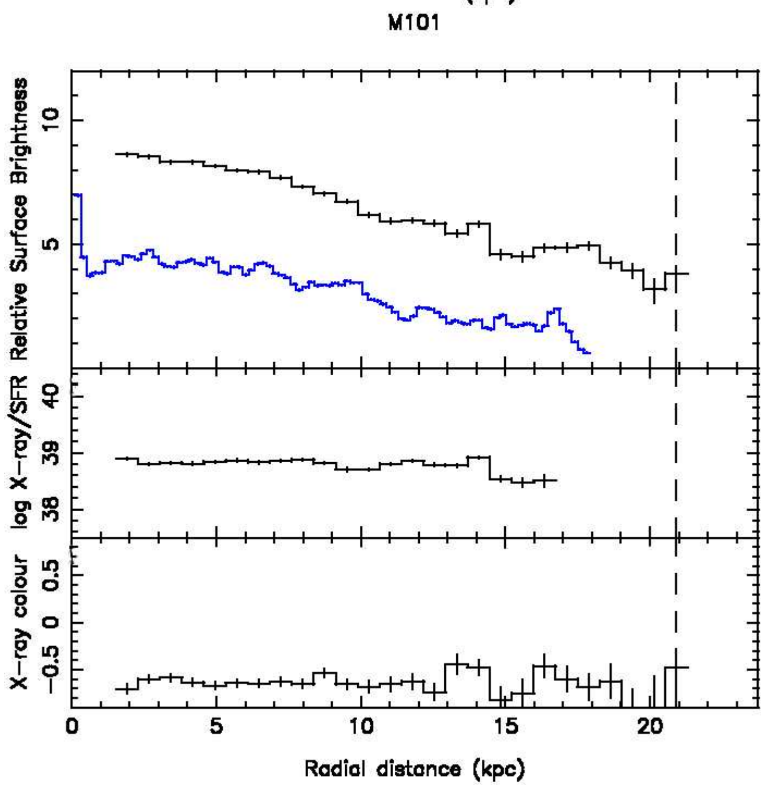

Figure 3.11: As for Fig. 3.9. *Top frame:* Radial profile of M83. *Bottom frame:* Radial profile of M101.

A(FUV)/N_H = 1.6×10^{-21} mag cm^{-2}, which assumes a Galactic dust-to-gas ratio and extinction law with $R_V = 3.1$ (Bohlin et al. 1978; Cardelli et al. 1989). This leads to estimates of the intrinsic X-ray absorption in the inner disk regions in the range $N_H = 5 - 12 \times 10^{20}$ cm^{-2} across the set of galaxies. Since these values are too high to be consistent with spectral fitting we can conclude either that the assumptions underlying the FUV to X-ray extinction scaling are not valid or, as seems likely, the FUV sources are more strongly embedded in obscuring material than the soft X-ray emission. As a final check we have looked for spectral trends versus radius by repeating the imaging analysis for two soft X-ray sub-bands, namely 0.3–0.8 keV and 0.8–1.2 keV. We then determine a spectral hardness ratio as (H-S)/(H+S), where H refers to the 0.8–1.2 keV band and S to the 0.3–0.8 keV band. Figure 3.9 (lower panels) shows the measured variations in spectral hardness versus radius. These curves show no marked spectral variations towards the inner galaxy regions, thus confirming that intrinsic absorption does not strongly influence the soft X-ray measurements.

The demarkation of the above sub-bands at 0.8 keV corresponds roughly to the position in the M51 and M83 spectra at which the cool and hot thermal components contribute equally. It follows that the spectral hardness profiles in Fig. 3.9 track the ratio of these two thermal components as a function of galactocentric radius. If we consider the three sources with best signal-to-noise, we find no variation in spectral hardness versus radius in M101, a hint of spectral softening versus radius in M83 and the hint of an opposite trend in M51.

3.7 Discussion

A major objective of our investigation is to intercompare the X-ray properties and other characteristics of the extended disks of the six late-type galaxies which comprise our sample. To that end we have summarised some of the results from the current analysis in Table 3.7. In brief this table provides the following information. We first define the extent of the disk region considered in X-rays. For this intercomparison we have chosen to exclude a central $1'$ radius region in both M51 and M83, so as to avoid the complications associated with the AGN and/or the nuclear starburst. We have next calculated the total SFR within the specified disk region by integrating under the exponential fits to the starburst density radial profiles reported by Muñoz-Mateos et al. (2007). We next report the luminosity associated with the disk by taking our soft band residual luminosity estimates and then correcting both

Table 3.7: Derived properties of the galactic disks.

Galaxy	Disk Radial Extent		SFR	L_X(0.3–2 keV)[a]	Cool:Hot
	Inner (kpc)	Outer (kpc)	$M_\odot$ yr^{-1}	10^{39} erg s^{-1}	Flux Ratio
NGC300	0	2.9	0.19	0.11	-
M74	0	16.7	5.2	1.2	> 5.4
NGC3184	0	12.2	-	3.4	> 4.1
M51	2.4	8.9	7.5	6.8	1.3
M83	1.3	8.5	3.5	3.4	1.5
M101	0	20.9	8.1	4.3	3.8

[a] - Luminosity after excluding sources with $L_X > 10^{37}$ erg s^{-1} (0.3–6 keV)

to a common source exclusion threshold of $L_X > 10^{37}$ erg s^{-1} (0.3–6 keV) (using essentially the same methodology as applied in §3.4.2) and to a broader 0.3–2 keV band-pass (using the spectral models for the residual emission regions discussed earlier[3]). These corrections were generally less than 20% except for NGC300, where the luminosity increased by a factor of 2.2 as a result of a significant additional contribution from discrete sources. Finally, we also note the relative strengths of the cool (0.2-keV) and hot (0.65-keV) thermal components in terms of the ratio of their fluxes in the 0.3–2 keV (band), as inferred from the spectral modelling (§3.5.2).

The results summarised in Table 3.7 establish that averaged over the defined disk regions, the X-ray/SFR ratio varies from a maximum of $\approx 10^{39}$ erg s^{-1} ($M_\odot$ yr^{-1})$^{-1}$ in the case of M51 and M83 down to $\approx 2 \times 10^{38}$ erg s^{-1} ($M_\odot$ yr^{-1})$^{-1}$ in M74. However, these disk-average values mask a trend, which is evident in Fig. 3.12, where we have plotted the X-ray/SFR ratio versus the local SFR density. Above a local SFR density of $\sim 3 \times 10^{-8}$ $M_\odot$ yr^{-1} pc^{-2} (corresponding to the inner disks of M51 and M83), the X-ray/SFR ratio is consistent with an upper bound value of $1 - 1.5 \times 10^{39}$ erg s^{-1}

[3]In the case of NGC300 we assume a single component (0.2-keV) MEKAL spectrum and for M101 we use the spectral model reported in W07.

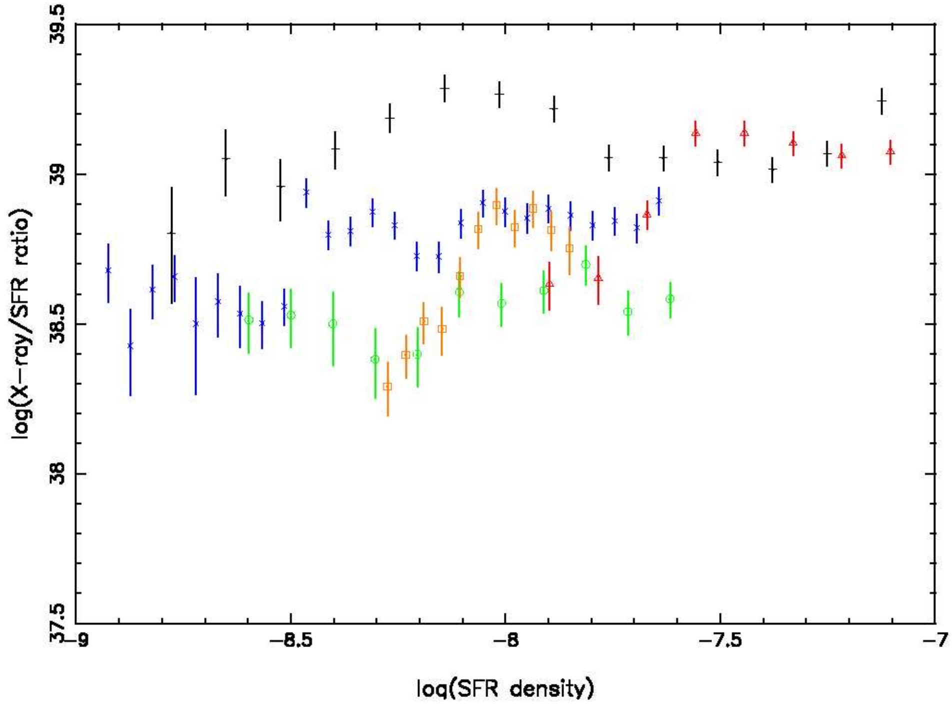

Figure 3.12: The ratio of the soft X-ray luminosity in units of $\mathrm{erg\,s^{-1}}$ pc^{-2} (0.3–2 keV) to the local SFR density in units of $\mathrm{M_\odot}$ yr^{-1} pc^{-2} versus the local SFR density. The data points correspond to NGC300 (orange squares), M74 (green circles), M51 (red triangles), M83 (black points) and M101 (blue crosses).

($\mathrm{M_\odot}$ yr^{-1})$^{-1}$. However, below a local SFR density of $\sim 3\times10^{-8}$ $\mathrm{M_\odot}$ yr^{-1} pc^{-2}, there is significant scatter in the ratio, spanning a range up to a factor 5 below the maximum. On the one hand some of this scatter appears to be due to the fact that all five galaxies show evidence for a fall-off in the X-ray/SFR ratio in their outer disks. On the other hand systematic errors in both the X-ray and FUV measurements will grow in importance as one tracks a signal of rapidly decreasing surface brightness against an essentially constant background. Nevertheless, these results do suggest that the efficiency of X-ray production may be sensitive to the local level of star-formation activity in the disk.

In a recent study, Mas-Hesse et al. (2008) (hereafter MH08) have investigated the temporal evolution of both the soft X-ray and far infrared (FIR) luminosity following a burst of star formation. The starting point of their analysis is the adoption of a stellar population synthesis model which follows the evolution of a cluster of massive stars formed either at the same time (which MH08 refer to as an instantaneous burst, IB) or at a constant rate over a period of several tens of Myr (an extended burst, EB). In either scenario, diffuse soft X-ray emission is produced through the heating of bubbles within the interstellar medium to temperatures of $\sim 10^6 - 10^7$ K as a result of the mechanical energy input from the winds of massive stars created in the starburst or the eventual destruction of such stars in supernovae. Their model also includes the soft X-rays emitted by individual SNR during the adiabatic expansion phase of their evolution, but excludes any contribution from the stellar atmospheres (which in any case would be extremely small) or accreting high-mass X-ray binaries created in the region. MH08 (see their Figure 1) find that the soft X-ray luminosity increases rapidly during the first few Myr following the onset of starburst activity, largely through the input power of the stellar winds of the most massive stars. After the first 3 Myr, the most massive stars produce supernovae and thereafter it is the mechanical energy of such explosions which dominates the energy budget. In the IB models the soft X-ray luminosity peaks at ~ 3 Myr, whereas in the EB models it continues to rise, albeit more gradually, until eventually an equilibrium is established between the formation and destruction of stars (after typically ~ 40 Myr for solar metallicities).

In comparing our present measurements with the predictions of MH08 it is important to bear in mind that we have used SFR estimates based on FUV measurements (Muñoz-Mateos et al. 2007), which in turn rely on the UV-to-SFR calibration suggested by Kennicutt (1998). As noted by MH08, the Kennicutt (1998) calibration assumes star formation over a wide 0.1–100 $\mathrm{M_\odot}$ mass range, whereas the SFR values they quote are for a more restricted 2–120 $\mathrm{M_\odot}$ range (which has a more direct bearing on the resulting soft X-ray and FIR luminosity). Assuming a Salpeter initial mass function, one obtains the scaling SFR(2-120 $\mathrm{M_\odot}$)/ SFR(0.1-100 $\mathrm{M_\odot}$) $= 0.293$, implying that our estimates of the X-ray/SFR ratio should be increased by a factor 3.4 when making a comparison with the MH08 predictions. Our upper-bound estimate, after applying the above scaling, becomes $\sim 5 \times 10^{39}\ \mathrm{erg\ s^{-1}}\ (\mathrm{M_\odot\ yr^{-1}})^{-1}$, which correponds to the X-ray/SFR ratio predicted some 10 Myr after the onset of an extended burst of star-formation, assuming a 1% efficiency in the conversion of mechanical energy into X-ray emission. Although it can be argued that star formation in the disks of late-type spiral galaxies generally proceeds over long-periods of time, the underlying activity pattern is presumably one of localised bursts of star formation, so a match with "young" extended bursts is perhaps not unreasonable. Of course, in matching the observations to the predictions, the efficiency of X-ray production and the duration of the EB episode are inversely linked, for example the above X-ray/SFR ratio is also reached after 30 Myr in the EB scenario, provided the energy conversion efficiency is scaled down to just 0.2%. Clearly a more detailed study, taking into account additional information relating to the current star formation rate and the star formation history relevant to each galaxy disk, might well pin down these parameters - but such an analysis is beyond the scope of the current study.

A number of recent studies have investigated whether the integrated soft (nominally 0.5-2 keV) or hard (2-10 keV) X-ray luminosities measured in galaxies not dominated by a central AGN might serve as a proxy for the underlying galaxy-wide SFR (*e.g.* Grimm et al. 2003; Ranalli et al. 2003; Gilfanov et al. 2004), which might then be applicable to more distant objects (*e.g.* Rosa-González et al. 2007). If we consider the Ranalli et al. (2003) calibration of the SFR in terms of the integrated soft X-ray luminosity (their equation 14), apply the corrections noted by MH08 and also scale the X-ray luminosity from a 0.5–2 keV bandpass to the 0.3–2 keV bandpass (which increases the luminosity by a factor of $1.1 - 1.5$ depending on the spectral assumption), we obtain an X-ray/SFR ratio in the range $10{-}14{\times}10^{39}$ erg s^{-1} (M$_{\odot}$ yr^{-1})$^{-1}$ which is factor $2 - 2.8$ higher than the (upper-bound) value derived from the current analysis. The difference is, of course, due to the fact that Ranalli et al. (2003) use the integrated soft X-ray luminosity of the entire galaxy, which includes a very substantial contribution from the bright discrete source population. In fact the ratio of the total galaxy luminosity to the residual galaxy luminosity over the 0.3-2 keV band for our current set of galaxies (see Table 3.4) is typically in the range $2 - 2.5$, consistent with this picture. It follows that when using the Ranalli et al. (2003) calibration to convert soft X-ray measurements to SFR rate estimates, an implicit assumption is that *both* the rate of production of X-ray binaries following a starburst and the subsequent balance between point source and diffuse luminosity is comparable to that pertaining in local galaxies.

As discussed above there is evidence that the X-ray/SFR ratio falls as the local SFR density declines, implying that the interstellar environment influences either the starburst and/or the efficiency with which its energy is reprocessed into the X-rays. Factors which may potentially be relevant include the local gas density (relevant to the conversion of mechanical energy into heat via shocks) and the local metallicity (which may, for example, influence the evolution timescales of massive stars, their stellar wind properties and the emissivity of the X-ray plasma heated by the starburst). It is also notable that the galaxies in our current sample with the highest X-ray/SFR ratios are those with the strongest weighting towards hot plasma (as measured by the cool:hot flux ratios in Table 3.7). In this context it would seem entirely plausible that X-ray production efficiency and “mean” plasma temperature are coupled quantities. Although the current data are too restricted to merit further consideration of these issues, such effects may well be relevant when attempting to fine tune the calibration of the soft X-ray luminosity versus SFR relation for specific applications in which the bright source component is spatially resolvable.

Star formation in the disks of spiral galaxies is thought to be triggered by the passage of a spiral density wave through the ISM. The resultant massive star formation results in copious FUV emission which in turn is rapidly reprocessed into Hα and FIR emission. As discussed above, the mechanical energy input from stellar winds and supernovae eventually gives rise to X-ray emission. This would seem to give an immediate explanation of the strong correlation observed between the infrared, optical and UV star-formation tracers and the soft X-ray emission seen in spiral galaxies (*e.g.,* Read & Pietsch 2001; Kuntz et al. 2003; Tyler et al. 2004, W07). However, the underlying timescales are not identical. UV and Hα emission will be produced on a timescale commensurate with the lifetime of the most massive stars ($\sim 3 \times 10^6$ years), whilst according to model predictions (Leitherer & Heckman 1995; Cerviño et al. 2002; MH08), it takes approximately ten times longer to maximise the diffuse X-ray emission. Given the delay between the peak in UV/Hα emission and the X-ray heating, one might predict a spatial offset between the diffuse X-ray emission and the other spiral tracers more closely tied to the passage of the spiral density wave. For example, W07 argue that in the case of M101 one might predict a rotational lag of $\approx 24^\circ$ at a galactocentric radius of $r \approx 7.5$ kpc (given a rotational velocity $v_{rot} \approx 200\ \ \mathrm{km\ s^{-1}}$ and assuming that the spiral pattern corotates with the disk material at $r \approx 15$ kpc). However, lags of this magnitude are not generally evident in the X-ray morphology of late-type galaxies (Tyler et al. 2004).

Assuming a gas filling factor $\eta \sim 1$ and a spatial extent perpendicular to the plane of the galaxy of 0.5 kpc, we earlier derived radiative cooling timescales in the range $2 - 10 \times 10^8$yr (Table 3.6). These estimates are comparable to the galaxy rotational periods in the region sampled by the current X-ray measurements and are clearly inconsistent with the presence of narrow X-ray spiral arm features. Matching the radiative timescales to the "young" extended burst scenario discussed earlier would require $\eta <<1$, consistent with a clumpy thin-disk distribution for the X-ray emitting plasma most closely associated with the spiral arms. In practice, however, the observed X-ray emission will encompass a complex web of diffuse features extending over a range of spatial scales including superbubbles and, in the most active regions, outflows into the lower galactic halo (*e.g.* Strickland et al. 2004a; Strickland et al. 2004b). Where there is no confinement by chimneys or similar structures in the ISM, energy losses arising from adiabatic expansion of the hot gas in the disk may also help localise the spiral arm component (W07). Relatively luminous discrete sources including young SNRs, some perhaps linked to disk population stars in interarm regions, together with aggregations of less luminous objects such as CVs and active binaries, add further to the mix.

3.8 Conclusions

We have used *XMM-Newton* observations in a study of the extended extranuclear disks of six nearby face-on spiral galaxies. Using a novel spatial masking technique to minimise the impact of the brightest discrete sources, we have investigated both the spatial morphology and the spectral properties of the residual soft X-ray emission emanating from the disk regions. The strong correlation found between soft X-ray and FUV images in terms of the tracing of specific spiral features and the overall radial extent of the emission unambiguously establishes a close link between the soft X-ray emission and recent star formation.

More detailed comparison of the radial profiles of soft X-ray and FUV surface brightness distributions establishes an X-ray/SFR ratio of $\sim 5 \times 10^{39}$ erg s^{-1} (M$_{\odot}$ yr^{-1})$^{-1}$ (referred to the 0.3–2 keV band and where the SFR applies to stars in the mass range 2–120 M$_{\odot}$) for the inner disks of M51 and M83. This is roughly a factor 2.5 below the soft X-ray to SFR calibration report by Ranalli et al. (2003), consistent with the fact that our estimate excludes the contribution of discrete sources with $L_X > 10^{37}$ erg s^{-1} (0.3–6 keV). Our measured X-ray/SFR ratio matches that predicted some 10 Myr after the onset of an extended burst of star formation in the models of MH08, when the efficiency of the conversion of mechanical energy input to X-rays is set at $\sim 1\%$. Our observations suggest a fall-off in the X-ray/SFR ratio as the local SFR density declines, implying that the interstellar environment influences either the starburst and/or the efficiency with which its energy is reprocessed into the X-rays.

With the bright sources excluded, the spectra of the residual galaxy regions are, in the main, well matched by a two-temperature thermal plasma model. The characteristic temperatures of ≈ 0.2 and ≈ 0.65 keV are in line with published results for other spiral and starburst galaxies. The relative strengths of these two components varies across the sample, with the galaxies having the highest X-ray/SFR ratio characterised by a higher “mean” temperature. The physical properties of the gas found in the disk are shown to be consistent with a clumpy thin-disk distribution presumably composed of diffuse structures such as superbubbles together with individual SNRs and other source aggregations.

Future observations should allow more detailed investigation of a wide range of factors, for example the local gas density and the local metallicity, which might influence the X-ray/SFR ratio measured in late-type galaxy disks.

Chapter 4

Properties of the Bright X-ray Point Source Population

4.1 Introduction

In this chapter, we study the X-ray colours of the bright X-ray point source population in a sample of six nearby face-on spiral galaxies, the same sample for which we studied the diffuse and unresolved emission present in Chapter 3. We use the classifications defined by Prestwich et al. (2003) and Kilgard et al. (2005) to examine the colours of the source population and relate them to the underlying luminosity distribution. We also compare the source positions with UV and X-ray images to identify any differences between the high-luminosity populations associated with different regions of the galactic disks. In §4.2 we describe the methods used to produce our source list. In §4.3 we describe the point source populations identified in each galaxy in turn, whereas in §4.4 we examine the properties of the population as a whole. Finally, we summarise our conclusions in §4.5.

4.2 Methodology

For the six galaxies in our sample, we constructed a point source catalogue from the primary observations of each galaxy. For five of the galaxies (M83, M74, M101, NGC300 and NGC3184), we used the 2XMM catalogue as our basis. The primary observation for M51 was not included in the set of observations used to produce the 2XMM catalogue, so a separate source list constructed in the same way was used. We used a number of criteria to produce a sample of sources suitable for hardness ratio analysis. For a source to be counted in the pn or either MOS camera, it must be detected with a maximum likelihood of 15 in at least one of the five 2XMM energy bands, which corresponds to a 5σ detection in that band. Soft sources are detected with a higher sensitivity by using this filtering criterion, due to the greater effective area of the pn camera at soft energies, but this effect is relatively small (Jenkins et al. 2005). This threshold corresponds to an approximate flux limit of 1×10^{-14} erg cm^{-2} s^{-1} in the 0.2-12 keV band. We are confident that almost all X-ray point sources in the target galaxies brighter than this flux are in the 2XMM catalogue, although we observed in 3.3.2 that a small number of sources have been missed by the automatic source detection procedures. This is primarily due to confusion of the source with prominent extended emission regions. The affected sources are hence not included in this study. The extent of the source is limited to a maximum of $30''$ and more than 80% of the source PSF must lie on the detector. The resulting source list contains the count-rates and errors for each detected point source in five energy bands: 0.2-0.5 keV, 0.5-1.0 keV, 1.0-2.0 keV, 2.0-4.5 keV and 4.5-12.0 keV. For our analysis, bands 1 and 2 are defined as soft (0.2-1.0 keV), band 3 as medium (1-2 keV) and bands 4 and 5 as hard (2-12 keV). In order to be able to compare sources for which there is either no MOS or no pn data, we apply conversion factors for each energy band to translate a MOS camera count-rate into an equivalent pn count-rate. This conversion factor is not strongly dependent on the spectral shape of the source. The weighted mean of the data from all instruments for the source is then used to produce the final count-rates and errors in each band, which are used to calculate the hardness ratios HR1 = (M-S)/(M+S) and HR2 = (H-M)/(H+M). These hardness ratios are similar to those used in previous colour classifications of point sources. In order to classify the nature of the point sources, we have used the HR1 and HR2 classifications developed by Prestwich et al. (2003) and Kilgard et al. (2005) for *Chandra* sources, which were adapted to *XMM-Newton* wavebands by Jenkins et al. (2005). We use slightly different wavebands here, and the range of hardness ratios corresponding to different source types is adjusted to reflect this. These ranges are given in Table 4.1. Fig. 4.1 shows the positions on this colour-colour diagram obtained from a simple power-law fit with a range of absorption.

One aspect of the point source population we are interested in studying is the spatial distribution of different source types across the galactic disks. Using GALEX FUV images of each galaxy smoothed to the same spatial resolution as the X-ray images, we used a surface brightness cut to define "on-arm"

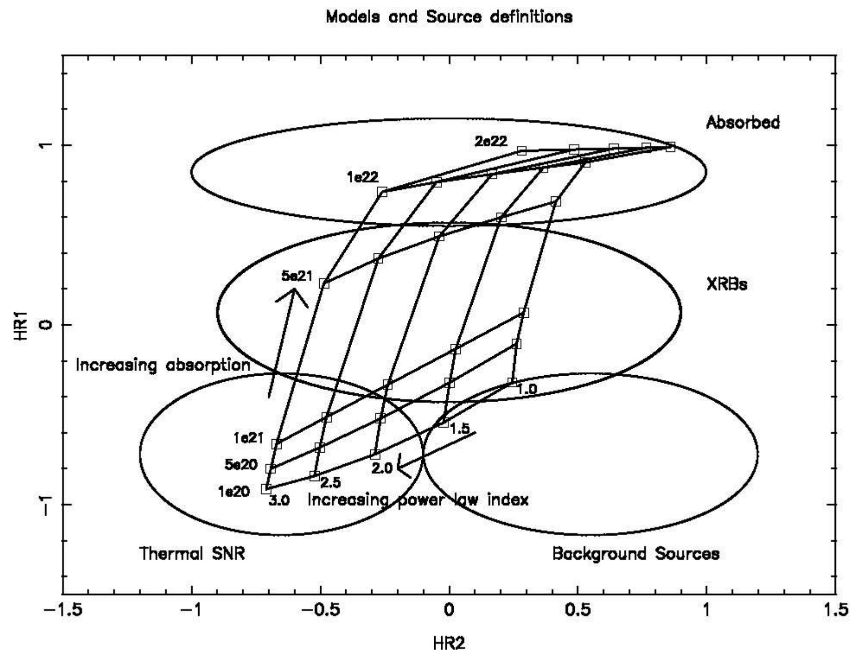

Figure 4.1: The Hardness Ratios predicted for simple power-law models with varying absorption. The ellipses show the boundaries of the colour ranges used for each category. The models show power laws with indices $1, 1.5, 2, 2.5$ and 3 (right to left) with absorption of $10^{20}\ \mathrm{cm}^{-2}$, $5\times10^{20}\ \mathrm{cm}^{-2}$, $10^{21}\ \mathrm{cm}^{-2}$, $5\times10^{21}\ \mathrm{cm}^{-2}$ and $10^{22}\ \mathrm{cm}^{-2}$ (bottom to top).

and “off-arm” regions, and classified each source according to its position. In this way, it is possible to determine any differences between the source population associated with the spiral arms and that associated with the rest of the disk. We are also interested in studying any variation in source colour with luminosity. To achieve this, it was necessary to convert the broad-band count-rates into X-ray luminosities. Using a standard source spectral model of a power-law with $\Gamma = 1.7$ and foreground Galactic absorption, as well as the best-estimate distance to the host galaxy, we converted the count-rate in each band to an unabsorbed luminosity in that band. As all of the galaxies studied are face-on, there was no compelling reason to include extra absorption intrinsic to the host. Finally we summed the luminosity across the energy bands to obtain the broad-band source luminosity, which was then used in the hardness ratio comparison.

Table 4.1: Classification of sources by EPIC pn hardness ratios.

Source type	HR1 range	HR2 range
Supernova remnant	$<$ -0.27	$<$ -0.10
X-ray binary	-0.40 – 0.58	-0.80 – 0.80
Background source	$<$ -0.27	$>$ -0.10
Absorbed source	$>$ 0.58	-1.00 – 1.00

4.3 Point source populations in each galaxy

4.3.1 M101

Of the 114 sources in the 2XMM catalogue within the D_{25} disk of M101, 52 passed the filtering process described in §4.2. The positions of these sources are marked in X-ray and NUV images of M101 in Fig. 4.2. 28 of the sources are defined as "on-arm" and 24 as "off-arm". The lowest luminosity of any source in this sample is $\approx 5 \times 10^{37}$ erg s^{-1}, which restricts the population observed to the higher luminosity end of the LMXB and HMXB populations, as well as some bright SNRs and super-soft sources. As shown in Fig. 4.3, 11 of the sources have colours which put them in the category of SNR candidates, 9 of which are located in the vicinity of the spiral arms. As most bright type II SNRs should be located near regions of recent star formation in the spiral arms, this result indicates that the population of SNR-type sources in the disk is predominantly associated with the young stellar population. Examining the distribution of these sources with luminosity, we find that they span from our lower luminosity limit up to 1.5×10^{39} erg s^{-1}. The lower end of this range is consistent with the sources being SNRs, whereas the higher luminosity sources (with $L_X \approx 10^{39}$ erg s^{-1}) may be soft XRBs or SSSs. Of the remainder of the sources in our sample, 2 are clear background sources, as indicated by their relative prominence in the hard band, and three are highly absorbed. The remaining 36 sources have colours typical of X-ray binaries. The "on-arm" XRB sources are slightly more closely bunched in hardness ratio than those detected "off-arm". We expect the majority of off-arm sources to be LMXBs associated with the galactic disk, with the on-arm X-ray binary population split between HMXB and LMXB sources. The lifetime of the HMXB sources is on the scale of 10^7 yr, a timescale too short to allow them to drift from the spiral arms into the off-arm regions. As the luminosity of the sources increases, the hardness ratio HR1 shows a slight tendency to decrease, indicating a softening of the spectrum. Four sources in the galaxy are detected as candidate ULXs in the broad band (0.3-12 keV), one of which has been reported

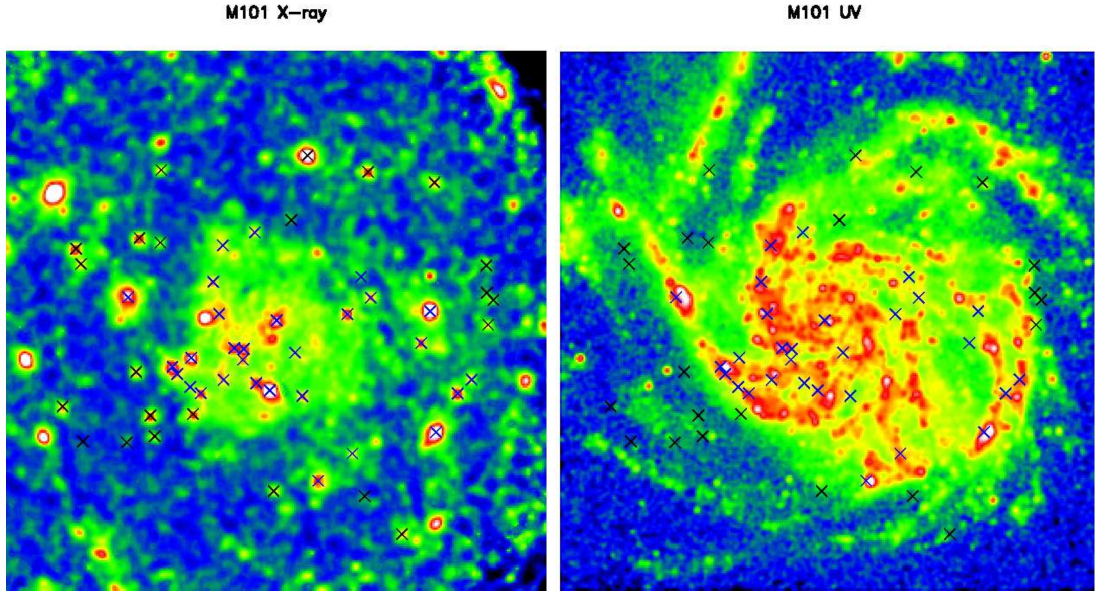

Figure 4.2: The locations of the X-ray point sources identified in the disk of M101. *Left panel:* Adaptively smoothed version of the *XMM-Newton* broad-band (0.3-6 keV) image with the positions of the point sources used in our analysis marked. Blue crosses: sources marked as on-arm. Black crosses: sources marked as off-arm. The amplitude scaling shown is logarithmic. *Right panel: GALEX* FUV image with the positions of the X-ray sources superimposed.

to be coincident with a bright OB star (Kong & di Stefano 2006). Of this ULX population, three are clearly located in the spiral arms in areas with a large quantity of unresolved UV and X-ray emission, whereas the remaining source is located away from areas of unresolved X-ray emission to the north of the galactic disk. The hardness distribution of sources broadly agrees with that derived by Jenkins et al. (2005), which also shows that the disk of M101 is dominated by XRBs.

4.3.2 M83

50 point sources are included in the 2XMM catalogue within the D_{25} disk of M83, 27 of which passed the filtering criteria so as to be included in our sample. The lowest luminosity sources included have $L_X \approx 4 \times 10^{37}$ erg s^{-1} (0.2-12 keV). 15 of these sources are detected in "on-arm" regions of the galaxy, with the remaining 12 in "off-arm" regions (See Fig. 4.4). From the hardness ratios in Fig. 4.5, one source is identified as a possible SNR candidate, with a broad-band luminosity of 5×10^{37} erg s^{-1}. The only other source with similar spectral characteristics is the nuclear source, measured with $L_X \approx 8 \times 10^{39}$ erg s^{-1}. There is one faint source coincident with the spiral arms whose

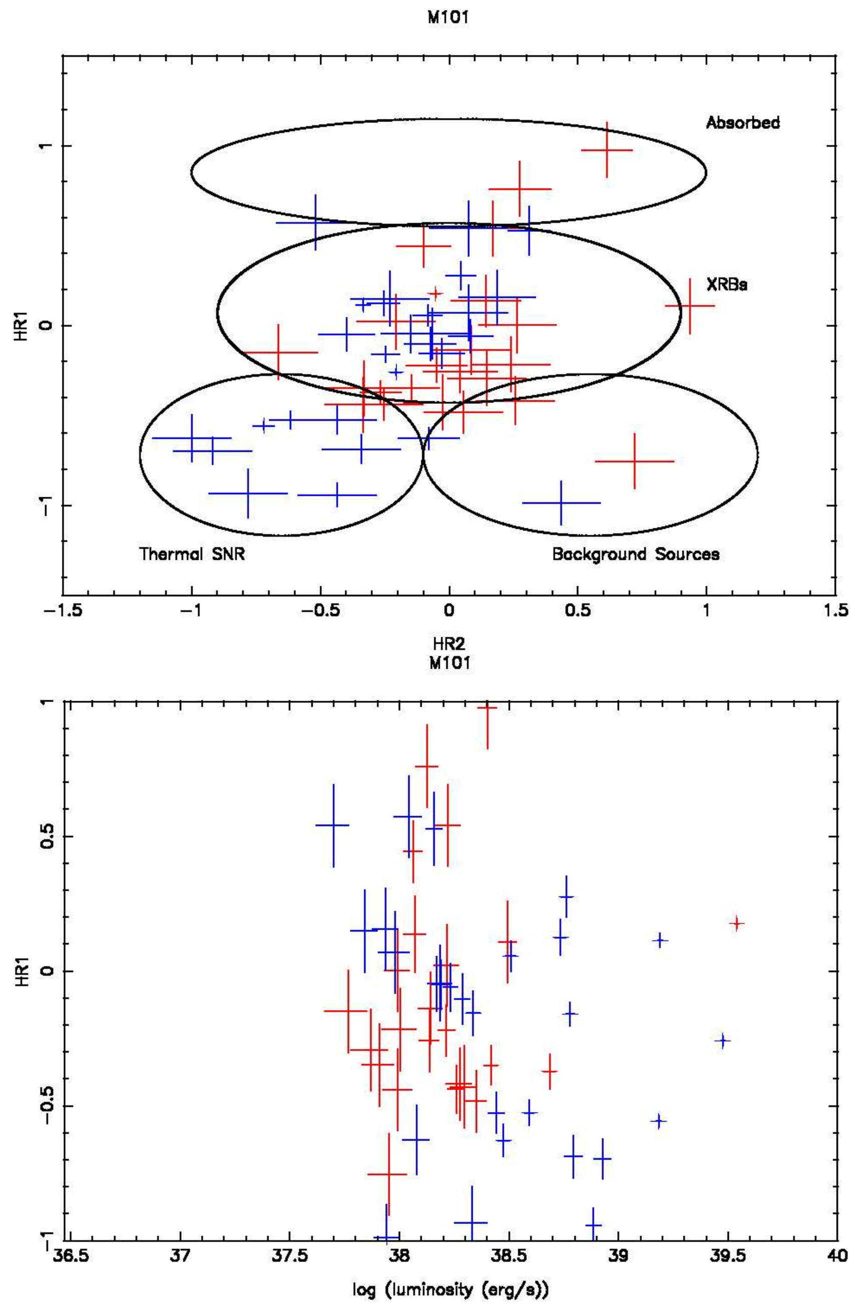

Figure 4.3: *Top panel:* Hardness ratios of the point sources in the disk of M101. HR1 = (M-S)/(M+S) and HR2 = (H-M)/(H+M) where S = 0.2-1 keV count-rate, M = 1-2 keV count-rate and H = 2-12 keV count-rate. These are used for all galaxies in our sample. Marked regions refer to source classifications according to the scheme defined in Kilgard et al. (2005). *Bottom panel:* HR1 for each of the sources compared with the broad-band (0.2-12 keV) luminosity of the source. In this and following plots, the blue crosses refer to sources marked as "on-arm", with the red crosses referring to "off-arm" sources.

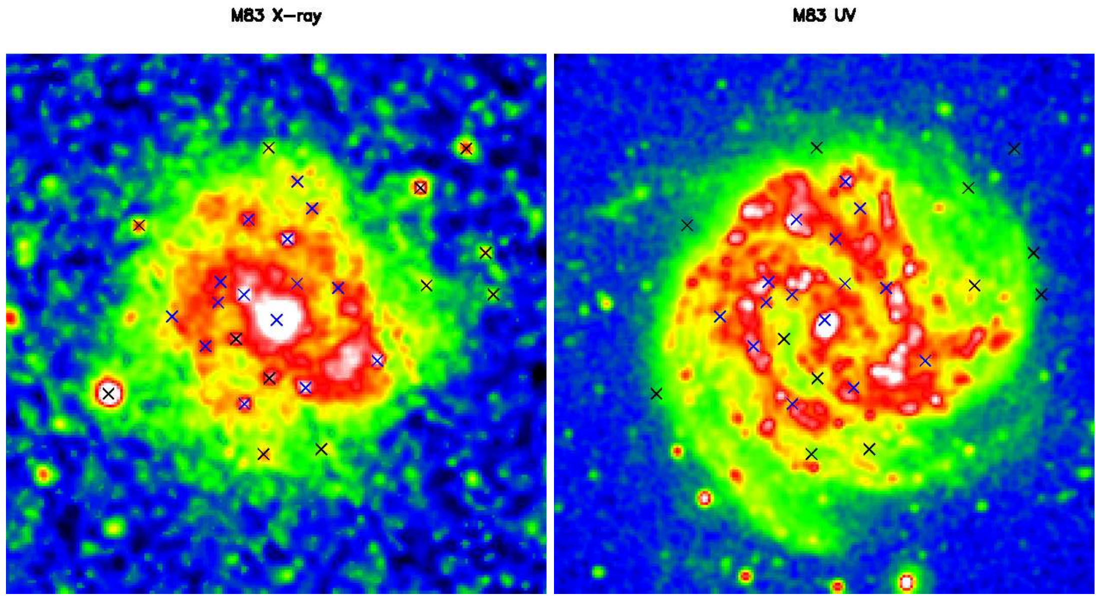

Figure 4.4: The locations of the X-ray point sources identified in the disk of M83. *Left panel:* Adaptively smoothed version of the *XMM-Newton* broad-band (0.3-6 keV) image showing the positions of the point sources used in our analysis. *Right panel: GALEX* FUV image with the positions of the X-ray sources superimposed.

colour profile ((HR2,HR1)=(1,-1)) is consistent with a background AGN, and 3-4 sources which are highly absorbed. The remaining 20 sources are consistent with X-ray binary colours, and are equally split between on-arm and off-arm sources. One of these is a candidate ULX, and is located in the south-eastern disk, significantly separated from the spiral arms. Comparison with a similar analysis of M83 point sources conducted by Kilgard et al. (2005) using *Chandra* data shows a similar colour distribution to ours, albeit for a far larger sample of $\approx$ 100 sources. At fainter luminosities, the population of SNR candidate sources increases significantly, as does the number of background AGN observed.

4.3.3 M51

M51 is the most actively star-forming galaxy of our sample at a distance of 8.4 Mpc. The sourcelist used contains 31 point sources, 20 of which passed the filtering criteria. 13 of these are coincident with the spiral arms, with 7 sources detected elsewhere in the disk (Fig. 4.6). As the overall surface brightness level of X-ray emission is so high in the disk, the corresponding minimum luminosity required for a high confidence interval detection is $L_X \approx 10^{38}$ erg s^{-1}. The hardness ratio plot (Fig. 4.7) shows six bright sources with colours consistent with SNRs. However, as five of these are ULX candidates with

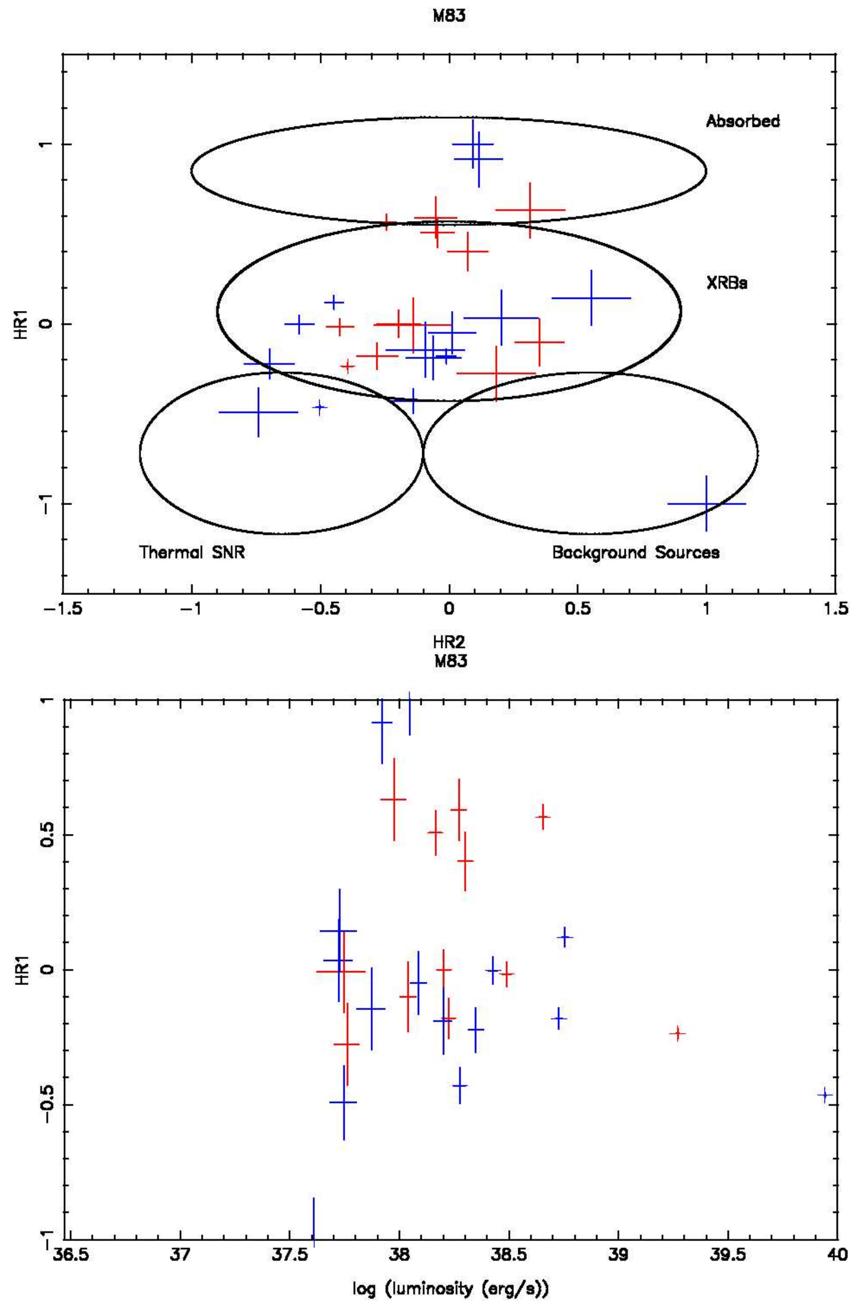

Figure 4.5: *Top panel:* Hardness ratios of the point sources in the disk of M83. *Bottom panel:* HR1 compared with broad-band luminosity for each source.

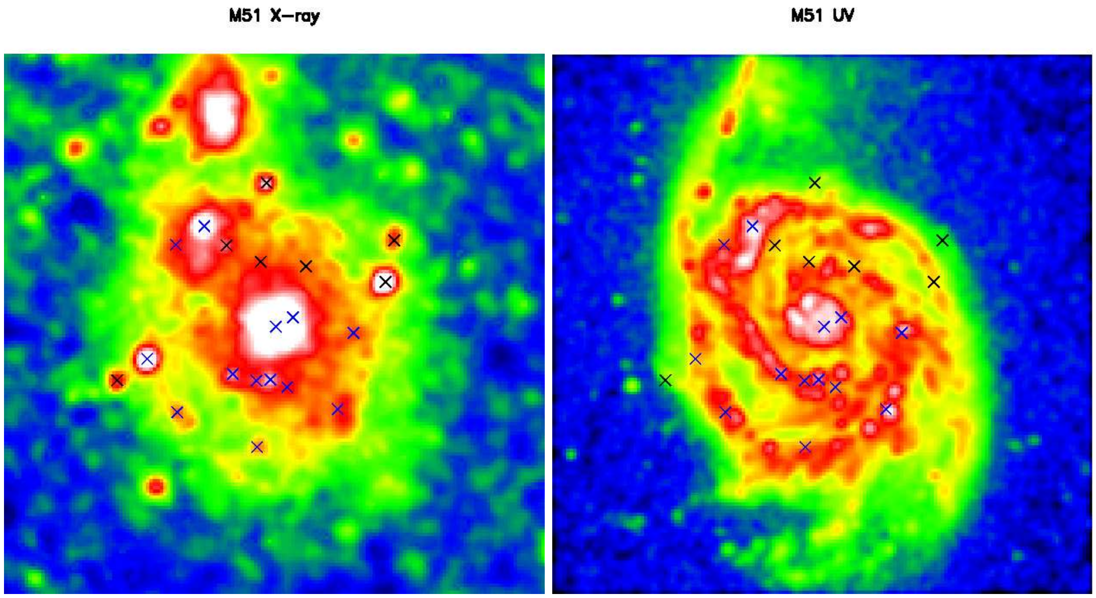

Figure 4.6: The locations of the X-ray point sources identified in the disk of M51. *Left panel:* Adaptively smoothed version of the *XMM-Newton* broad-band (0.3-6 keV) image showing the positions of the point sources used in our analysis. *Right panel: GALEX* FUV image with the positions of the X-ray sources superimposed.

$L_X > 10^{39}$ erg s^{-1}, only one of these is a likely candidate SNR. Of the 8 ULXs observed in the disk, three have colours consistent with X-ray binaries whilst the five previously mentioned have noticeably softer spectra. 6 out of 8 of these are coincident with the spiral arms, which is consistent with previous observations of ULXs, which tend to be found preferentially in areas of active star formation (Swartz et al. 2004). From the plot of hardness ratio against luminosity, the more luminous sources tend to have a softer colour, a trend which is consistent with our observations of M101. Our population of 12 sources with X-ray binary colours is split between on-arm and off-arm sources, which suggests that the colours of LMXB and HMXB sources are difficult to distinguish from each other. The corresponding survey of M51 in Kilgard et al. (2005) shows a similar clustering of soft sources and XRBs, with a much larger number of candidate SNRs present due to the higher sensitivity of their survey.

4.3.4 M74

At a distance from us of 11Mpc, M74 is one of the two furthest galaxies from us in our sample. The 2XMM catalogue for the primary observation contains 31 sources within the D_{25} of the galaxy, 12 of which passed our criteria for inclusion. Four of these sources are marked as on-arm, with the other eight

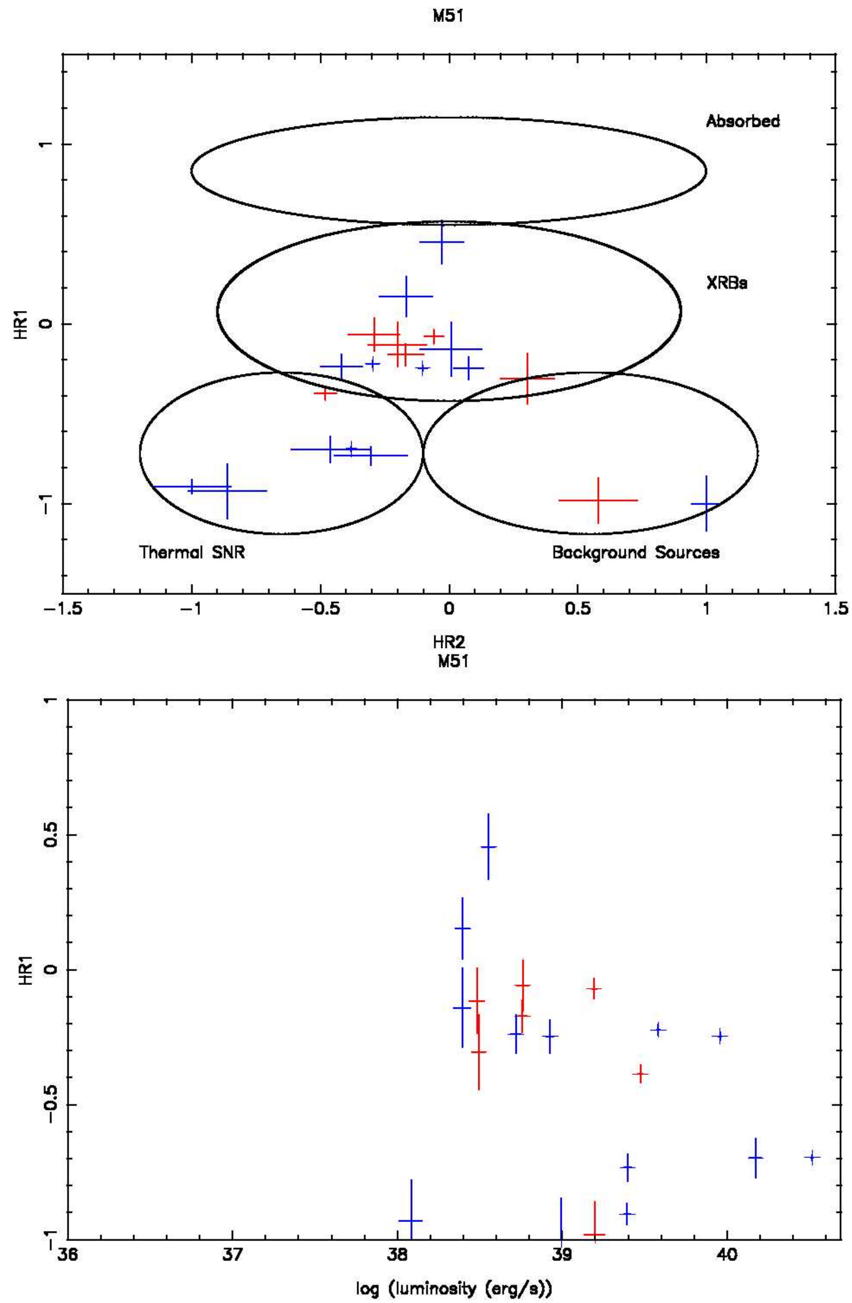

Figure 4.7: *Top panel:* Hardness ratios of the point sources in the disk of M51. *Bottom panel:* HR1 compared with broad-band luminosity for each source.

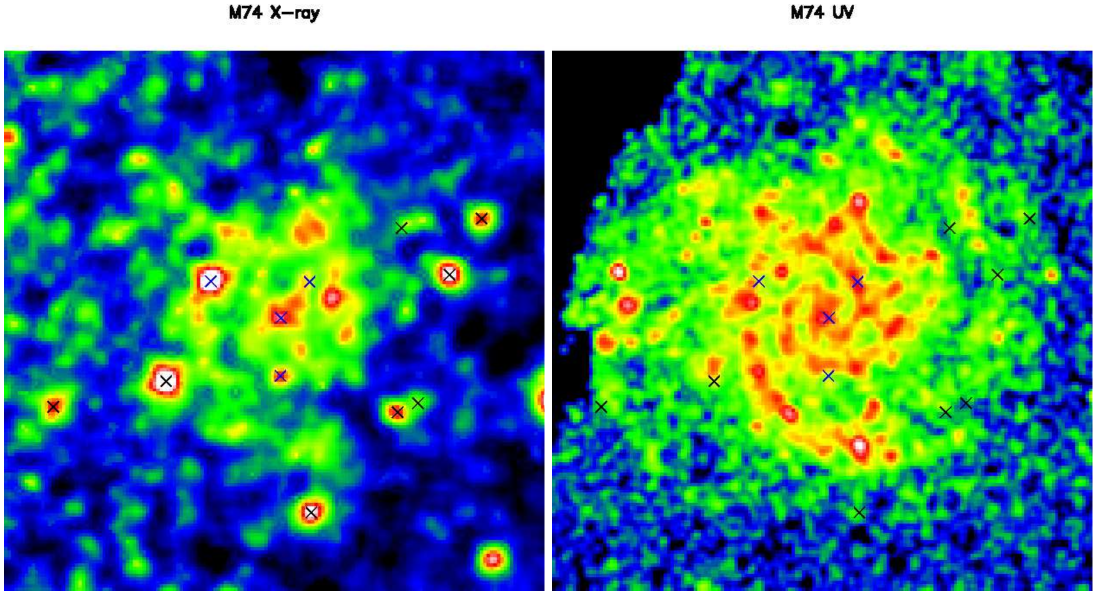

Figure 4.8: The locations of the X-ray point sources identified in the disk of M74. *Left panel:* Adaptively smoothed version of the *XMM-Newton* broad-band (0.3-6 keV) image showing the positions of the point sources used in our analysis. *Right panel: GALEX* FUV image with the positions of the X-ray sources superimposed.

off-arm (Fig. 4.8). The broad-band luminosity cutoff is at 1.5 $\times 10^{38}$ erg s^{-1} (0.2-12 keV). Three SNR candidate sources are detected (Fig. 4.9), with $L_X = 2 - 9 \times 10^{38}$ erg s^{-1}, two of which are off-arm. There is one absorbed source, and the other seven are consistent with XRB colours, including the three ULX candidate sources in the galaxy. Unusually for our sample, all three ULX sources are towards the outside of the disk, away from the spiral arm regions in the galaxy. The luminosity distribution of sources found above 10^{38} erg s^{-1} is similar to that found by Kilgard et al. (2005), as is the distribution of source colours.

4.3.5 NGC3184

NGC3184, at a distance of 11.6Mpc, is the furthest galaxy from us in our sample, and has the highest luminosity cutoff at 2×10^{38} erg s^{-1}. Of the 20 sources in the 2XMM catalogue for this observation, only 9 passed the threshold criteria for inclusion in our sample, with three of these located on the spiral arms (Fig. 4.10). Two of these sources have colours consistent with SNR (Fig. 4.11), although their high luminosity ($L_X = 1 - 2 \times 10^{39}$ erg s^{-1}) suggests that they are ULX candidate sources, which often have a softer spectral shape than other XRB systems. All other sources are consistent with XRB

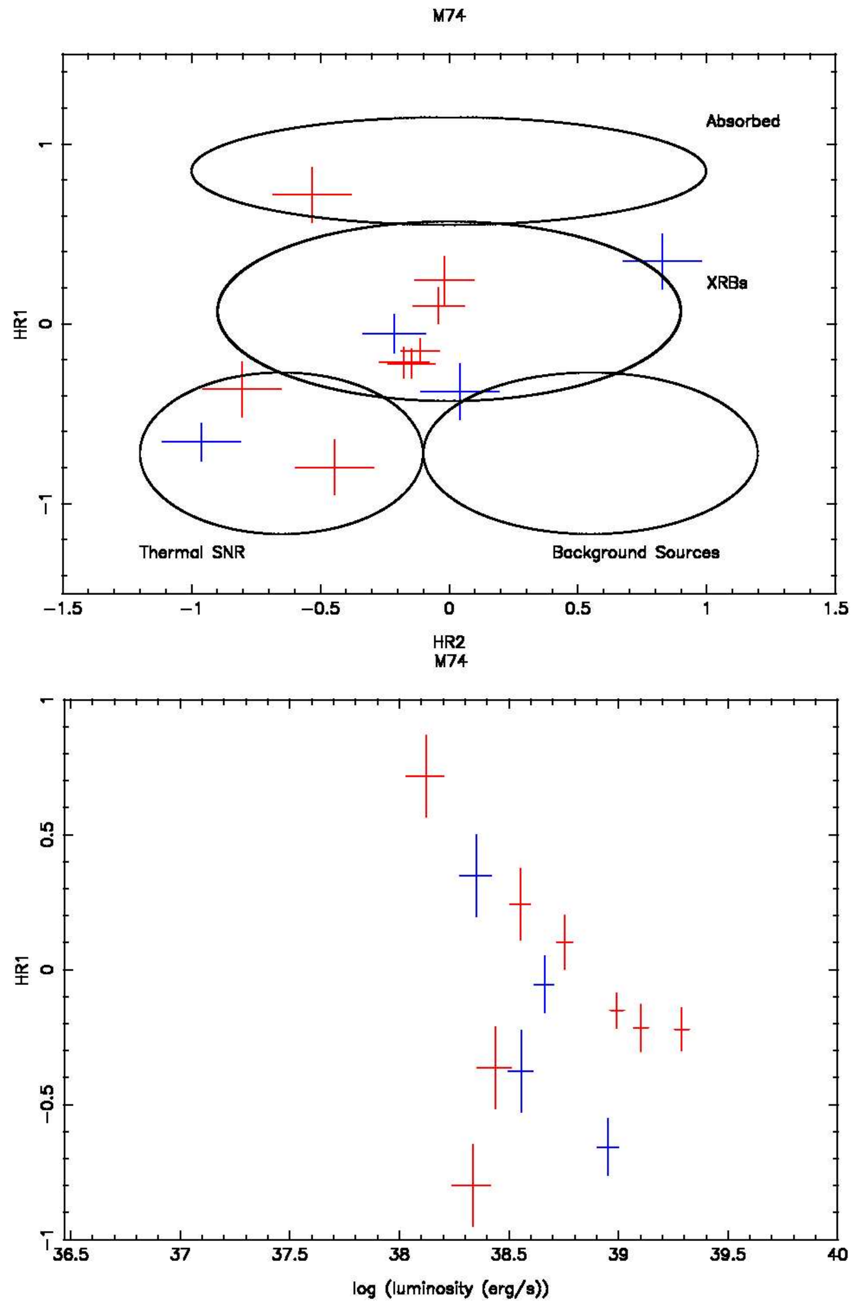

Figure 4.9: *Top panel:* Hardness ratios of the point sources in the disk of M74. *Bottom panel:* HR1 compared with broad-band luminosity for each source.

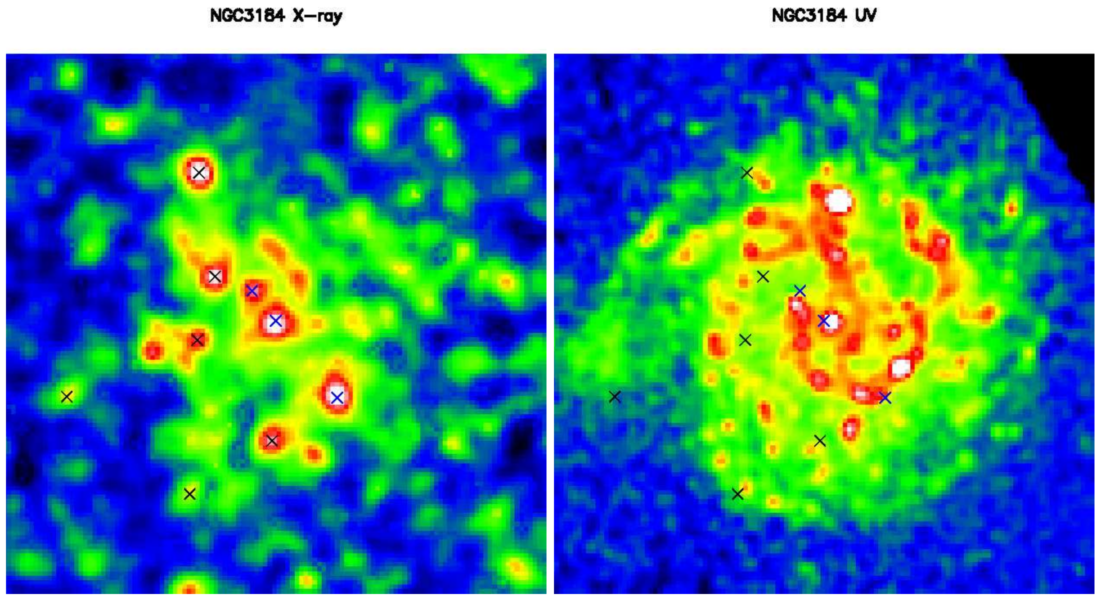

Figure 4.10: The locations of the X-ray point sources identified in the disk of NGC3184. *Left panel:* Adaptively smoothed version of the *XMM-Newton* broad-band (0.3-6 keV) image showing the positions of the point sources used in our analysis. The amplitude scaling shown is logarithmic. *Right panel:* *XMM-Newton* UVW1 image with the positions of the X-ray sources superimposed.

colours, including two other ULXs. All of the observed sources in our sample are clustered close together on the colour-colour plot, which agrees with *Chandra* analysis of this galaxy (Kilgard et al. 2005).

4.3.6 NGC300

At a distance of 2.0Mpc, NGC300 is the closest galaxy to us in our sample. As a result, it allows us to probe the source luminosity distribution deeper than for the other galaxies studied, down to a limiting luminosity of 3×10^{36} erg s^{-1}. Of the 88 sources included in the 2XMM catalogue sourcelist, 55 pass our filtering process and are included in the sample. 19 of these are marked as on-arm sources, with the remaining 36 located away from the spiral arms (Fig. 4.12). Given the luminosity range of the detected sources ($3 \times 10^{36} - 5 \times 10^{38}$ erg s^{-1}), the majority of these sources are expected to be a mixture of X-ray binary systems and relatively bright SNRs, and colour analysis bears this out (Fig. 4.13). 4 of the sources are classified as background AGN, which is approximately the number expected to be observed to our flux limit across a D_{25} disk of this size. A further three sources are highly absorbed, 12 are classified as SNR candidates and the remaining 36 have colours consistent with XRB sources.

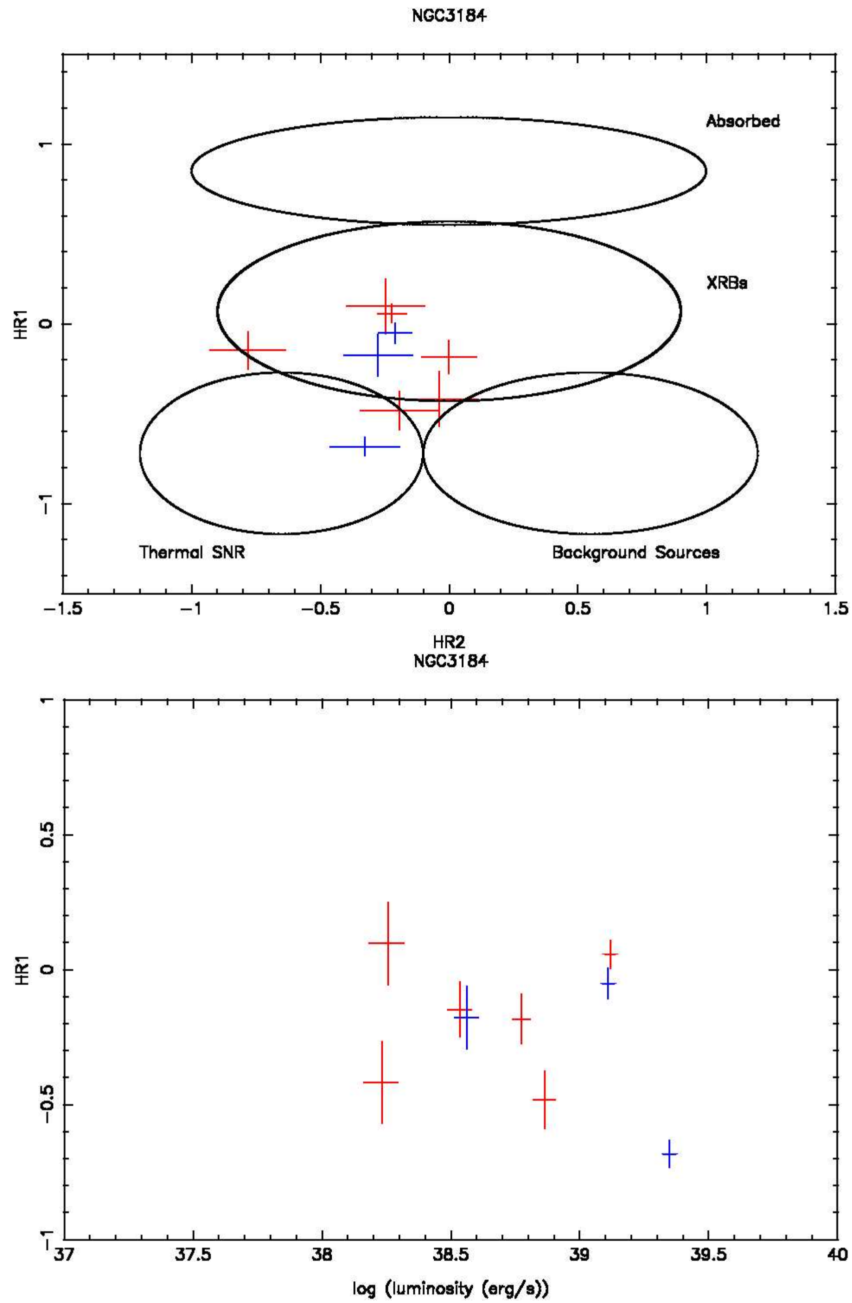

Figure 4.11: *Top panel:* Hardness ratios of the point sources in the disk of NGC3184. *Bottom panel:* HR1 compared with broad-band luminosity for each source.

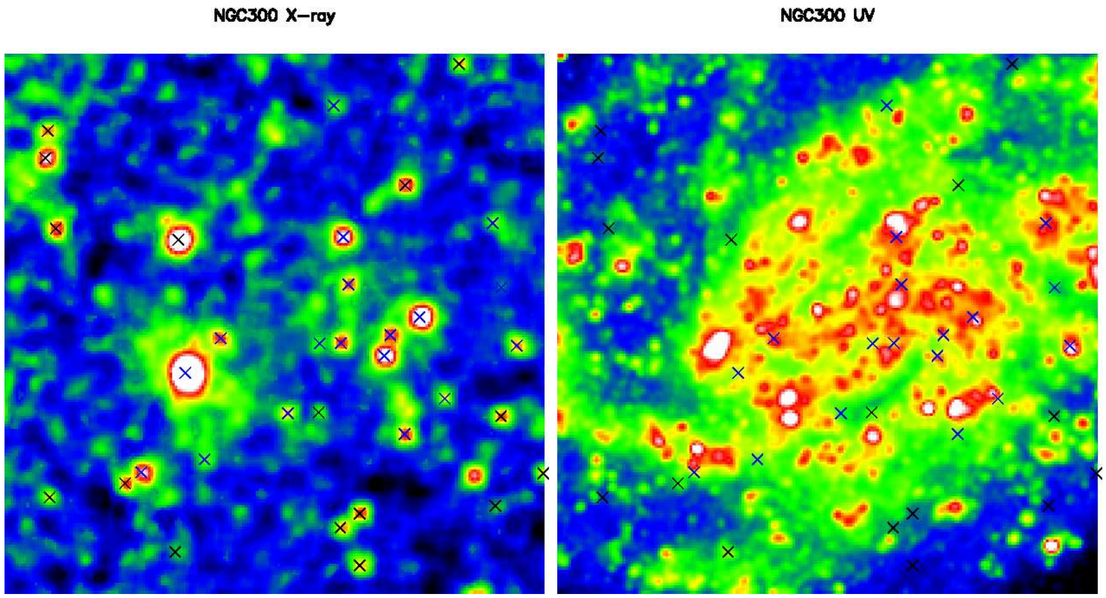

Figure 4.12: The locations of the X-ray point sources identified in the disk of NGC300. *Left panel:* Adaptively smoothed version of the *XMM-Newton* broad-band (0.3-6 keV) image showing the positions of the point sources used in our analysis. *Right panel: GALEX* FUV image with the positions of the X-ray sources superimposed.

As the Hubble type of NGC300 is Sd, it is difficult to distinguish between the "on-arm" and "off-arm" regions of the galaxy. This is because the spiral arms are tenuous and not significantly brighter than the rest of the galaxy disk. It is therefore possible that some young sources produced in star-forming regions are able to drift into the "off-arm" regions and vice versa. Caution must therefore be taken when attempting to classify point sources according to their location in this system. We expect to observe type II SNR candidates preferentially in areas of recent star formation, and this is reflected in the locations of these sources, with 9 of 12 found in the vicinity of the spiral arms of the galaxy. The three off-arm SNR candidates may have originated as type Ia supernovae, or they may be type II objects which have drifted out of the spiral arm regions. The luminosity range of these sources is consistent with them being SNRs rather than other soft luminous sources. There appears to be little spectral differentiation between the populations of XRB sources found in the on-arm and off-arm regions.

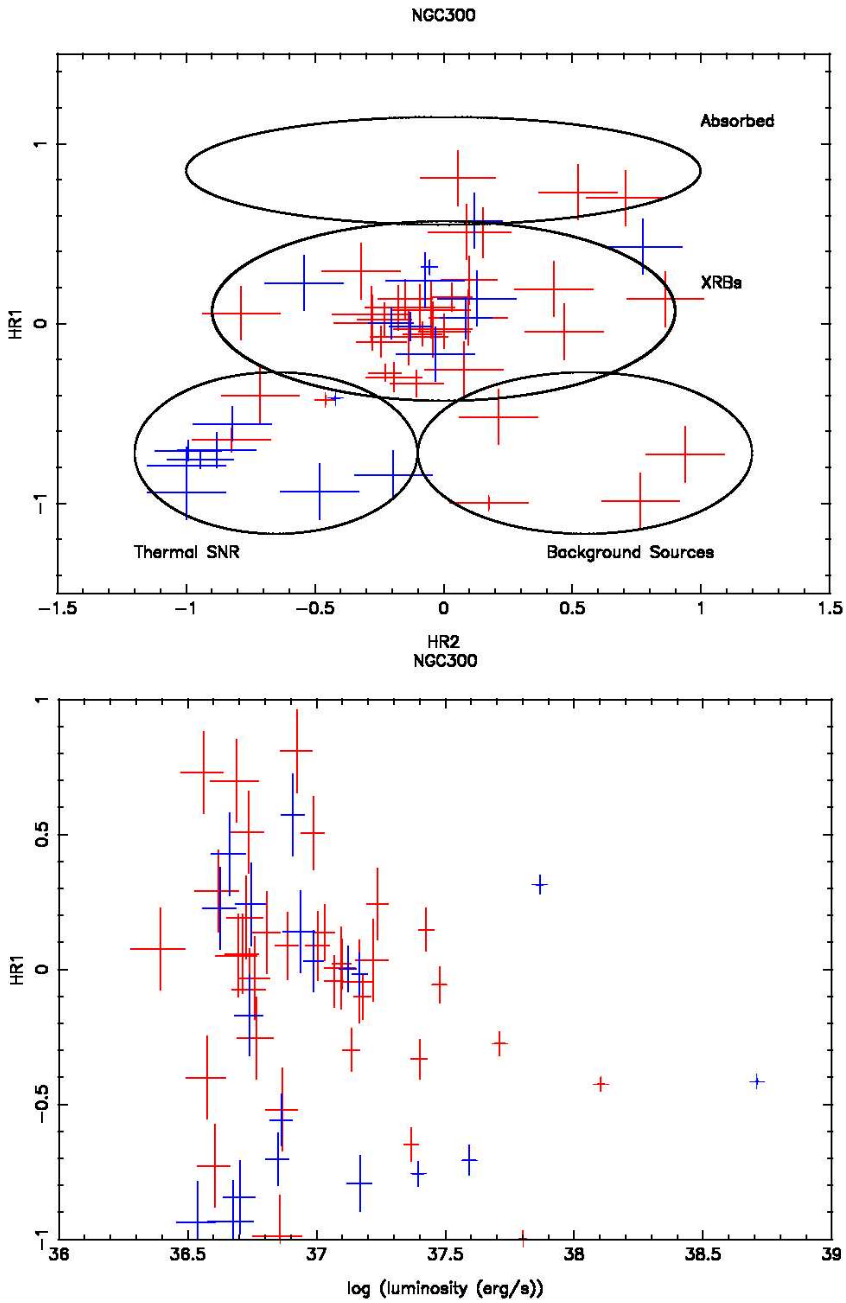

Figure 4.13: *Top panel:* Hardness ratios of the point sources in the disk of NGC300. *Bottom panel:* HR1 compared with broad-band luminosity for each source.

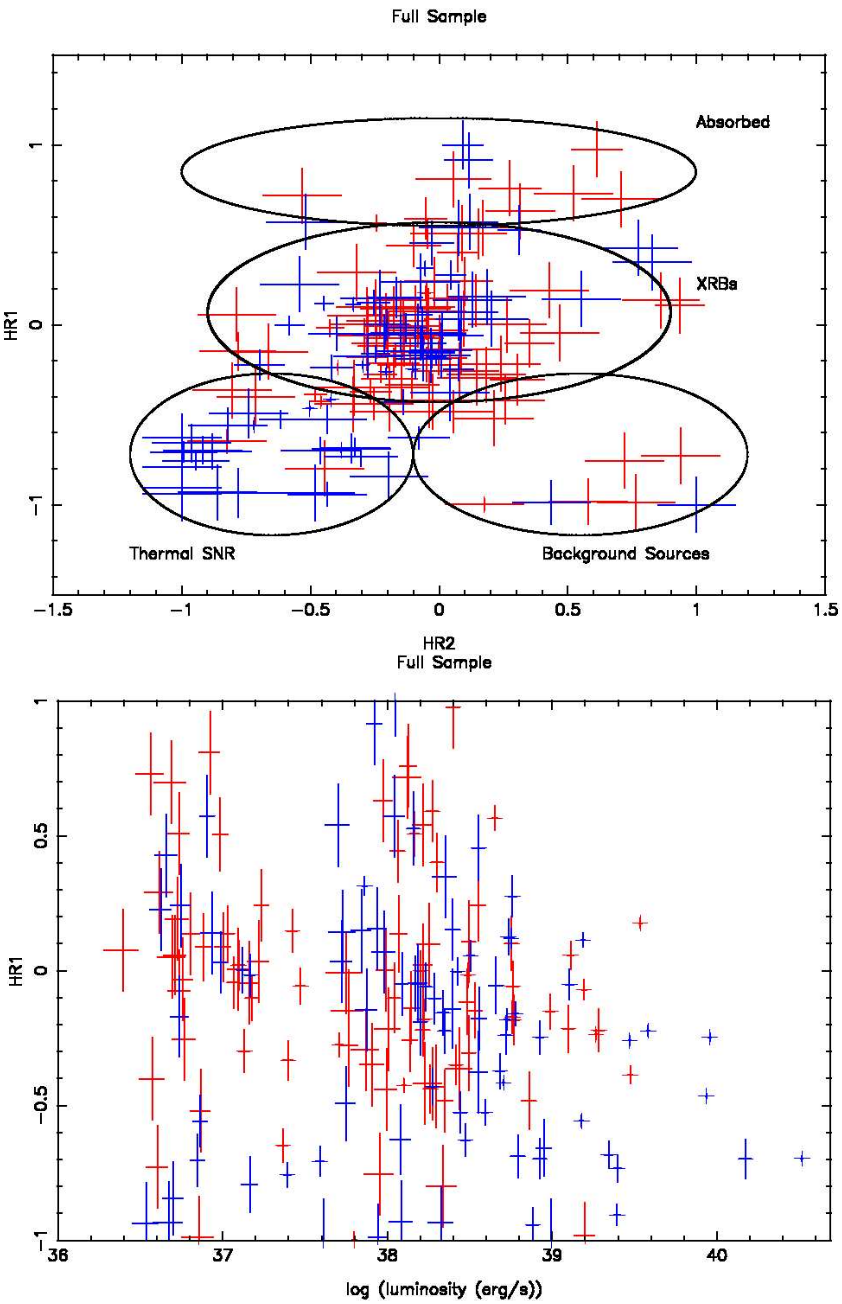

Figure 4.14: *Top panel:* Hardness ratios of the point sources in the disks of all of the galaxies in our sample. HR1 and HR2 are as defined in Fig. 4.3. *Bottom panel:* Soft hardness ratios of the sources compared with the broad-band luminosity of the source.

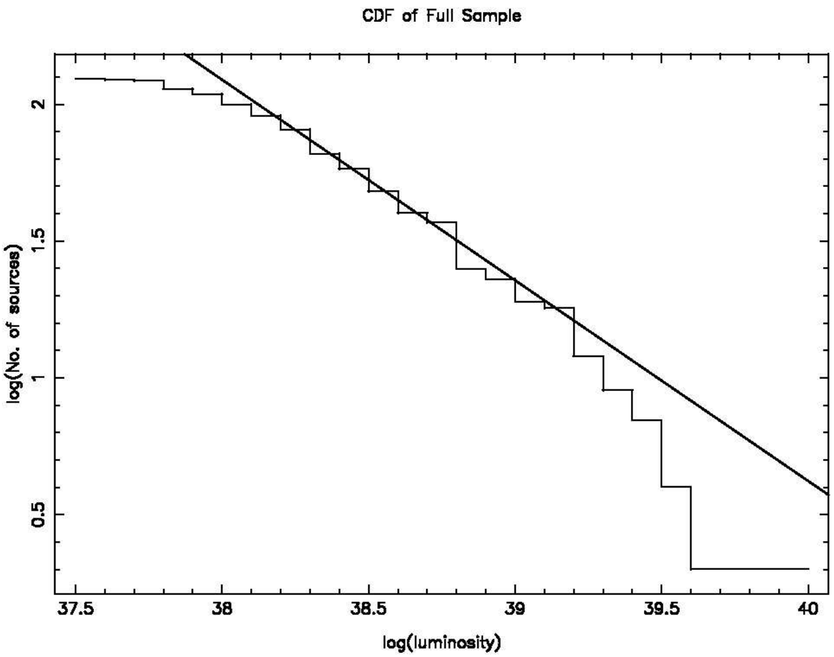

Figure 4.15: Cumulative luminosity distribution function of the point sources in our sample across all six galaxies. The best power law fit is shown, and has a gradient of -0.73±0.08.

4.4 Global properties of the point source sample

Fig. 4.14 shows the hardness ratio plot and broad-band luminosity distribution of the entire sample of 175 point sources across all six galaxies. Our lower limit for the broad-band X-ray flux detected from each source is $1 \times 10^{-14}\,\mathrm{erg\,cm^{-2}\,s^{-1}}$, which leads to significantly different luminosity thresholds for each galaxy. This can be seen in the hardness ratio vs. luminosity plot, where there is a gap in our luminosity function at $\mathrm{L_X} \approx 2 \times 10^{37}\,\mathrm{erg\,s^{-1}}$. All sources below this luminosity are in the disk of NGC300.

As fewer than ten of the sources have colours which indicate that they may be background AGN, the majority of our sources appear to be associated with the target galaxy. From the analysis of log N – log S distributions for extra high latitude sources by Campana et al. (2001), we expect to observe $\approx 20-25$ sources above our flux threshold in the disks of all six galaxies. Many background sources have been recorded with similar spectral shapes to X-ray binaries, so it is expected that ≈ 15 of the sources in the "XRB" region of our hardness ratio plot may be background AGN.

21 of the sources are detected with $\mathrm{L_X} > 10^{39}\,\mathrm{erg\,s^{-1}}$ in the broad band (0.2-12 keV) and comprise the ULX population across the sample. From the luminosity-hardness plot, HR1 for these sources is

significantly lower than the average across the entire sample, confirming that these sources are generally soft. Whereas there is a very large spread in hardness ratio for the lower luminosity end of our source sample, this narrows significantly for the high luminosity end, where the sources are observed to be spectrally softer. As shown in the analysis of the individual galaxies, the spectral colours of these high luminosity sources are similar to SNR or the softer end of the XRB population. This agrees with previous studies of ULX spectral properties by Irwin et al. (2003), which find similarities between ULX spectra and those of galactic BH binaries, and Roberts et al. (2005) and Kaaret et al. (2003), which discovered strong soft components in the spectra of several ULXs. Spatially, we find some association of these sources with star forming areas in the galaxy, with slightly over half of them coincident with the spiral arms. Indeed, the five sources with the highest broad-band luminosity are all on-arm sources. This agrees strongly with previous observations by Liu & Mirabel (2005).

The hardness ratio plot shows a grouping of very soft sources with colours characteristic of SNRs. Some of these are classified as ULXs due to their high luminosity, whereas the remainder are strong SNR candidates. The population of type II SNR candidates is expected to be strongly correlated with recent star formation activity in the host galaxy, due to the short lifetimes of the progenitor, and we find that the overwhelming majority of these sources are coincident with spiral arms in the UV emission. The apparent deficit of SNRs outside the spiral arms of the galaxies implies a low number of bright type Ia SNR sources present, suggesting that the brightest SNRs observed are associated with the young stellar population.

The population of sources found with characteristic colours typical of X-ray binaries is split between sources found on-arm and those found off-arm, with little distinction between the two populations. There is no obvious difference in colour observed between HMXB and LMXB populations in the disk. Of the populations of sources wth XRB colours in the galaxies (excluding NGC300, for which the spatial distribution of sources is less clear), approximately equal numbers are detected in the spiral arm regions as in the off-arm regions. On average, the spiral arm regions occupy 20-25% of the overall disk area, so if the LMXB population is evenly distributed across the disk, we expect $\approx 25\%$ of the sources detected in spiral arm regions of the galaxies to be LMXBs. Of the high luminosity ($L_X >$ 2×10^{37} erg s^{-1}) XRB sources present in our sample, we estimate that $\approx 60 - 65\%$ are LMXBs.

The cumulative luminosity distribution function (CDF) of the point source population is shown in Fig. 4.15, along with the best fit line between 1×10^{38} erg s^{-1} and 2×10^{39} erg s^{-1}. Below the lower limit, our source sample is incomplete, leading to a levelling off of the luminosity distribution, and at high luminosity low number statistics dominate. Between these two limits, a power law fit with gradient -0.73±0.08 fits the data. This is in between than the CDF gradients found for populations of HMXBs and LMXBs in several nearby galaxies (Grimm et al. 2005; Kilgard et al. 2005; Colbert et al. 2004). This suggests that the high luminosity X-ray point source population is split between the old and young stellar populations.

4.5 Conclusions

Using the system of X-ray point source classification by hardness ratios derived by Prestwich et al. (2003) and modified by Kilgard et al. (2005), we have studied the bright X-ray point source population in a sample of six nearby face-on spiral galaxies. We find that the luminosity function of the point sources above 10^{38} $\mathrm{erg\,s^{-1}}$ (0.2-12 keV) is well fit with a single power law with gradient -0.73±0.08, in between the CLF gradients for HMXBs and LMXBs in other nearby galaxies. We find that there is a clear distinction between the populations of sources in different regions of the host galaxies, with candidate SNRs almost entirely coincident with the spiral arms. This implies that the majority of bright SNRs present in these systems are associated with the young stellar population. More ULX sources are found in the spiral arms of their host galaxy than elsewhere in the galactic disk, whereas X-ray binaries are spread out across the entire disk, suggesting that comparable numbers of bright HMXB and LMXB sources are present. We estimate that at high luminosity, $\approx 60 - 65\%$ of the XRB sources present in our sample are LMXBs. For the most luminous sources in our sample, we observe some spectral softening compared to the colour distribution at lower luminosity. These results suggest that the bright X-ray population contains comparable contributions from the old and young stellar populations in our sample of galaxies.

Chapter 5

XMM-NEWTON Analysis of Extended X-ray Emission from M33

5.1 Introduction

The X-ray emission observed from spiral galaxies comprises several components: emission from bright resolved pointlike sources, which include high-mass and low-mass X-ray binary systems (HMXBs and LMXBs), a lower luminosity point source population, which includes supernova remnants (SNRs), active binary systems (ABs) and stellar coronal emission, and truly diffuse emission from hot gas in the galactic disk and halo. The extent to which these components can be distinguished from each other depends on the spatial resolution and sensitivity of the detector and the distance to the target galaxy. Early X-ray observations using the *Einstein* detector were able to detect the brightest point source population in a range of nearby galaxies (Fabbiano 1989), whilst also finding underlying extended emission in complex structures. Understanding of this emission improved with the superior spatial resolution of *ROSAT* which allowed study of the unresolved, seemingly diffuse component in in a number of spiral galaxies (*e.g.* , Read et al. 1997). More recent *XMM-Newton* and *Chandra* studies, with their improved collecting area and spatial and spectral sensitivity, have permitted identification of the populations of point sources in galaxies to much fainter luminosities than previously attained (*e.g.* Strickland et al. 2004a, Colbert et al. 2004, Fabbiano 2006), as well as detailed analysis of the spatial extent of the residual unresolved emission. As a result, the X-ray luminosity function (XLF) for HMXB and LMXB populations in several spiral galaxies has been constructed, from which the aggregated luminosity of point sources too faint to be detected can be inferred. In this way, it is possible to estimate how much of the unresolved emission we observe in a galactic disk is truly diffuse.

In our previous papers (Warwick et al. 2007, hereafter W07; Owen & Warwick 2009, hereafter OW09 and Chapter 3), we studied the radial profiles of soft X-ray emission and star formation rate in a sample of six nearby face-on spiral galaxies, after excision of the bright point source population. We confirmed the close relationship between soft X-ray emission and SFR, with the suggestion that the diffuse X-ray to SFR ratio is higher in regions of high SFR density. This relationship can be further explored by analysis of galaxies closer to us, in which the majority of HMXBs and LMXBs can be identified and extracted. In this way, it should be possible to estimate the amount of truly diffuse emission present with far greater accuracy.

M33 is an Sc spiral galaxy with an inclination of $56°$ (Zaritsky et al. 1989) at a distance of 795kpc (van den Bergh 1991), and is the third largest galaxy in the Local Group. Its proximity to us permits detailed study of the population of X-ray point sources present and enables spatial distinction of these sources from the diffuse gas located in the disk. The relatively low Galactic foreground $N_H(6 \times 10^{20}$ cm^{-2}; Stark et al. 1992) in the direction of M33, its moderate inclination, and high star formation rate in comparison to the Milky Way and M31 (0.3-0.7 $\mathrm{M_{\odot}yr^{-1}}$, Hippelein et al. 2003) make M33 an ideal candidate for study of soft X-ray emission in its disk.

Early *Einstein* observations of M33 discovered a total of 17 point sources, including the bright ULX M33 X-8 (Long et al. 1981; Markert & Rallis 1983; Trinchieri et al. 1988). The last of these also found evidence for the presence of a soft diffuse component in the plane of the galactic disk. *ROSAT* observations (Schulman & Bregman 1995; Long et al. 1996) greatly expanded the known population of X-ray point sources in the direction of M33 to a total of 184 (Haberl & Pietsch 2001). With the advent of *Chandra* and *XMM-Newton* , the spatial and spectral sensitivity of observations was greatly increased, with a total of 350-400 X-ray point sources to a limiting X-ray luminosity of 10^{35} erg s^{-1} identified and categorized (Foschini et al. 2004; Misanovic et al. 2006; Grimm et al. 2005; Grimm et al. 2007; Pietsch et al. 2004). The majority of studies to this point have focused on the X-ray emission from point sources, but Haberl & Pietsch (2001) and Pietsch et al. (2004) have noted the presence of seemingly diffuse structures along the spiral arms. It is this component which we examine in this chapter.

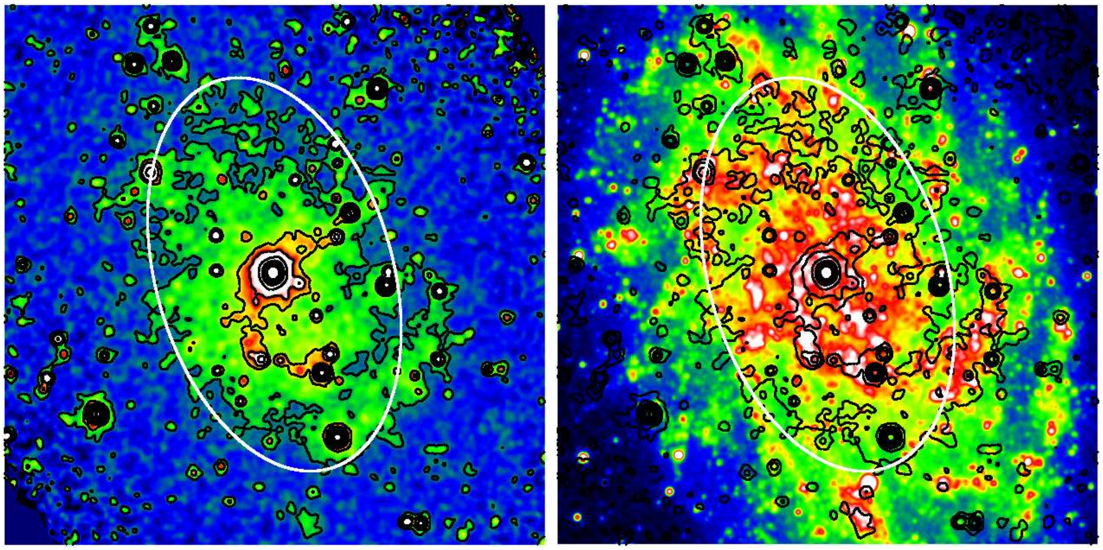

Figure 5.1: Comparison of the soft X-ray and far-ultraviolet images of M33. *Left-hand panel:* Adaptively smoothed versions of the *XMM-Newton* pn+MOS images in the soft (0.3-1 keV) band. The amplitude scaling in all cases is logarithmic with the contour levels representing factor two steps in the soft X-ray surface brightness. The marked ellipse shows the area used for image and spectral analysis, and has a major axis radius of 15′ . *Right-hand panel:* The *GALEX* FUV ($\lambda_{eff} = 1528$ Å) image on the same spatial scale as the X-ray data.

In this chapter, we focus on the spectral and spatial properties of the unresolved X-ray emission from the inner disk of M33, deduced from archival *XMM-Newton* observations. In §5.2, we describe the properties of the set of observations used to construct soft-band X-ray images and outline the methods used for data analysis. In §5.3, we briefly examine the properties of the collated point source population and spatial distribution of the soft X-ray emission compared with *GALEX* FUV data. We follow this with spectral analysis of the bright point source population and unresolved, residual emission (§5.2.3). We examine the spatial extent of the X-ray emission in comparison with star formation data (§5.5) for M33, and compare this relationship to that found for a number of other nearby late-type spiral galaxies. Finally we discuss the implication of our results (§5.6) and summarize our conclusions (§5.7).

5.2 Observations and Data Reduction

In previous papers (W07; OW09), we reported the results of an *XMM-Newton* study of six nearby face-on galaxies, namely M101, M83, M51, M74, NGC300 and NGC3184. Here we use a similar

Table 5.1: Details of the *XMM-Newton* observations of M33 utilised.

Galaxy	Observation ID	Start Date	Filter [a]	Target co-ordinates		Useful exposure (ks)	
		(yyyy-mm-dd)	pn/MOS1/MOS2	RA (J2000)	Dec (J2000)	pn	MOS 1+2
M33	0102640101[c]	2000-08-04	M/-/-	$01^h33^m51.0^s$	$+30°\ 39'\ 37''$ [b]	7.1	-
	0102640201	2000-08-04	M/M/M	$01^h34^m40.0^s$	$+30°\ 57'\ 48''$	11.8	31.5
	0102640301	2000-08-07	M/M/Tn	$01^h33^m32.0^s$	$+30°\ 52'\ 13''$	3.6	9.5
	0102640401	2000-08-02	Tk/Tk/Tk	$01^h32^m51.0^s$	$+30°\ 36'\ 49''$	9.1	23.1
	0102640501	2001-07-05	M/M/M	$01^h33^m02.0^s$	$+30°\ 21'\ 24''$	9.2	23.1
	0102640601	2001-07-05	M/M/M	$01^h34^m08.0^s$	$+30°\ 46'\ 06''$	4.5	11.9
	0102640701	2001-07-05	M/M/M	$01^h34^m10.0^s$	$+30°\ 27'\ 00''$	6.9	21.9
	0102640801	2001-07-07	-/M/M	$01^h34^m51.0^s$	$+30°\ 42'\ 22''$	-	3.2
	0102640901	2001-07-08	M/M/M	$01^h34^m04.0^s$	$+30°\ 57'\ 25''$	3.9	11.2
	0102641001	2001-07-08	M/M/M	$01^h33^m07.0^s$	$+30°\ 45'\ 02''$	1.5	16.3
	0102641101	2001-07-08	M/M/M	$01^h32^m46.0^s$	$+30°\ 28'\ 19''$	8.0	21.0
	0102641201	2000-08-02	Tk/Tk/Tk	$01^h33^m38.0^s$	$+30°\ 21'\ 49''$	12.0	7.2
	0102642001	2001-08-15	M/M/M	$01^h34^m51.0^s$	$+30°\ 42'\ 22''$	8.8	22.3
	0102642101	2002-01-25	M/M/M	$01^h34^m34.0^s$	$+30°\ 34'\ 11''$	10.0	24.3
	0102642201	2002-01-25	M/M/M	$01^h34^m56.0^s$	$+30°\ 50'\ 52''$	11.5	27.3
	0102642301[c]	2002-01-27	M/M/M	$01^h33^m33.0^s$	$+30°\ 33'\ 07''$	9.9	24.1
	0141980101	2003-07-11	M/M/M	$01^h33^m07.0^s$	$+30°\ 45'\ 02''$	6.2	13.2
	0141980201	2003-07-11	M/M/M	$01^h34^m04.0^s$	$+30°\ 57'\ 25''$	13.0	28.8
	0141980301	2003-07-25	-/M/M	$01^h34^m08.0^s$	$+30°\ 46'\ 06''$	-	1.2
	0141980501	2003-01-22	M/M/M	$01^h33^m51.0^s$	$+30°\ 39'\ 37''$	1.9	17.0
	0141980601	2003-01-23	M/M/M	$01^h32^m51.0^s$	$+30°\ 36'\ 49''$	11.0	25.9
	0141980701	2003-01-24	M/M/M	$01^h33^m38.0^s$	$+30°\ 21'\ 49''$	4.4	11.4
	0141980801[c]	2003-02-12	M/M/M	$01^h33^m51.0^s$	$+30°\ 39'\ 37''$	7.8	19.8

[a] - Tn = thin filter, M = medium filter, Tk = thick filter

[b] - Assumed position of the galactic nucleus.

[c] - Observations used for spectral annalysis.

methodology to incorporate M33 into our sample, in order to effectively compare the X-ray characteristics between galaxies. Since M33 has a D_{25} diameter of $70'$, which extends significantly beyond the EPIC (European Photon Imaging Camera) field of view, observations from the multiple pointing survey conducted by Pietsch et al. (2004) were used. Details of these *XMM-Newton* observations of M33 are summarised in Table 5.1.

Data reduction was based on SAS v8.0. The datasets were screened for periods of high background through creation of full-field 10–15 keV lightcurves. MOS data were excluded when the 10–15 keV count-rate in a 100s bin exceeded 0.2 $\mathrm{count\ s^{-1}}$, whereas pn data were excluded above 2 $\mathrm{count\ s^{-1}}$ in the same band. The resulting exposure times after filtering the observations, as seen in Table 5.1, range from 1.9 to 13 ks in the pn camera, with typically slightly greater exposure in the MOS cameras. Several of the pn datasets which include the bright ULX near the nucleus of M33 are affected by Out Of Time (OoT) events. These are events which are registered during readout of the pn CCD and are hence assigned an incorrect position, appearing in images as a stripe leading from the image position to the readout node of the detector. The SAS tasks *epproc* and *epchain* were used to create OoT event lists and images of OoT event positions. These were subtracted from the raw images produced from the full event lists to produce images cleaned of OoT events, which could then be used for imaging analysis.

In Chapters 2 and 3, it was shown how an appropriate spatial mask could be used to excise the bright source population in the galaxy disk from the residual emission, thus reducing the "contamination" present in analysis of this diffuse component. Here we employ a slight modification of this imaging analysis, necessitated by the need to mosaic the data sets from the component observations.

5.2.1 Image Construction

The majority of the image construction follows the same lines as in Chapter 3, and the same energy bands (0.3-1 keV, 1-2 keV and 2-6 keV) are used for consistency. Emphasis in our analysis is placed on the 0.3–1 keV band, which contains the majority of the diffuse signal present. Images and exposure maps were extracted for all three bands and cameras for each observation. The images had a constant particle rate subtracted (estimated from the corners of the detector not exposed to the sky) and were divided by the relevant exposure maps to create flat-field images, which were added together by the method detailed in §2.2. The images from each observation were then combined, with a position offset

Table 5.2: Characteristics of the bright X-ray source population in M33.

Galaxy	X-ray Region[a] ($'$)	Threshold L_X[b] (10^{35} erg s^{-1})	Number in Source List	Number of high L_X sources ($L_X > 5 \times 10^{38}$ erg s^{-1})
M33	30.0	2.0	92	1

[a] - Diameter of the major axis "X-ray extraction region".

[b] - Nominal L_X threshold applied in the 0.3–6 keV band in defining sample.

dependent on the pointing direction of the observation, to create a mosaiced image of the full galaxy. Compensation for different camera filters used and different background sky levels was necessary to create a truly flat image. This was achieved by imposing a mask on the combined image consisting of the source mask derived in §5.2.2 plus an elliptical mask extending to a major axis radius of $15'$ from the nucleus of the galaxy. Assuming that the extended X-ray emission from the galaxy is negligible beyond this radius, the masked X-ray intensity across the field is indicative of the X-ray sky background level. Through inspection of the raw images, this assumption appears to be justified. This level was then compared across all observations, and the background level scaled to be uniform. As a result of this correction, analysis of M33 images is only justified for the region extending from the nucleus to a major-axis radius of $15'$. This corresponds to a radius of 3.5kpc, which is comparable to the analysis performed for the other galaxies in our sample.

5.2.2 Spatial masking of bright sources

The catalogue of sources used to produce the spatial mask for M33 was derived from that produced by Misanovic et al. (2006), who found 350 X-ray sources across the D_{25} disk of M33 above a luminosity of 2×10^{35} erg s^{-1}. 92 of these sources lie within the elliptical region defined in §5.2.1. Following the methods detailed in §2.2, a model "bright source image" was created for M33. A surface brightness cut was applied to this image at a level of 0.07 pn+MOS1+MOS2 ct ks^{-1} pixel^{-1} to produce the source mask, leading to a "spillover" fraction (*i.e.* the fraction of the bright source signal not contained within the masked region) of 4%. This mask was used to separate the "bright source region" from the "residual emission region" in spatial and spectral analysis. For image analysis, contamination of the residual galaxy signal by bright sources was removed through subtraction of the simulated image from the corresponding pn+MOS image and imposition of the source mask, whereas for spectral analysis, a fraction of the combined source spectrum was included in the spectral fit of the residual emission.

Table 5.3: Contribution of point sources to the total X-ray luminosity.

Galaxy	Spillover/Area Factors (%)	Component	$L_X(10^{38}$ erg s$^{-1})$			
			(0.3-1 keV)	(1-2 keV)	(2-6 keV)	(0.3-6 keV)
M33	4/6	Resolved Sources	5.6	4.0	6.2	15.8
		Unresolved Sources[a]	[0.04]	[0.03]	[0.05]	
		Residual Galaxy	1.1	0.1	-	1.2
		Total Measured	6.7	4.1	6.2	17.0

[a] - Extrapolated to $L_X = 1 \times 10^{35}$ erg s^{-1}

5.2.3 Spectral Extraction

The soft-band image in Fig. 5.1 demonstrates the existence of an extended emission component in addition to the population of bright point sources. On the basis of the approach described earlier, we extracted the integrated pn spectrum of both the bright source region (bounded by the spatial mask) and the residual emission region (corresponding to the full X-ray extraction region less the masked area) within a major axis radius of $15'$ from the nucleus. This was done for the three observations indicated in Table 5.1, which were chosen due to the relatively long exposure times and pointing directions which encompassed the central region of the galaxy. A narrow strip of one CCD contaminated by Out of Time (OoT) events from the ULX was excised in each observation. The SAS tools *arfgen* and *rmfgen* were used to produce appropriate Auxiliary Response File (ARF) and Response Matrix File (RMF) files for the source and residual galaxy regions, and the counts recorded in adjacent (raw) spectral channels were summed to give a minimum of 20 counts per spectral bin in the final set of spectra.

The large extent of the bright source and residual emission areas make the process of background subtraction a lot more complex than for most *XMM-Newton* data. In Chapter 3, we used appropriately scaled spectra from an annulus surrounding the defined galaxy region and the corner regions of the detector to approximate the background. This process was not viable for M33 as the central galaxy field covered too large a fraction of the EPIC pn field of view, making the extraction of a large enough background region so as to give acceptable spectral signal to noise impossible. We therefore used a combination of "blank-sky" fields extracted from a region of sky close to M33 (to minimize the difference in the sky X-ray background) and "filter-wheel closed" data to produce a background spectrum.

Using the SAS tool *skycast*, a mosaic blank-sky pn image was rotated to the same attitude as each observation, and our spatial mask imposed for the bright source and residual regions. Spectra were then extracted from these areas and scaled to the same exposure time as for the observation. The same process was followed for filter-wheel closed data to produce a particle background spectrum. The raw pn and blank-sky spectra were compared in the 8–12 keV band, where the signal is dominated by the particle background. The difference in this signal was compensated for by addition of a relevant fraction of the filter-wheel closed spectrum, the effect of which was to ensure the particle background level for source and background spectra was the same.

5.3 Properties of the galactic X-ray emission

5.3.1 The contribution of luminous point sources

The relative proximity of M33 means that source extraction for this galaxy can be performed to a luminosity level a factor of 100 deeper than in the majority of our galaxy sample. Most LMXB and HMXB sources are therefore removed by the source masking process. The collective X-ray luminosity (0.3-6 keV) of the bright source population within the source mask is measured to be 1.6×10^{39} erg s^{-1}, which is dominated by the bright ULX, M33 X-8. This luminosity measurement is in line with previous studies of this source (Dubus et al. 1997; Foschini et al. 2004). This source is coincident with the optical nucleus of the galaxy, but short-term variability in the X-ray emission suggests that it is not the galactic nucleus itself. Analysis by Foschini et al. (2004) of this ULX suggests that the object is a black hole of mass $\approx$10 $M_{\odot}$accreting at a super-Eddington rate. Table 5.3 summarizes the distribution of the collated source flux across the three energy bands, which is derived from the best fit spectral models in Table 5.4. As in our previous analysis, the $L_X$figures derived are corrected for foreground galactic absorption. Correction factors were also applied for spillover of source counts into the residual galaxy area and for residual emission encompassed by the source mask.

It is possible to estimate the X-ray luminosity of point sources below our $L_X$threshold with similar spectral characteristics to the bright sources already identified. For this, we use the *Chandra* M33 observations of Grimm et al. (2005), which study the same area of the galaxy we examine here. They derive an X-ray luminosity function with a slope of -0.74 to -0.78, which we use to estimate the total

L_X for sources between 2×10^{35} erg s^{-1} and 1×10^{35} erg s^{-1}. The results are given in Table 5.3, and show that unresolved X-ray binaries do not contribute significantly to the residual X-ray emission observed in the soft band, but may form a significant contribution to the emission observed above 1 keV. This implies that the residual emission measured is due to a combination of contributions from truly diffuse emission, energized by supernovae and stellar winds, and the integrated population of lower luminosity sources such as cataclysmic variables and active binaries.

5.3.2 Morphology of the residual X-ray emission

Fig. 5.1 shows the comparison of soft (0.3–1 keV) X-ray emission from M33 with FUV emission from *GALEX* images. The *GALEX* images were resampled to the same spatial scale as the *XMM-Newton* images, and were then lightly smoothed with a gaussian mask with $\sigma \approx 4''$. There is clear correlation between these images, although the FUV emission extends further from the nucleus than the X-ray emission. Most of the X-ray emission is contained within a major-axis radius of 15 $'$ of the nucleus (marked on the images), and traces the inner spiral arms of the galaxy closely. This general correlation confirms the close relationship between X-ray emission and star formation in the inner galactic disk. From spectral analysis (see §5.4.2) we estimate the underlying residual X-ray emission has a luminosity of $L_X = 1.2 \times 10^{38}$ erg s^{-1} (0.3–2 keV).

5.4 Spectral Analysis

The methodology outlined in §5.2.3 was used to extract bright-source and residual-galaxy spectra for three observations. Only EPIC pn data was used for spectral fitting, due to its superior sensitivity in the soft-band over MOS data. For each observation, the bright source spectrum was fit separately to allow for possible spectral variation between observations (and also to take account of the fact that some of the sources encompassed by one observation might fall outside the field of view in another). The residual galaxy spectra for the three observations were then extracted, but in this case fit simultaneously. The overspill of the bright sources beyond the mask was accounted for in each observation by including a “bright source” contribution to the model spectrum. The spectral fitting was carried out using the software package XSPEC version 12.5.

5.4.1 Spectra of the bright source regions

In all three observations studied, the bright source population is dominated by M33 X-8, the ULX close to the nucleus of the galaxy. It follows that the collated source spectrum will also be dominated by this source. We therefore attempted to fit these spectra in each case with the ULX spectral models derived by Foschini et al. (2004). In each case, the best fit model was an absorbed power law with a multicolour black-body disk component (see Fig. 5.2). The spectral parameters derived are slightly different than was found by Foschini et al. (2004), which we attribute to the influence of the rest of the bright source population, the majority of which is expected to be composed of HMXB and LMXB sources modelled by a simple unabsorbed power-law. The source spectrum changes slightly between observations, which is likely due to long-term spectral variability of the ULX source.

5.4.2 Spectra of the residual-galaxy regions

The simultaneously fit spectra for the residual emission are shown in Fig. 5.2. The models used to fit these spectra consist of the aforementioned percentage of the combined source spectrum plus an unabsorbed combination of two thermal plasma components. A model comprising two MEKAL components was found to provide a good fit to the residual galaxy spectrum. A “cool” thermal component was required at kT ≈ 0.2 keV, along with a “hot” thermal component at kT ≈ 0.65 keV. This model with two solar-abundance MEKAL components was found to fit the data fairly well (χ^2_ν=1.07), but allowing the metallicity of the cooler component to vary improved the fit (χ^2_ν=1.02). An F-test shows that this improvement is extremely significant, with an F-test statistic of 90.4 and probability P=9.3×10^{-21}. The X-ray luminosity of this residual component is measured to be 1.1×10^{38} erg s^{-1}. W07 notes that strongly sub-solar metallicities are often produced as an artifact of fitting low-resolution spectra, but in this case the reduced abundance is required to correct a significant soft excess in the residual galaxy spectrum. The requirement here for sub-solar abundance hints that a similar component may compensate for the soft excess found previously in M51 and M83, although in those cases the spectral resolution was insufficient to adequately constrain the metallicity.

These spectral fits are consistent with previous results derived for normal and starburst galaxies (*e.g.* Fraternali et al. 2002). It should be noted that as for the previous sample of galaxies, no intrinsic absorption was required to fit the components. As M33 has moderately face-on inclination, a large absorption col-

Table 5.4: Parameters of the best-fitting models to the spectra of the bright-source and residual-galaxy regions.

Observation	Region	Intrinsic N_H	Power-law	Disc BB	Cool MEKAL	Hot MEKAL	Goodness	Cool:Hot
		cm^{-2}	Index	keV	keV	keV	of Fit	Flux Ratio
			Normalization	Normalization	Normalization	Normalization	χ^2/dof	(0.3–2 keV)
0102640101	Bright Sources	6.9×10^{20}	2.13±0.15	1.11±0.07	-	-	676/703	-
			2.30×10^{-3}	0.331				
0102642301	Bright Sources	8.3×10^{20}	2.13±0.14	1.07±0.05	-	-	720/723	-
			3.02×10^{-3}	0.266				
0141980801	Bright Sources	8.5×10^{20}	2.09±0.13	0.93±0.18	-	-	709/672	-
			3.45×10^{-3}	0.242				
Combined	Residual Galaxy	-	-	-	0.19±0.02[a]	0.66±0.04	1292/1265	6.3
					5.93×10^{-3}	8.04×10^{-5}		

[a] - Cool component in residual emission at 9.3% solar abundance.

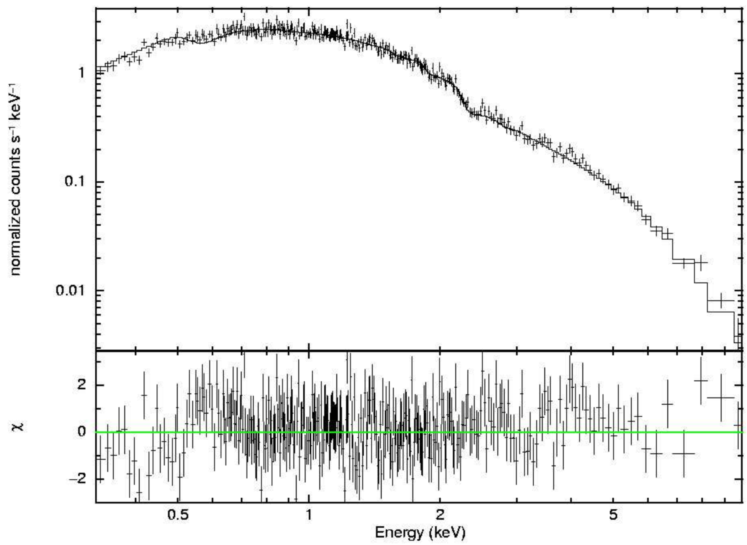

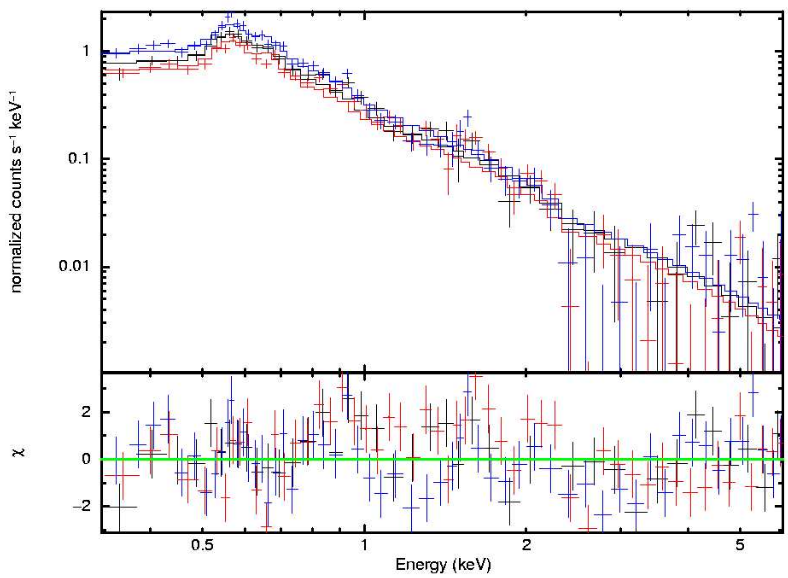

Figure 5.2: The EPIC spectra for M33. *Upper panel:* The spectrum of the bright-source regions from one observation. *Lower panel:* The simultaneously fitted spectra of the residual-galaxy region. In all cases the solid line corresponds to the best-fit spectral model (see text). The χ^2 residuals with respect to the best-fitting model are also shown.

Table 5.5: Physical properties of the diffuse gas present in each galaxy.

Galaxy	Radius[a] kpc	Component (keV)	Electron Density $10^{-3}\eta^{-1/2}$ cm^{-3}	Thermal Energy $10^{54}\eta^{1/2}erg$	Cooling Timescale $10^{8}\eta^{1/2}$ yr
M33	3.5	0.2	1.8	1.9	10.8
		0.65	0.85	2.9	61.0

[a] - Assumed radius of a putative shallow halo component (see text)

umn within the galaxy is not expected. The relative contribution of the two thermal components in the 0.3–2 keV band is measured to be 6.3:1, with the cool component dominant. M33 is therefore spectrally similar to M74, M101 and NGC3184, as opposed to M51 and M83, where the balance between the two components is more even.

We can infer physical properties of the diffuse gas from the spectral fits. If we assume that the majority of the residual emission we observe is truly diffuse and is constrained in a disk of major-axis radius $15'$ (corresponding to 3.5kpc, approximately the extent of the residual emission) and half-width 0.5kpc, we can estimate the electron density, thermal energy contained and cooling timescale for each of the two components. These are given in Table 5.5. The thermal energy contained in the two components is comparable, implying that they are in approximate pressure balance.

5.5 The connection between soft X-ray emission and star-formation

The strength of the spatial correlation between soft X-ray emission and FUV emission, as noted from comparison of the relevant images, confirms the close relationship between soft X-ray emission and recent star formation activity in late-type spiral galaxies. In the earlier study of M101 (W07), point-by-point correlation analysis of soft X-ray surface brightness with that observed in a range of different wavebands was undertaken, which revealed the best correlation to be with U-band data. This was interpreted in terms of two spatial components, a thin-disk component tracing the spiral arms of the galaxy as well as a more extended component with larger filling factor, which contributed mainly to the central concentration of the soft X-ray emission. Our subsequent survey of that galaxy and five other late-type spiral galaxies (Chapter 3) focused on the relationship between X-ray emission and FUV emission in terms of radially-averaged spatial profiles, aiming to quantify the relationship between diffuse X-ray emission and star formation rate (SFR) in a range of systems. Here we follow the methods of the latter paper to incorporate M33 into the sample, again using FUV radial profiles from Muñoz-Mateos et al. (2007). We also consider the relationship between soft X-ray surface brightness and mass density profiles derived from K-band emission (also from Muñoz-Mateos et al. 2007).

As M33 is of intermediate inclination with a major/minor axis ratio of 1.7, we use elliptical annuli centred on the galactic nucleus to extract the X-ray radial profiles, in preference to the circular annuli used in Chapter 3. Due to the presence of the ULX near the galactic nucleus, we extract data from a major-axis radius of $2'$ out to $14'$, where the soft X-ray emission falls to near the background level. This corresponds to a major-axis radius of 0.5–3.5kpc.

Comparison of the X-ray and FUV radial profiles (Fig. 5.3, top panel) shows that radial fall-off in the soft X-ray band is comparable to that observed in the FUV band. This agrees with the inner disk radial profiles observed in all other galaxies in our sample. As our process of image construction for M33 involves an artificial flattening of the surface brightness level at the edges of the D_{25} region of the galaxy to account for different background levels between observations, we are unable to comment quantitatively on the relationship between soft X-ray and FUV radial profiles for the outer disk region. However, visual inspection of the images shows a marked decrease in X-ray surface brightness outside the region used for analysis. This fall-off is consistent with those observed in the outer disk regions of NGC300, M74, M51 and M101. Comparison of the soft X-ray luminosity (per unit disk area) to SFR (per unit disk area) gives a ratio of 1×10^{39} erg s^{-1} (M$_{\odot}$ yr^{-1})$^{-1}$ (Fig. 5.3, second panel), which is flat across the inner disk of the galaxy. There is no evidence for a decline in X-ray/SFR ratio with galactocentric radius. This derived value is consistent with the values for M51, M83 and M101, but is significantly higher than for NGC300 and M74. Analysis of the hardness ratio between the 0.3–0.8 keV and 0.8–1.2 keV bands (Fig. 5.3, bottom panel) is used to track how the relative contribution of the two thermal spectral components varies with galactocentric radius. We find a hint of spectral softening with increased radius, indicating that the hotter component is stronger towards the centre of the galaxy.

Muñoz-Mateos et al. (2007) use K-band data to evaluate the mass radial profile of M33, and use this to calculate specific star formation rates (sSFR) as a function of radius. We divide our calculated SFR across the inner disk by the measurement of the equivalent sSFR at each point to produce an estimate of the mass density, which we then compare to the soft X-ray luminosity (Fig. 5.3, third panel). By this method, we estimate the soft X-ray/mass ratio to be $\approx 4 \times 10^{28}$ erg s^{-1} M$_\odot$$^{-1}$, which is consistent across the inner disk of M33.

5.6 Discussion

The major objective of our study has been to compare the soft X-ray emission observed in the inner disk of M33 with that observed in the galactic disks studied in Chapter 3, particularly with reference to star formation activity. We find that the ratio of soft X-ray emission to SFR (see Fig. 5.3) is $\approx 1 \times 10^{39}$ erg s^{-1} (M$_\odot$ yr^{-1})$^{-1}$ after exclusion of X-ray point sources with L$_X$> 2×10^{35} erg s^{-1}. As this detection level is significantly more sensitive than for the other galaxies in the sample, the M33 XLF from Grimm et al. (2005) was used to scale this result to estimate the observed ratio to a detection limit (in the 0.3-6 keV band) of L$_X$= 1×10^{37} erg s^{-1}. After scaling the X-ray luminosity to the 0.3-2 keV band using the residual emission spectral model, the final ratio was plotted against SFR density, as shown in Fig. 5.4. For direct comparison with Mas-Hesse et al. (2008), which uses a more restrictive SFR band than Muñoz-Mateos et al. (2007), we use the conversion SFR(2-120 M$_\odot$)/ SFR(0.1-100 M$_\odot$) $= 0.293$. This gives us an X-ray/SFR ratio of $\approx 4 \times 10^{39}$ erg s^{-1} (M$_\odot$ yr^{-1})$^{-1}$. The soft X-ray to SFR calibration of Ranalli et al. (2003) derives this value (in the 0.3-2 keV band) to be $10 - 14 \times 10^{39}$ erg s^{-1}, approximately a factor of three higher than our value. This difference is explained by the fact that Ranalli et al. (2003) use the soft X-ray luminosity from the entire galaxy, including a large contribution from the bright point source population, whereas we remove this component.

The results for M33 lie towards the upper end of the range derived for the other galaxies in our sample, with similar results to M51 and M83. This is consistent with the focus of our study being the inner disk, where the SFR density is highest. Across the sample, we have shown clear evidence for a fall-off in X-ray/SFR ratio towards the edge of the disk, and visual inspection of the images in Fig. 5.1 suggests that this is true for M33 as well. The extent of the star-forming disk in M33, as derived from Hα data by Kennicutt (1989), is 7 kpc, extending twice as far out as the observed X-ray emission.

Recent studies conducted by Revnivtsev et al. (2007) and Revnivtsev et al. (2007) have explored the relationship between unresolved X-ray emission and stellar mass distributions for the Galactic ridge and M32, in an attempt to derive the X-ray emissivity per unit stellar mass in systems with low SFR. This emission appears to be almost evenly split between point sources with L$_X$between 10^{31}

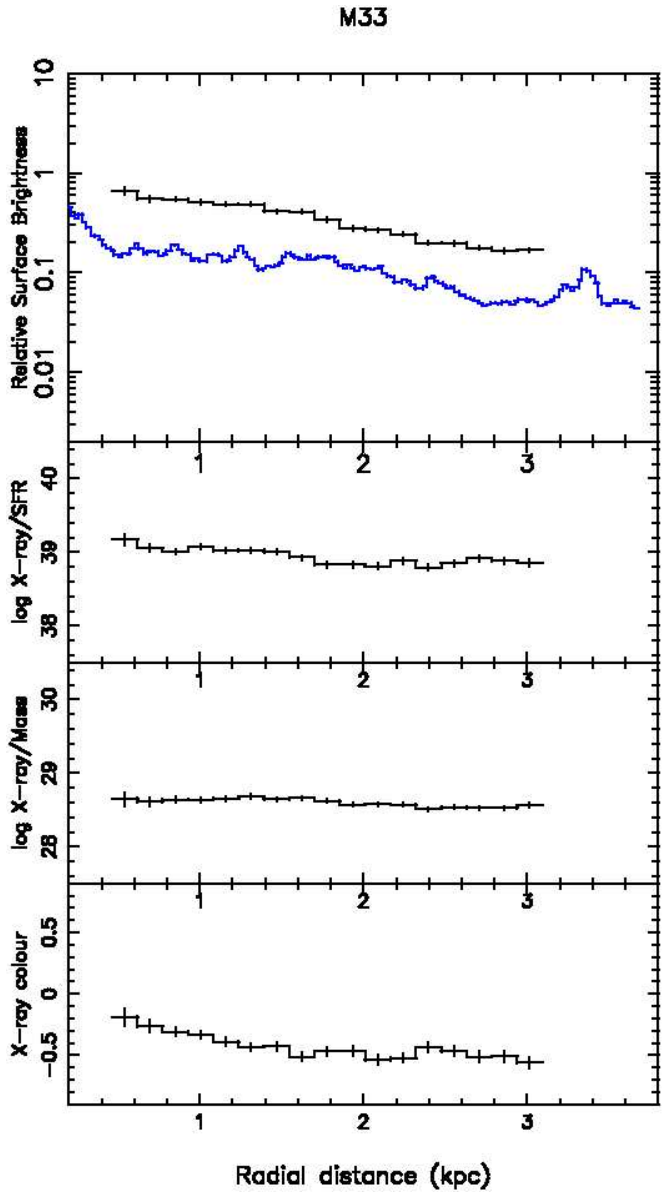

Figure 5.3: A comparison of the radial profile of X-ray emission with FUV emission, SFR and mass distributions in the central disk of M33. The x-axis refers to the major-axis radius scaled to kpc, assuming the distance to M33 is 795kpc. The following information is provided: *Top panel:* The soft X-ray surface brightness versus radius (upper curve). The radial profile of the FUV emission after correction for internal extinction - taken from Muñoz-Mateos et al. (2007) (lower curve). *Second panel:* The ratio of the soft X-ray luminosity in $\mathrm{erg\,s^{-1}}$ pc^{-2} (0.3-1 keV) to the local SFR in units of $\mathrm{M_\odot}$ yr^{-1} pc^{-2}. *Third panel:* The ratio of the soft X-ray luminosity in $\mathrm{erg\,s^{-1}}$ pc^{-2} (0.3-1 keV) to the K-band derived mass in units of $\mathrm{M_\odot}$ pc^{-2}. *Bottom panel:* Variation in X-ray spectral hardness, (H-S)/(H+S), versus radius, where H refers to the 0.8–1.2 keV band and S to the 0.3–0.8 keV band.

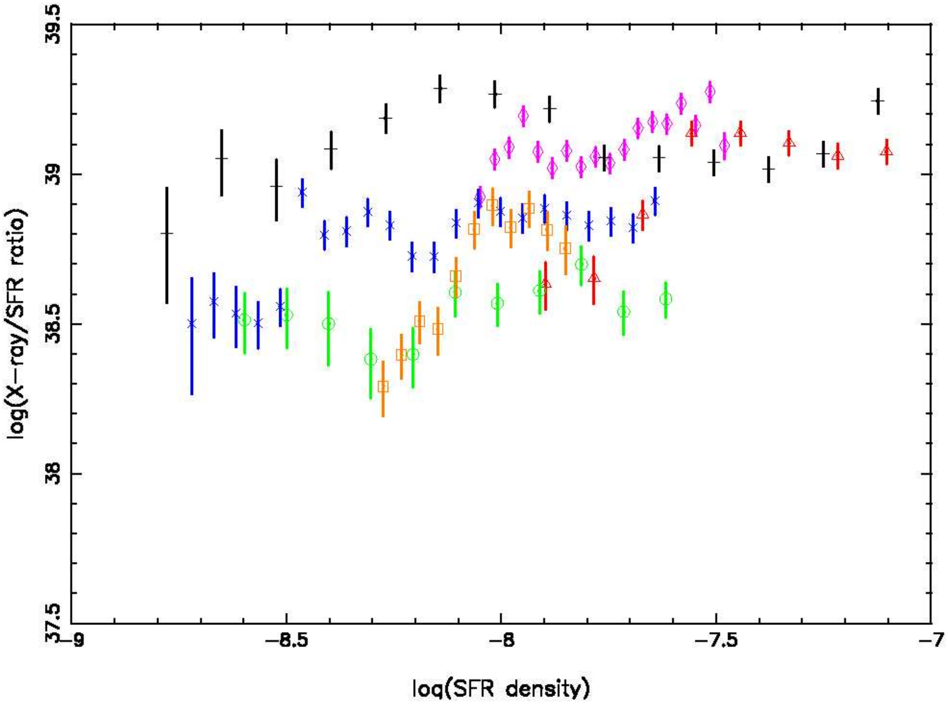

Figure 5.4: The ratio of the soft X-ray luminosity in units of $\mathrm{erg\,s^{-1}}$ $\mathrm{pc^{-2}}$ (0.3–2 keV) to the local SFR density in units of $\mathrm{M_\odot}$ $\mathrm{yr^{-1}}$ $\mathrm{pc^{-2}}$. The data points correspond to NGC300 (orange squares), M74 (green circles), M51 (red triangles), M83 (black points), M101 (blue crosses) and M33 (pink diamonds).

and 10^{34} $\mathrm{erg\,s^{-1}}$, which consist of Active Binaries (AB) and Cataclysmic Variables (CV), and point sources fainter than this, the bulk of which are coronally active stars. Studies of the Galaxy by Sazonov et al. (2006) have derived the XLF for sources to a limiting luminosity of $\mathrm{L_X}$= 10^{27} $\mathrm{erg\,s^{-1}}$, concluding that the soft-band contribution of CVs and ABs to the X-ray luminosity of the galactic disk is $\approx 3\%$ of the contribution of LMXBs in the hard (2–10 keV) band. Revnivtsev et al. (2007) predict that in the soft band, the contribution of these sources may be substantially more, due to their relatively soft spectra. In M33, the population of X-ray sources is highly skewed towards younger sources associated with recent star formation, with a marked deficit in the population of LMXBs observed (Grimm et al. 2005). From the classification of the point source population in this study, along with the observed XLFs of old population sources in the Galaxy, we estimate the contribution from ABs and CVs to the unresolved soft X-ray emission to be $\mathrm{L_X}\approx 1\times10^{37}$ $\mathrm{erg\,s^{-1}}$, or approximately 10% of the observed soft X-ray emission. The remainder of the observed residual emission can be attributed to the combination of faint point sources from the young population of HMXBs, ABs and SNRs as well as truly diffuse X-ray emitting gas. Through extension of the XLF for HMXBs with the same index, we estimate the point source X-ray luminosity (0.3-2 keV) for young sources between 10^{31} and 2×10^{35} erg s^{-1} to be 4×10^{37} erg s^{-1}. This implies that $\approx 5 \times 10^{37}$ erg s^{-1}, or 50% of the observed residual emission is truly diffuse.

The aforementioned studies of the Galactic ridge and M32, along with studies of NGC3379 and M31 (Revnivtsev et al. 2008; Bogdán & Gilfanov 2008), derive an X-ray to stellar mass ratio for quiescent systems (which do not contain substantial hot gas) of $4 - 8 \times 10^{27}$ erg s^{-1} M$_\odot{}^{-1}$ (0.5-2 keV), with the majority of this attributed to the contribution of faint point sources. We estimate the equivalent ratio for M33 to be 4×10^{28} erg s^{-1} M$_\odot{}^{-1}$ in the same band, a factor of 5-10 higher than the range derived for elliptical galaxies and spiral galaxies with limited star formation. This implies that $\approx 10 - 20\%$ of the observed unresolved X-ray luminosity originates in the old faint point-source population, a level consistent with that predicted from the old population XLF.

Spectral analysis of the residual X-ray emission in the inner disk of M33, after removal of the majority of the HMXB/LMXB population, shows a two-temperature thermal model to adequately fit the data, with a strongly subsolar abundance "cool" component at 0.2 keV and a (unconstrained abundance) "hotter" component at 0.65 keV. The subsolar metallicity detected here is in line with studies of HII regions in M33 (Crockett et al. 2006), which report O/H abundances a factor of 2-3 below solar metallicity. These temperatures are consistent with published results for spiral and starburst galaxies (*e.g.,* OW09; Ehle et al. 1998; Soria & Wu 2003; Kuntz et al. 2003). In our previous study, we measured the relative flux contained within the two thermal components. For M51 and M83 there is approximate equality between the flux contained in each component, whereas for the rest of the sample the soft component dominates. In M33, the soft component dominates with a 6.3:1 ratio. In our previous study we suggested that the galaxies with the highest X-ray/SFR ratio were characterised by a higher "mean" temperature. The high ratio in this case, combined with the relatively cool temperature of the residual emission, suggests that temperature alone is not a determining factor in the strength of X-ray emission observed.

Using the models of Mas-Hesse et al. (2008) in the same way as in Chapter 3, the observed X-ray/SFR ratio is consistent with X-ray production 10 Myr after a burst of extended star formation, if the efficiency of conversion of mechanical energy from supernovae into X-ray emission is 1%. Studies of the star formation history of M33 (Wilson et al. 1988; Wilson & Matthews 1995) have shown that several strongly emitting HII regions have undergone bursts of star formation on the timescale of 10 Myr, which indicates that this model is realistic.

The strong correlation observed between X-ray and FUV emission in Fig. 5.1 confirms the linkage between star formation and X-ray emission. As detailed in Chapter 3, we expect FUV emission to arise on the timescale of the lifetime of the most massive stars ($\sim 3 \times 10^6$ years) whereas according to model predictions (Mas-Hesse et al. 2008; Cerviño et al. 2002) the diffuse X-ray signal should reach a maximum after $\sim 3 \times 10^7$ years. Therefore, we should expect to see a rotational lag between the FUV and X-ray emission observed caused by the rotation of M33. Using the rotation curves derived by Corbelli & Salucci (2000), at a galactocentric radius of 2 kpc we would expect to observe a lag of $\approx 26^\circ$ after 10^7 years. No evidence for such a lag is observed in M33, and similar results have been shown for a number of spiral galaxies (Tyler et al. 2004; W07). If the filling factor of the gas $\eta \approx 1$, with the gas enclosed in a cylindrical region with radius 3.5 kpc and half-width 0.5 kpc, the cooling timescale of the dominant cool thermal component of the residual emission is derived to be $\approx 10^9$ yr (Table 5.5) (we assume that 50% of the observed emission can be attributed to faint point sources, as shown above). This cooling timescale is comparable to the rotational period of the galaxy, which is precluded by our observation of narrow spiral features in the X-ray image. The implication of this is, as for the other galaxies in our sample, a clumpy thin-disk distribution best fits the emission observed, consisting of bubbles of hot gas and outflows into the galactic halo. Collections of faint sources, including SNRs, ABs and active coronal stars also contribute to this emission.

5.7 Conclusions

We have used archival *XMM-Newton* observations to examine the residual X-ray emission from M33 after excision of the bright point source population to a limit of $L_X > 2 \times 10^{35}$ erg s^{-1}. Using the same methodology as in Chapter 3, we have investigated the spatial and spectral properties of X-ray emission in the inner galactic disk. The strong correlation between X-ray and FUV emission found confirms the close linkage between X-ray emission and recent star formation.

Detailed comparison of soft X-ray and FUV radial profiles of the inner disk of M33 reveals the ratio of X-ray emission to SFR to be $\approx 4 \times 10^{39}$ erg s^{-1} (M$_\odot$ yr^{-1})$^{-1}$ (in the 0.3-2 keV band, where the SFR refers to stars in the mass range 2–120 M$_\odot$). This is calculated with bright point sources removed to a luminosity of 10^{37} erg s^{-1} (0.3-6 keV), so as to be consistent with the rest of the galaxy sample.

This ratio is approximately a factor of three below the soft X-ray to SFR calibration derived by Ranalli et al. (2003), which is consistent with our removal of the bright point source population. It matches the predictions of Mas-Hesse et al. (2008) for an extended burst of star formation occurring 10 Myr ago, with an efficiency of mechanical energy conversion to X-rays of $\sim 1\%$. Comparison of the soft X-ray emission to mass ratio across the inner disk of M33 finds a ratio of 4×10^{28} erg s^{-1} M$_{\odot}{}^{-1}$, a factor of 5-10 higher than the corresponding ratio for elliptical galaxies and spiral galaxies with low SFR. The excess X-ray emission is split between the faint population young point sources and truly diffuse emission, with the young point source population and diffuse emission closely tracing the spiral arms of the galaxy. There is a small contribution from ABs and CVs in the old point source population, which we expect to be distributed evenly across the disk.

Spectral analysis of the residual emission finds a two-component thermal model to fit the data well, with derived temperatures of ≈ 0.2 keV and ≈ 0.65 keV. The cooler component is dominant in this fit, and is detected with strongly subsolar metallicity, consistent with the subsolar O/H metallicity found in previous studies of this system. The narrow spiral features observed in the soft X-ray emission, in conjunction with the modelled cooling timescales of the gas, show further that the gas in the inner disk of M33, as in the rest of the galaxies in our sample, is likely to follow a clumpy thin-disk distribution, delineated with hot bubbles of gas and collections of faint sources such as active coronal stars and faint SNRs.

Chapter 6

Conclusions and Further Work

In this thesis, we have studied the extended X-ray emission observed in the disks of a sample of nearby face-on spiral galaxies. Our primary goals were to investigate the spatial and spectral properties of this unresolved emission and its connection to star formation in spiral galaxy disks. We were also interested in studying the properties and luminosity function of the global bright X-ray point source population, to better estimate the division of the unresolved emission between faint point sources and diffuse X-ray emitting gas.

6.1 Conclusions

We find evidence for the presence of substantial X-ray emission from diffuse gas in a sample of seven nearby face-on spiral galaxies, using *XMM-Newton* archival observations. This gas traces the spiral arms of the galaxy and is shown to be connected to recent star formation. Using a novel technique to remove the bulk of the contamination due to the bright point source population in each galaxy, we have isolated a residual disk component, comprising truly diffuse emission plus the integrated emission of unresolved point sources. We have derived a quantitative relationship between this unresolved X-ray emission and the star formation rate, which is consistent with physical starburst models.

In Chapter 3, we found a strong correlation between soft X-ray emission and FUV emission in a sample of six nearby face-on spiral galaxies, unambiguously establishing a linkage between X-ray emission and recent star formation. Comparison of the bright point source population observed in these galaxies with the profile of the XLF measured for spiral galaxies in general suggests that the majority of the observed unresolvedemission is from diffuse gas. Comparison of the radial profiles of X-ray and FUV surface brightness, after removal of bright point sources with $L_X > 10^{37}\ \mathrm{erg\ s^{-1}}$ (0.3-6 keV), establishes the X-ray/SFR ratio in the range $1-5\times10^{39}\ \mathrm{erg\ s^{-1}}$ ($M_\odot$ yr^{-1})$^{-1}$. This ratio was highest in the inner disks of M51 and M83, which out of the regions studied were those with the highest SFR. Study of the inner disk of M33 (Chapter 5) shows the X-ray/SFR ratio to be towards the upper end of this range, consistent with the relatively high SFR density in this system. Comparison with the models of Ranalli et al. (2003) shows our ratio to be a factor of three lower, consistent with their inclusion of the bright point source population we exclude. It also matches the predicted X-ray emission observed 10 Myr after an extended burst of star formation, assuming 1% of the total energy is converted into X-rays. As local SFR density declines, we observe a fall-off in the X-ray/SFR ratio, which implies a connection between the interstellar environment and the efficiency of energy conversion from the starburst into X-rays.

The addition of M33 to our sample in Chapter 5 allowed exploration of the unresolved X-ray emission in greater detail. The relative proximity of the galaxy (compared to the other systems studied) make it possible to exclude point sources to a threshold luminosity of $L_X = 2\times10^{35}\ \mathrm{erg\ s^{-1}}$. From previous studies of the optical counterparts to these sources, this population is shown to contain very few LMXBs and consists primarily of young objects. The XLF for sources in this galaxy was therefore extremely well defined, allowing an estimate to be made of the contribution of faint point sources to the unresolved emission. We show that $\approx 50\%$ of the unresolved emission in the disk is attributable to diffuse gas, with the remainder dominated by point sources from the young stellar population. For this system, we also examined the relationship between the unresolved X-ray emission and the mass profile of the galaxy (derived from K-band data). We find this ratio to be $4\times10^{28}\ \mathrm{erg\ s^{-1}}\ {M_\odot}^{-1}$, which is a factor of 5-10 higher than the corresponding ratio found in elliptical galaxies lacking hot gas. This suggests that $\approx$ $10-20\%$ of the unresolved X-ray emission in this galaxy is attributable to faint point sources in the old stellar population. As the population of discrete point sources in M33 is dominated by young objects, which is not necessarily the case in the other galaxies in our sample, the relative contributions of the point source and diffuse components to the observed residual emission may vary significantly between galaxies. In order to constrain these contributions, the balance between old and young populations in these galaxies (from identification of optical counterparts) must be known in more detail. Our study of the bright point source populations in each galaxy in our sample (Chapter 4) suggests that there is a comparable contribution from old and young populations overall, although the relatively low number of sources does not allow robust quantitative analysis for each system individually.

Spectral analysis shows the unresolved emission in the galaxy disks to be well fit by a two-temperature thermal plasma model, with characteristic temperatures of ≈ 0.2 keV and ≈ 0.65 keV. This is consistent with previous results for spiral and starburst galaxies. The mean temperature of the plasma, as determined from the relative contributions of the two thermal components, is significantly higher in M51 and M83, the two galaxies in our sample which exhibit violent starbursts. There is little evidence of a radial dependence in the gas temperature in any of the galaxies studied. The metallicities of the spectral fits were unconstrained in all cases except for M33, which required a thermal fit with strongly subsolar abundance. We suggest this may be linked to the observed deficit of LMXBs observed in the galaxy. The unresolved X-ray emission in all galaxies in our sample was found to be consistent with a clumpy thin-disk distribution, with bubbles of hot gas and collections of faint SNRs and young sources tracing the spiral arms of the galaxy. This model predicts the relatively narrow spiral features observed in X-rays which are coincident with the spiral arms.

In Chapter 4, we studied the X-ray colours and luminosity function of the bright point source populations in each of the galaxies in our original sample, using a source classification scheme derived by Prestwich et al. (2003). We found the cumulative luminosity distribution of sources with luminosities above $L_X = 10^{38}\ \mathrm{erg\ s^{-1}}$ (0.2-12 keV) to be well-fit with a single power-law with an index of -0.73 ± 0.08, in between the gradients derived for high luminosity LMXB and HMXB sources in a range of galaxies. The sources classified as candidate SNRs were found to be predominantly associated with spiral arm regions, indicating that most of the remnants in our survey originate from type-II supernova explosions than type-Ia events. The distribution of X-ray binary sources across the disk suggests a comparable number of HMXBs and LMXBs are present, with the high luminosity population skewed slightly in favour of LMXBs. Our analysis indicates that old and young stellar populations contribute comparably to the bright point source X-ray emission observed from our sample of galaxies.

6.2 Future Work

The work presented here is an extension of the study conducted by Ranalli et al. (2003) into the connection between both soft and hard X-ray emission and star formation in galaxies, without exclusion of point sources. This allows distant systems to be studied, for which it is not possible to spatially distinguish the different X-ray components in the galaxy. A problem which arises, however, is that the X-ray luminosities observed in this way are strongly influenced by the few brightest discrete sources in the target galaxy. These sources contribute a comparable luminosity to our residual disk component in the soft band (0.5–2 keV), whilst completely dominating emission in the hard band (2–10 keV). Our removal of the brightest point sources circumvents this problem somewhat, as it allows us to estimate the XLF of the sources in the galaxy and account for their contribution to the unresolved emission to relatively low luminosity. As we have found the spectral components of the residual emission in our sample of galaxies to be consistent between galaxies, it should be possible to fit a set thermal spectrum (with varying normalisation) along with a simple combined source model to the emission from more distant systems. With sufficient spectral resolution, the contribution of the different components to this fit can be evaluated, allowing a rudimentary estimate of the relationship between residual emission and star formation to be made.

In the present work, we have demonstrated a quantifiable link between soft X-ray emission and star formation rate in a sample of nearby galaxies. However, there is only a small sample of face-on spiral galaxies which are currently in the *XMM-Newton* archive with sufficient exposure to allow measurement of the diffuse signal with good signal-to-noise. For example, the 20ks observations used for analysis of M74 and NGC3184 are barely sufficient to constrain the amount of unresolved emission observed. On the other hand, analysis of the UV radial properties and SFR of nearby galaxies using GALEX has been completed for the majority of spiral galaxies within 20 Mpc. There are several moderate inclination normal spiral galaxies within 10Mpc which have little or no *XMM-Newton* observational time, spanning a range of Hubble types from Sb-Sd and large enough in extent to be deserving of study. These include NGC2403, NGC2903, NGC3344 and NGC7793. For these systems, a 50ks observation will be sufficient to identify and remove point sources to a limit of $\approx 2 \times 10^{37}$ erg s^{-1}. It is certainly true that the larger the number of systems observed, the better we will be able to constrain the relationship between soft X-ray emission and SFR.

Our use of “blank-sky” fields in background subtraction for M33 has been shown to be robust. These methods can be used for study of other nearby systems, such as regions of M31 and the Magellanic Clouds. Study of such systems, where the XLF is well defined to low luminosity, will allow estimation of the faint point source contribution to the unresolved emission with far greater accuracy than is currently possible for the majority of our sample.

We have shown the ability to effectively remove the influence of the brightest point sources in the galaxies we have studied, despite the moderate spatial resolution afforded by *XMM-Newton* . Application of similar techniques to *Chandra* data should be able to achieve this to even greater effect. The major problem with this is the difference in collecting area. A significantly longer exposure with *Chandra* is necessary to achieve the same signal as a corresponding *XMM-Newton* exposure.

One physical aspect of the residual X-ray emission which it has proven difficult to study for our sample is the metallicity of the thermal components in the spectral fits, which have been unconstrained in the majority of cases. Only for M33 have we found a thermal fit which requires strongly subsolar abundances. The relationship between the metal abundances in galaxies and the amount and temperature of X-ray emitting gas present is a subject which merits further study. With current X-ray observatories it is only possible to investigate this for relatively nearby systems. With the advent of the next generation of X-ray observatories such as IXO, with arcsecond spatial resolution, spectral resolution comparable to *XMM-Newton* and collecting area 20 times greater, it should be possible to explore the relationship between soft X-ray emission and star formation over a wide range of astrophysical settings.

Appendix A

Bright X-ray point source catalogue

The following tables provide details of the bright point sources which comprise the "master source catalogue" of each galaxy studied in Chapter 3.

Table A.1: Bright X-ray sources detected within 5’ of the nucleus of NGC300.

Src	XMMU	$r_{1\sigma}$	pn count rate (count ks^{-1})			MOS count rate (count ks^{-1})			F_X	L_X
		($''$)	S	M	H	S	M	H		
(1)	(2)	(3)	(4)			(5)			(6)	(7)
1	J005437.6-374249	0.98	**1.2±0.2**	0.6±0.2	0.7±0.2	0.3±0.1	**0.4±0.1**	0.3±0.1	0.82±0.10	0.40±0.05
2	J005440.7-374048	0.56	**16.5±0.7**	**2.3±0.3**	0.1±0.1	**4.6±0.2**	**1.3±0.1**	0.1±0.1	2.92±0.22	1.40±0.11
3	J005442.5-373733	0.69	**3.4±0.4**	**1.8±0.3**	**1.0±0.2**	**0.9±0.1**	**0.7±0.1**	**0.4±0.1**	1.58±0.14	0.76±0.07
4	J005442.5-374342	0.65	**3.0±0.3**	**2.1±0.3**	**1.4±0.2**	**0.4±0.1**	**1.1±0.1**	**0.7±0.1**	1.95±0.14	0.93±0.07
5	J005444.4-374115	0.81	**2.3±0.3**	0.7±0.2	0.2±0.1	**0.7±0.1**	0.2±0.1	-	0.58±0.10	0.28±0.05
6	J005445.2-374146	0.51	**10.3±0.6**	**1.4±0.2**	-	**2.4±0.2**	**0.8±0.1**	-	1.65±0.17	0.79±0.08
7	J005449.7-374000	0.68	**1.8±0.3**	**1.7±0.2**	**1.1±0.2**	**0.4±0.1**	**0.7±0.1**	**0.4±0.1**	1.35±0.12	0.65±0.06
8	J005450.3-373849	0.41	**7.6±0.5**	**14.0±0.7**	**10.1±0.6**	**2.1±0.2**	**6.1±0.3**	**4.9±0.3**	12.36±0.30	5.91±0.14
9	J005450.6-374128	0.84	**2.5±0.3**	0.7±0.2	0.2±0.1	**0.7±0.1**	0.3±0.1	0.1±0.1	0.63±0.10	0.30±0.05
10	J005453.2-374127	1.14	0.5±0.2	**1.1±0.2**	0.5±0.2	0.1±0.1	0.1±0.1	0.2±0.1	0.58±0.08	0.28±0.04
11	J005453.4-374310	1.20	**0.9±0.2**	0.2±0.1	0.7±0.2	-	-	0.3±0.1	0.67±0.08	0.32±0.04
12	J005457.2-374311	0.79	**1.8±0.3**	**1.0±0.2**	**1.4±0.2**	0.2±0.1	**0.7±0.1**	**0.4±0.1**	1.41±0.12	0.68±0.06
13	J005503.2-374538	1.96	0.7±0.2	0.6±0.2	0.2±0.2	0.1±0.1	-	-	0.45±0.09	0.22±0.04
14	J005505.7-374119	1.57	**2.0±0.3**	-	0.1±0.1	**0.6±0.1**	0.2±0.1	-	0.38±0.10	0.18±0.05
15	J005507.2-374345	6.73	0.4±0.2	0.4±0.2	0.2±0.1	0.1±0.1	0.1±0.1	0.1±0.1	0.29±0.09	0.14±0.04
16	J005507.6-374420	0.76	0.7±0.2	**1.3±0.2**	**1.7±0.3**	0.2±0.1	**0.4±0.1**	**0.4±0.1**	1.48±0.12	0.71±0.06
17	J005510.0-374212	0.36	**178.3±2.5**	**78.8±1.7**	**28.5±1.0**	**39.0±0.7**	**27.2±0.6**	**10.9±0.4**	59.07±0.84	28.24±0.40
18	J005510.9-373854	0.42	**27.4±1.0**	0.1±0.1	-	**7.4±0.3**	-	0.1±0.1	3.74±0.27	1.79±0.13
19	J005512.2-373823	1.25	1.1±0.3	0.7±0.2	0.5±0.2	0.1±0.1	0.3±0.1	0.1±0.1	0.55±0.10	0.26±0.05
20	J005515.5-374439	0.74	**3.0±0.4**	0.1±0.1	-	**1.9±0.2**	0.2±0.1	-	0.71±0.13	0.34±0.06

(1) source number; (2) 2XMM source designation (J2000 coordinates); (3) 1σ error radius (including a $0.5''$ systematic error); (4 & 5) source count rates in soft (0.3–1 keV), medium (1–2 keV) & hard (2–6 keV) bands for the pn and MOS cameras, with the significant source detections ($> 4\sigma$) highlighted in bold; the MOS count rates are scaled to single camera count-rates; (6) source flux in units of 10^{-14} erg cm^{-2} s^{-1} in the broad (0.3–6 keV) band; (7) source luminosity in units of 10^{37} erg s^{-1} in the 0.3–6 keV band.

Table A.2: Bright X-ray sources detected within the D_{25} circle of M74.

Src	XMMU	$r_{1\sigma}$	pn count rate (count ks^{-1})			MOS count rate (count ks^{-1})			F_X	L_X
		($''$)	S	M	H	S	M	H		
(1)	(2)	(3)		(4)			(5)		(6)	(7)
1	J013624.3+154214	0.63	**4.4±0.6**	**2.9±0.5**	**2.5±0.5**	0.6±0.2	**1.4±0.2**	0.8±0.2	2.57±0.26	2.89±0.29
2	J013627.2+155007	0.68	**6.4±0.7**	**4.5±0.6**	**3.5±0.5**	**2.4±0.7**	**2.6±0.3**	**1.8±0.2**	4.70±0.32	5.26±0.36
3	J013629.8+155728	1.60	**1.7±0.4**	**2.2±0.4**	**1.9±0.4**	0.2±0.1	**0.9±0.2**	0.8±0.2	1.59±0.20	1.78±0.23
4	J013631.2+155239	1.58	1.2±0.5	**1.6±0.4**	0.8±0.4	-	0.3±0.2	0.3±0.1	0.83±0.20	0.93±0.23
5	J013631.8+154848	0.78	**2.9±0.5**	0.2±0.2	0.3±0.3	**1.0±0.2**	0.3±0.1	0.3±0.1	1.06±0.18	1.18±0.21
6	J013635.2+154657	1.87	0.7±0.4	0.6±0.3	1.2±0.4	0.3±0.1	**0.5±0.1**	**0.5±0.1**	0.88±0.19	0.99±0.22
7	J013635.7+154557	1.27	0.1±0.5	0.4±0.2	0.9±0.3	-	0.2±0.1	0.1±0.1	0.34±0.17	0.39±0.19
8	J013636.5+155036	0.43	**3.8±0.7**	1.3±0.4	1.2±0.4	0.5±0.2	0.4±0.2	**0.5±0.1**	1.53±0.24	1.72±0.27
9	J013638.3+153808	1.77	0.6±0.5	0.2±0.3	0.1±0.3	0.3±0.2	0.2±0.1	0.1±0.1	0.31±0.19	0.35±0.21
10	J013638.9+154421	3.28	**7.7±0.7**	**5.1±0.6**	**3.9±0.5**	**1.5±0.2**	**2.0±0.2**	**1.9±0.2**	4.65±0.32	5.21±0.36
11	J013639.2+154311	0.58	2.3±0.6	1.2±0.4	**3.8±0.5**	0.1±0.2	0.2±0.1	**0.9±0.2**	1.65±0.24	1.85±0.27
12	J013639.4+154744	1.05	2.6±0.7	0.3±0.3	0.4±0.4	**0.8±0.2**	0.2±0.2	-	0.91±0.25	1.02±0.28
13	J013639.6+154848	4.87	**4.3±0.7**	**1.6±0.4**	1.9±0.5	**0.9±0.2**	**1.2±0.2**	**1.0±0.2**	2.38±0.28	2.67±0.32
14	J013641.7+154701	1.14	2.3±0.6	**2.6±0.5**	**1.6±0.4**	**0.8±0.2**	**1.3±0.2**	**0.9±0.2**	2.07±0.26	2.32±0.29
15	J013642.0+153436	1.84	0.3±0.4	0.8±0.4	0.4±0.3	0.2±0.1	0.6±0.2	0.2±0.1	0.58±0.20	0.65±0.22
16	J013643.9+154358	1.93	1.9±0.7	0.1±0.3	0.4±0.4	-	-	-	0.75±0.18	0.84±0.20
17	J013644.1+154818	0.96	0.7±0.5	0.3±0.3	0.9±0.4	-	0.2±0.1	0.3±0.1	0.47±0.20	0.53±0.23
18	J013646.1+154120	0.88	-	1.1±0.4	1.0±0.4	-	0.6±0.2	0.4±0.2	0.71±0.17	0.79±0.19
19	J013646.1+154424	1.48	**33.4±1.6**	**4.6±0.6**	**2.6±0.5**	**5.5±0.4**	**2.8±0.3**	0.4±0.1	9.79±0.48	10.97±0.54
20	J013650.9+155331	0.80	**15.6±1.1**	**9.0±0.8**	**6.7±0.8**	**3.4±0.3**	**4.0±0.4**	**2.6±0.3**	8.64±0.47	9.68±0.52

Key: As for Table A.1.

Table A.3: Bright X-ray sources detected within the D_{25} circle of NGC3184.

Src	XMMU	$r_{1\sigma}$	pn count rate (count ks^{-1})			MOS count rate (count ks^{-1})			F_X	L_X
		($''$)	S	M	H	S	M	H		
(1)	(2)	(3)		(4)			(5)		(6)	(7)
1	J101758.5+412602	1.78	1.2±0.5	0.9±0.3	0.2±0.3	0.1±0.1	0.2±0.1	0.2±0.1	0.59±0.20	0.96±0.32
2	J101806.8+412422	1.40	-	0.6±0.3	1.5±0.4	0.1±0.1	0.3±0.1	**0.9±0.2**	0.89±0.18	1.46±0.30
3	J101808.2+412331	1.34	0.4±0.3	0.7±0.3	1.4±0.4	-	0.2±0.1	**1.0±0.2**	0.94±0.18	1.53±0.31
4	J101810.6+412532	2.15	0.8±0.4	-	-	0.2±0.1	-	-	0.26±0.16	0.33±0.21
5	J101812.0+412421	0.55	**8.6±0.8**	**7.8±0.7**	**4.4±0.6**	**2.1±0.3**	**2.9±0.3**	**2.0±0.3**	6.16±0.39	9.98±0.64
6	J101814.0+412332	1.25	**1.6±0.4**	0.8±0.3	0.5±0.3	0.7±0.2	0.2±0.1	**0.4±0.1**	0.98±0.19	1.59±0.30
7	J101815.1+412609	1.91	**2.0±0.5**	1.0±0.3	0.7±0.3	0.6±0.2	**0.5±0.1**	**0.5±0.1**	1.31±0.21	2.12±0.34
8	J101816.7+412629	1.00	**1.9±0.5**	-	0.4±0.3	0.4±0.1	0.2±0.1	0.2±0.1	0.67±0.17	1.09±0.27
9	J101816.8+412529	1.64	**7.2±0.7**	**2.3±0.4**	1.1±0.3	**2.5±0.3**	**1.1±0.2**	**0.9±0.2**	3.61±0.30	5.80±0.48
10	J101817.1+412343	0.76	**5.5±0.6**	**3.1±0.5**	**2.7±0.5**	0.7±0.2	**1.2±0.2**	**1.2±0.2**	3.07±0.28	4.98±0.45
11	J101818.7+412556	0.87	**3.9±0.5**	**2.4±0.4**	**2.1±0.4**	**0.9±0.2**	**0.9±0.2**	**0.7±0.1**	2.31±0.24	3.75±0.39
12	J101821.6+412609	0.74	**3.8±0.5**	**2.3±0.4**	0.5±0.2	**1.5±0.2**	**1.1±0.2**	**1.0±0.2**	2.56±0.25	4.21±0.41
13	J101821.8+412644	6.35	0.6±0.3	0.1±0.2	-	0.1±0.1	-	0.2±0.1	0.25±0.12	0.40±0.20
14	J101822.9+412741	0.53	**8.0±0.7**	**8.3±0.7**	**5.1±0.6**	**1.8±0.2**	**4.0±0.3**	**2.4±0.3**	6.81±0.39	11.04±0.63
15	J101823.0+412512	0.84	**2.3±0.4**	**1.7±0.3**	1.1±0.3	0.8±0.2	**1.2±0.2**	0.1±0.1	1.71±0.21	2.77±0.34
16	J101823.6+412255	1.12	**1.3±0.3**	1.0±0.3	**1.2±0.3**	0.4±0.1	**0.6±0.1**	0.2±0.1	1.03±0.18	1.68±0.29
17	J101830.9+412641	1.15	1.0±0.3	0.7±0.2	0.7±0.3	0.1±0.1	0.3±0.1	**0.8±0.2**	0.88±0.16	1.44±0.26
18	J101833.3+412422	1.11	1.0±0.3	0.9±0.3	0.7±0.3	0.1±0.1	0.1±0.1	0.1±0.1	0.73±0.14	1.19±0.23

Key: As for Table A.1.

Table A.4: Bright X-ray sources detected within the D_{25} circle of M51.

Src	XMMU	$r_{1\sigma}$	pn count rate (count ks^{-1})			MOS count rate (count ks^{-1})			F_X	L_X
		($''$)	S	M	H	S	M	H		
(1)	(2)	(3)		(4)			(5)		(6)	(7)
1	J132938.7+471326	0.79	**7.1±0.7**	**5.6±0.6**	**2.6±0.4**	**2.2±0.2**	**2.3±0.2**	**1.7±0.2**	4.58±0.23	2.84±0.14
2	J132939.7+471239	0.23	**55.9±1.6**	**24.5±1.1**	**9.3±0.7**	**14.0±0.5**	**11.3±0.5**	**4.0±0.3**	19.50±0.47	12.09±0.29
3	J132942.6+471042	1.21	-	0.6±0.3	0.2±0.3	0.3±0.2	**0.5±0.1**	**0.4±0.1**	0.66±0.13	0.41±0.08
4	J132943.5+471136	2.69	2.4±0.7	0.1±0.3	0.1±0.3	**1.1±0.2**	**0.5±0.1**	0.1±0.1	0.64±0.17	0.40±0.11
5	J132944.4+471357	0.86	-	**1.2±0.3**	1.5±0.4	0.2±0.1	**0.5±0.1**	**0.6±0.1**	1.43±0.13	0.89±0.08
6	J132945.5+471012	3.19	**6.9±0.8**	0.9±0.3	0.2±0.2	**1.4±0.2**	**0.5±0.1**	-	1.08±0.19	0.67±0.12
7	J132950.6+471155	0.38	**72.7±1.9**	**9.9±0.7**	**23.2±1.0**	**18.6±0.6**	**5.0±0.3**	**11.3±0.5**	30.09±0.51	18.65±0.31
8	J132951.3+471033	0.96	**7.8±0.8**	**3.0±0.4**	**2.6±0.4**	**1.9±0.2**	**1.5±0.2**	**1.3±0.2**	3.79±0.23	2.35±0.14
9	J132952.6+471144	2.87	**428.5±4.4**	**76.1±1.8**	**10.5±0.7**	**109.1±1.4**	**34.4±0.8**	**3.8±0.3**	76.78±1.06	47.60±0.66
10	J132953.6+471435	0.31	**15.0±1.0**	**15.6±0.9**	**11.7±0.8**	**3.7±0.3**	**5.9±0.4**	**5.0±0.3**	14.19±0.36	8.80±0.22
11	J132953.8+471043	2.13	**14.2±0.9**	**6.7±0.6**	**5.9±0.5**	**3.4±0.3**	**2.9±0.2**	**2.4±0.2**	7.64±0.28	4.74±0.17
12	J132954.1+471300	1.21	**5.2±0.8**	**2.3±0.4**	**3.2±0.4**	**0.9±0.2**	**1.2±0.2**	**1.1±0.2**	3.36±0.22	2.09±0.13
13	J132954.5+470921	0.83	2.2±0.6	**3.2±0.5**	**2.0±0.4**	0.4±0.2	**1.7±0.2**	**0.6±0.1**	2.43±0.18	1.51±0.11
14	J132954.8+471039	2.51	**9.0±0.8**	**2.7±0.4**	**1.7±0.3**	**2.2±0.2**	**1.3±0.2**	**0.6±0.1**	2.90±0.21	1.80±0.13
15	J132955.8+471238	1.98	**7.2±0.9**	1.2±0.4	0.3±0.2	**2.2±0.3**	**0.9±0.2**	0.2±0.1	1.59±0.21	0.99±0.13
16	J132957.2+471356	3.15	**11.5±0.9**	**2.4±0.4**	0.5±0.3	**3.3±0.3**	**0.8±0.2**	0.2±0.1	2.34±0.22	1.45±0.14
17	J132957.6+471049	0.41	**11.9±0.9**	**7.0±0.6**	**2.7±0.4**	**2.9±0.3**	**3.0±0.3**	**1.4±0.2**	5.21±0.27	3.23±0.17
18	J132958.2+471323	1.32	**13.9±1.0**	**4.5±0.5**	**2.9±0.4**	**2.3±0.3**	**2.3±0.2**	**0.9±0.1**	4.49±0.25	2.79±0.15
19	J133000.8+471126	3.86	**2.8±0.7**	0.4±0.3	-	**1.0±0.2**	-	0.1±0.1	0.55±0.17	0.34±0.11
20	J133000.9+471344	0.32	**82.5±2.1**	**69.9±1.9**	**49.4±1.6**	**20.2±0.7**	**28.8±0.8**	**21.7±0.7**	63.65±0.74	39.46±0.46
21	J133001.0+471309	1.30	**18.1±1.1**	**2.3±0.4**	0.9±0.3	**3.9±0.3**	**1.2±0.2**	0.2±0.1	3.18±0.25	1.97±0.16
22	J133004.2+471321	0.69	**8.8±0.9**	**6.0±0.6**	**4.2±0.5**	**2.2±0.3**	**2.1±0.2**	**1.3±0.2**	5.23±0.25	3.24±0.16
23	J133004.7+471417	1.23	0.7±0.5	1.3±0.4	**1.9±0.4**	0.7±0.2	**0.5±0.1**	0.7±0.2	1.88±0.17	1.16±0.11
24	J133007.5+471105	0.15	**51.4±1.6**	**36.9±1.4**	**17.2±1.0**	**12.8±0.5**	**15.3±0.6**	**7.8±0.4**	27.84±0.54	17.26±0.33
25	J133010.9+471043	1.17	**9.7±0.8**	**4.4±0.5**	**2.7±0.4**	**2.2±0.2**	**2.6±0.3**	**1.4±0.2**	4.48±0.24	2.78±0.15

Key: As for Table A.1.

Table A.5: Bright X-ray sources detected within the D_{25} circle of M83.

Src	XMMU	$r_{1\sigma}$	pn count rate (count ks^{-1})			MOS count rate (count ks^{-1})			F_X	L_X
		($''$)	S	M	H	S	M	H		
(1)	(2)	(3)		(4)			(5)		(6)	(7)
1	J133635.9-295120	0.96	1.2±0.6	0.9±0.4	1.3±0.5	0.4±0.2	**0.9±0.2**	**0.9±0.2**	1.08±0.19	0.27±0.05
2	J133639.0-294743	0.74	**9.2±1.0**	**7.0±0.9**	**4.1±0.7**	**2.2±0.3**	**2.9±0.3**	**1.5±0.2**	4.35±0.33	1.05±0.07
3	133643.4-295108	2.00	-	**1.9±0.5**	**1.6±0.5**	0.6±0.2	**3.0±0.3**	**3.0±0.3**	4.91±0.35	1.18±0.09
4	J133644.2-294842	0.59	**16.4±1.3**	**15.5±1.2**	**6.0±0.8**	**3.6±0.3**	**6.0±0.4**	**2.6±0.3**	8.07±0.41	1.95±0.10
5	J133649.2-295258	0.65	**16.4±1.4**	**11.1±1.0**	**2.5±0.5**	**2.9±0.4**	**3.7±0.3**	**1.1±0.2**	5.76±0.37	1.39±0.09
6	J133651.6-295335	1.29	2.6±1.2	0.8±0.5	0.3±0.4	1.1±0.3	0.7±0.2	0.5±0.2	1.16±0.27	0.28±0.07
7	J133651.9-295135	1.91	**7.3±1.0**	1.2±0.4	0.7±0.3	**2.5±0.3**	0.7±0.2	**0.4±0.1**	2.18±0.25	0.53±0.06
8	J133652.4-295256	2.59	**23.6±1.8**	**3.1±0.7**	0.6±0.4	**4.8±0.4**	**0.7±0.2**	-	4.74±0.37	1.14±0.23
9	J133653.6-295110	1.40	**8.2±1.1**	**2.8±0.6**	0.8±0.4	0.9±0.3	**1.0±0.2**	0.1±0.2	1.91±0.25	0.46±0.06
10	J133654.8-295026	4.58	**7.0±1.1**	**2.4±0.6**	0.1±0.3	0.9±0.3	0.3±0.1	0.1±0.1	1.42±0.37	0.34±0.06
11	J133655.5-295509	0.83	-	-	0.5±0.4	0.6±0.2	**1.6±0.2**	**1.6±0.2**	2.90±0.25	0.70±0.06
12	J133656.6-294912	0.86	1.1±0.8	**3.3±0.6**	**2.2±0.5**	0.6±0.2	**1.0±0.2**	**0.9±0.2**	1.55±0.24	0.37±0.06
13	J133657.3-295338	0.69	**7.5±1.2**	**6.8±0.8**	**5.6±0.7**	**2.8±0.3**	**3.0±0.3**	**2.0±0.2**	4.70±0.34	1.44±0.09
14	J133657.5-294913	4.44	**3.2±0.9**	**7.3±0.8**	**5.8±0.8**	**0.9±0.2**	**1.9±0.2**	**1.2±0.2**	3.09±0.29	0.75±0.08
15	J133658.3-294832	0.91	1.3±0.8	**3.2±0.6**	**2.8±0.6**	**1.2±0.3**	**0.8±0.2**	**0.9±0.2**	1.74±0.24	0.41±0.06
16	J133658.3-295104	1.06	0.3±1.0	0.9±0.6	**2.3±0.6**	0.6±0.3	0.4±0.2	**1.0±0.2**	0.99±0.25	0.24±0.06
17	J133659.4-294958	0.55	**18.8±1.5**	**17.7±1.2**	**19.4±1.3**	**4.1±0.4**	**7.2±0.4**	**6.3±0.4**	11.79±0.48	2.84±0.12
18	133659.5-295414	2.00	**3.9±1.0**	**3.0±0.6**	**3.0±0.6**	0.4±0.2	0.2±0.1	0.6±0.2	1.93±0.25	0.47±0.06
19	J133700.5-295341	3.32	1.6±0.9	**2.8±0.6**	**1.7±0.5**	0.0±0.2	**1.1±0.2**	0.5±0.1	1.20±0.24	0.30±0.06
20	J133700.6-295052	1.37	**8.3±1.3**	-	-	**1.1±0.3**	-	-	1.24±0.24	0.30±0.06
21	J133700.6-295158	2.90	**453.9±5.8**	**197.2±3.8**	**55.3±2.0**	**90.9±1.5**	**57.3±1.2**	**18.5±0.7**	130.91±1.43	31.58±0.34
22	J133701.4-295324	0.61	**18.2±1.4**	**33.7±1.7**	**17.8±1.2**	**1.9±0.3**	**9.9±0.5**	**6.3±0.4**	13.44±0.50	3.24±0.12
23	J133701.5-294742	0.69	1.7±0.7	**7.4±0.9**	**4.9±0.7**	0.7±0.2	**3.1±0.3**	**2.3±0.3**	3.48±0.29	0.84±0.08
24	J133702.1-295517	0.75	**5.0±0.9**	**5.6±0.8**	**5.5±0.8**	**1.0±0.2**	**1.1±0.2**	**1.7±0.2**	2.98±0.27	0.73±0.07
25	J133703.8-294929	0.76	**11.6±1.3**	**6.3±0.8**	**4.3±0.7**	**1.9±0.3**	**2.6±0.3**	**1.8±0.2**	4.73±0.33	1.08±0.09
26	J133704.3-295402	0.63	**14.7±1.3**	**16.4±1.2**	**6.1±0.8**	**2.8±0.3**	**4.9±0.4**	**1.2±0.2**	6.94±0.38	1.67±0.10
27	J133704.3-295120	0.56	**24.7±1.8**	**33.2±1.7**	**13.3±1.1**	**4.4±0.4**	**10.5±0.5**	**5.0±0.4**	14.19±0.53	3.42±0.13
28	J133705.2-295226	0.74	**11.2±1.2**	**10.4±1.0**	**6.3±0.8**	**2.1±0.3**	**2.2±0.3**	**1.4±0.2**	4.89±0.34	1.18±0.09
29	J133705.4-295111	2.92	**4.0±1.3**	**8.9±1.0**	**3.2±0.6**	**1.1±0.3**	**2.7±0.3**	**1.0±0.2**	3.32±0.33	0.80±0.07
30	J133707.1-295101	0.71	2.8±1.2	**9.2±1.0**	**9.2±0.9**	-	**2.3±0.3**	**2.7±0.3**	3.94±0.32	0.95±0.07
31	J133707.2-294649	1.22	0.1±0.5	1.7±0.5	1.6±0.6	0.3±0.1	**0.9±0.2**	0.4±0.1	0.87±0.18	0.21±0.05
32	J133707.3-295132	0.77	1.1±1.1	**6.2±0.8**	**6.2±0.8**	0.3±0.2	**1.9±0.3**	**2.1±0.2**	2.87±0.31	0.70±0.08
33	J133707.6-294911	3.23	**8.6±1.2**	0.3±0.4	-	0.5±0.2	0.4±0.2	-	1.73±0.24	0.41±0.21
34	J133708.0-295333	4.50	0.0±0.6	1.7±0.5	1.0±0.4	-	**1.0±0.2**	0.7±0.2	1.27±0.20	0.31±0.04
35	J133708.8-295235	1.43	**11.0±1.2**	1.1±0.5	0.1±0.3	**1.3±0.3**	-	-	2.36±0.26	0.56±0.06
36	J133712.5-295151	3.58	-	0.3±0.4	0.3±0.3	0.2±0.2	0.5±0.2	**1.0±0.2**	1.26±0.23	0.31±0.06
37	J133716.3-294937	0.65	**6.2±0.9**	**8.2±0.9**	**8.0±0.9**	0.6±0.2	**2.7±0.3**	**2.8±0.3**	4.40±0.31	1.06±0.07
38	J133717.2-295153	1.14	**6.5±0.9**	**2.8±0.6**	1.1±0.4	**1.1±0.2**	0.6±0.2	-	1.68±0.21	0.40±0.06
39	J133719.4-295709	1.09	**3.7±0.8**	**3.5±0.7**	**2.2±0.6**	0.7±0.2	**1.0±0.2**	**0.8±0.2**	1.83±0.24	0.44±0.06
40	J133719.8-295347	0.52	**131.8±3.5**	**86.3±2.8**	**37.5±1.9**	**24.8±0.8**	**24.3±0.8**	**10.4±0.5**	47.10±0.93	11.36±0.23

Key: As for Table A.1.

BIBLIOGRAPHY

Ballet J., 2006, Advances in Space Research, 37, 1902

Bauer M., Pietsch W., Trinchieri G., Breitschwerdt D., Ehle M., Freyberg M. J., Read A. M., 2008, *A&A* , 489, 1029

Bautz M., Suzaku Team 2006, in Bulletin of the American Astronomical Society Vol. 38 of Bulletin of the American Astronomical Society, Early Results from Suzaku: Broadband X-ray Spectroscopy of Galaxies and Clusters of Galaxies. pp 109–+

Bogdán Á., Gilfanov M., 2008, *MNRAS* , 388, 56

Bohlin R. C., Savage B. D., Drake J. F., 1978, *ApJ* , 224, 132

Borkowski K. J., Rho J., Reynolds S. P., Dyer K. K., 2001, *ApJ* , 550, 334

Bowyer S., Byram E. T., Chubb T. A., Friedman H., 1964, Science, 146, 912

Bregman J. N., 1980, *ApJ* , 237, 681

Bresolin F., 2007, *ApJ* , 656, 186

Bresolin F., Garnett D. R., Kennicutt Jr. R. C., 2004, *ApJ* , 615, 228

Burbidge G. R., 1956, *ApJ* , 124, 416

Burrows D. N., Hill J. E., Nousek J. A., Wells A. A., Short A. T., Ambrosi R. M., Chincarini G., Citterio O., Tagliaferri G., 2003, in Truemper J. E., Tananbaum H. D., eds, Society of Photo-Optical Instrumentation Engineers (SPIE) Conference Series Vol. 4851 of Society of Photo-Optical Instrumentation Engineers (SPIE) Conference Series, Swift x-ray telescope (XRT). pp 1320–1325

Campana S., Moretti A., Lazzati D., Tagliaferri G., 2001, *ApJL* , 560, L19

Cardelli J. A., Clayton G. C., Mathis J. S., 1989, *ApJ* , 345, 245

Carpano S., Wilms J., Schirmer M., Kendziorra E., 2005, *A&A* , 443, 103

Cerviño M., Mas-Hesse J. M., Kunth D., 2002, *A&A* , 392, 19

Chevalier R. A., Clegg A. W., 1985, *Nature*, 317, 44

Colbert E. J. M., Heckman T. M., Ptak A. F., Strickland D. K., Weaver K. A., 2004, *ApJ* , 602, 231

Corbelli E., Salucci P., 2000, *MNRAS* , 311, 441

Cox D. P., Smith B. W., 1974, *ApJL* , 189, L105+

Crockett N. R., Garnett D. R., Massey P., Jacoby G., 2006, *ApJ* , 637, 741

Dahlem M., Weaver K. A., Heckman T. M., 1998, *ApJS* , 118, 401

Davidge T. J., 1998, *ApJ* , 497, 650

de Korte P. A. J., Bleeker J. A. M., McKechnie S. P., den Boggende A. J. F., Brinkman A. C., Gronenschild E. H. B. M., Branduardi-Raymont G., Culhane J. L., Mason I., 1981, Space Science Reviews, 30, 495

de Vaucouleurs G., de Vaucouleurs A., Corwin H. G., 1991, Third Reference Catalogue of Bright Galaxies. Volume 1-3, XII, 2069 pp. 7 figs.. Springer-Verlag Berlin Heidelberg New York

Dewangan G. C., Griffiths R. E., Choudhury M., Miyaji T., Schurch N. J., 2005, *ApJ* , 635, 198

Dickey J. M., Lockman F. J., 1990, *ARA&A* , 28, 215

Doane N. E., Sanders W. T., Wilcots E. M., Juda M., 2004, *AJ* , 128, 2712

Done C., Gierliński M., Kubota A., 2007, *A&AR*, 15, 1

Dubus G., Charles P. A., Long K. S., Hakala P. J., 1997, *ApJL* , 490, L47+

Dufour R. J., Talbot Jr. R. J., Jensen E. B., Shields G. A., 1980, *ApJ* , 236, 119

Ehle M., Pietsch W., Beck R., 1995, *A&A* , 295, 289

Ehle M., Pietsch W., Beck R., Klein U., 1998, *A&A* , 329, 39

Fabbiano G., 1989, *ARA&A* , 27, 87

Fabbiano G., 2006, *ARA&A* , 44, 323

Fabbiano G., Feigelson E., Zamorani G., 1982, *ApJ* , 256, 397

Fabbiano G., Trinchieri G., 1987, *ApJ* , 315, 46

Feldmeier J. J., Ciardullo R., Jacoby G. H., 1997, *ApJ* , 479, 231

Foschini L., Rodriguez J., Fuchs Y., Ho L. C., Dadina M., Di Cocco G., Courvoisier T. J.-L., Malaguti G., 2004, *A&A* , 416, 529

Fraternali F., Cappi M., Sancisi R., Oosterloo T., 2002, *ApJ* , 578, 109

Freedman W. L., Madore B. F., Gibson B. K., Ferrarese L., Kelson D. D., Sakai S., Mould J. R., Kennicutt Jr. R. C., et al. 2001, *ApJ* , 553, 47

Fujimoto R., Ishida M., 1997, *ApJ* , 474, 774

Fukazawa Y., Iyomoto N., Kubota A., Matsumoto Y., Makishima K., 2001, *A&A* , 374, 73

Giacconi R., Kellogg E., Gorenstein P., Gursky H., Tananbaum H., 1971, *ApJL* , 165, L27+

Giacconi R., Rosati P., Tozzi P., Nonino M., 2001, ApJ, 551, 624

Giacconi R. e. a., 1979, *ApJ* , 230, 540

Gil de Paz A., Boissier S., Madore B. F., Seibert M., Joe Y. H., Boselli A., Wyder T. K., Thilker D., et al. 2007, *ApJS* , 173, 185

Gilfanov M., Grimm H.-J., Sunyaev R., 2004, *MNRAS* , 347, L57

Goad M. R., Roberts T. P., Reeves J. N., Uttley P., 2006, *MNRAS* , 365, 191

Grimes J. P., Heckman T., Strickland D., Ptak A., 2005, *ApJ* , 628, 187

Grimm H.-J., Gilfanov M., Sunyaev R., 2003, *MNRAS* , 339, 793

Grimm H.-J., McDowell J., Zezas A., Kim D.-W., Fabbiano G., 2005, *ApJS* , 161, 271

Grimm H.-J., McDowell J., Zezas A., Kim D.-W., Fabbiano G., 2007, *ApJS* , 173, 70

Grindlay J. E., Hong J., Zhao P., Laycock S., van den Berg M., Koenig X., Schlegel E. M., Cohn H. N., Lugger P. M., Rogel A. B., 2005, *ApJ* , 635, 920

Haberl F., Geppert U., Aschenbach B., Hasinger G., 2006, *A&A* , 460, 811

Haberl F., Pietsch W., 2001, *A&A* , 373, 438

Hasinger G., Altieri B., Arnaud M., Barcons X., Bergeron J., Brunner H., Dadina M., Dennerl K., et al. 2001, *A&A* , 365, L45

Helfand D. J., Moran E. C., 2001, *ApJ* , 554, 27

Hippelein H., Haas M., Tuffs R. J., Lemke D., Stickel M., Klaas U., Völk H. J., 2003, *A&A* , 407, 137

Ho L. C., Filippenko A. V., Sargent W. L. W., 1997, *ApJS* , 112, 315

Immler S., 2003, in Li X. D., Trimble V., Wang Z. R., eds, High Energy Processes and Phenomena in Astrophysics Vol. 214 of IAU Symposium, X-Ray Emission from Young Supernovae. pp 113–+

Immler S., Vogler A., Ehle M., Pietsch W., 1999, *A&A* , 352, 415

Irwin J. A., Athey A. E., Bregman J. N., 2003, *ApJ* , 587, 356

Jenkins L. P., Roberts T. P., Warwick R. S., Kilgard R. E., Ward M. J., 2005, *MNRAS* , 357, 401

Kaaret P., Corbel S., Prestwich A. H., Zezas A., 2003, Science, 299, 365

Kaastra J. S., Paerels F. B. S., Durret F., Schindler S., Richter P., 2008, Space Science Reviews, 134, 155

Kahn S. M., Seward F. D., Chlebowski T., 1984, *ApJ* , 283, 286

Kennicutt Jr. R. C., 1989, *ApJ* , 344, 685

Kennicutt Jr. R. C., 1998, *ARA&A* , 36, 189

Kilgard R. E., Cowan J. J., Garcia M. R., Kaaret P., Krauss M. I., McDowell J. C., Prestwich A. H., Primini F. A., Stockdale C. J., Trinchieri G., Ward M. J., Zezas A., 2005, *ApJS* , 159, 214

Kim D.-W., Fabbiano G., 2004, *ApJ* , 611, 846

King A. R., Davies M. B., Ward M. J., Fabbiano G., Elvis M., 2001, *ApJL* , 552, L109

Kohno K., Kawabe R., Tosaki T., Okumura S. K., 1996, *ApJL* , 461, L29+

Kong A., di Stefano R., 2006, in Meurs E. J. A., Fabbiano G., eds, Populations of High Energy Sources in Galaxies Vol. 230 of IAU Symposium, Ultra-luminous Supersoft X-ray Sources in Nearby Galaxies. pp 282–286

Kong A. K. H., 2003, *MNRAS* , 346, 265

Körding E., Falcke H., Markoff S., 2002, *A&A* , 382, L13

Krauss M. I., Kilgard R. E., Garcia M. R., Roberts T. P., Prestwich A. H., 2005, *ApJ* , 630, 228

Kreykenbohm I., Wilms J., Kretschmar P., Torrejón J. M., Pottschmidt K., Hanke M., Santangelo A., Ferrigno C., Staubert R., 2008, *A&A* , 492, 511

Kuntz K. D., Snowden S. L., Pence W. D., Mukai K., 2003, *ApJ* , 588, 264

Leitherer C., Heckman T. M., 1995, *ApJS* , 96, 9

Leonard D. C., Filippenko A. V., Li W., Matheson T., Kirshner R. P., Chornock R., Van Dyk S. D., Berlind P., Calkins M. L., Challis P. M., Garnavich P. M., Jha S., Mahdavi A., 2002, *AJ* , 124, 2490

Liu C. Z., Li T. P., 2004, *ApJ* , 611, 1084

Liu Q. Z., Mirabel I. F., 2005, *A&A* , 429, 1125

Long K. S., Charles P. A., Blair W. P., Gordon S. M., 1996, *ApJ* , 466, 750

Long K. S., Dodorico S., Charles P. A., Dopita M. A., 1981, *ApJL* , 246, L61

Long K. S., Helfand D. J., 1979, *ApJL* , 234, L77

Madau P., Rees M. J., 2001, *ApJL* , 551, L27

Makishima K., Mihara T., Ishida M., Ohashi T., Sakao T., Tashiro M., Tsuru T., Kii T., Makino F., Murakami T., Nagase F., Tanaka Y., Kunieda H., Tawara Y., Kitamoto S., Miyamoto S., Yoshida A., Turner M. J. L., 1990, *ApJL* , 365, L59

Markert T. H., Rallis A. D., 1983, *ApJ* , 275, 571

Marston A. P., Elmegreen D., Elmegreen B., Forman W., Jones C., Flanagan K., 1995, *ApJ* , 438, 663

Mas-Hesse J. M., Otí-Floranes H., Cerviño M., 2008, *A&A* , 483, 71

Mason K. O. e. a., 2001, *A&A* , 365, L36

Mathewson D. S., Ford V. L., Dopita M. A., Tuohy I. R., Long K. S., Helfand D. J., 1983, *ApJS* , 51, 345

Mewe R., Lemen J. R., van den Oord G. H. J., 1986, *A&AS* , 65, 511

Miller J. M., 2005, *APSS*, 300, 227

Misanovic Z., Pietsch W., Haberl F., Trinchieri G., Ehle M., Hatzidimitriou D., 2006, in Meurs E. J. A., Fabbiano G., eds, Populations of High Energy Sources in Galaxies Vol. 230 of IAU Symposium, XMM-Newton survey of the Local Group galaxy M33 bright individual sources. pp 162–163

Miyamoto S., Kitamoto S., 2001, X-ray Astronomy: Stellar Endpoints, AGN, and the Diffuse X-ray Background, 599, 786

Morrison R., McCammon D., 1983, *ApJ* , 270, 119

Morrissey P., Conrow T., Barlow T. A., Small T., Seibert M., Wyder T. K., Budavári T., Arnouts S., et al. 2007, *ApJS* , 173, 682

Muñoz-Mateos J. C., Gil de Paz A., Boissier S., Zamorano J., Jarrett T., Gallego J., Madore B. F., 2007, *ApJ* , 658, 1006

Mukai K., 2003, Advances in Space Research, 32, 2067

Norman C. A., Ikeuchi S., 1989, *ApJ* , 345, 372

Okada K., Mitsuda K., Dotani T., 1997, *PASJ*, 49, 653

Owen R. A., Warwick R. S., 2009, *MNRAS* , 394, 1741

Palumbo G. G. C., Fabbiano G., Trinchieri G., Fransson C., 1985, *ApJ* , 298, 259

Patnaude D. J., Fesen R. A., 2007, *AJ* , 133, 147

Pence W. D., Snowden S. L., Mukai K., Kuntz K. D., 2001, *ApJ* , 561, 189

Pietsch W., Misanovic Z., Haberl F., Hatzidimitriou D., Ehle M., Trinchieri G., 2004, *A&A* , 426, 11

Pietsch W., Roberts T. P., Sako M., Freyberg M. J., Read A. M., Borozdin K. N., Branduardi-Raymont G., Cappi M., Ehle M., Ferrando P., Kahn S. M., Ponman T. J., Ptak A., Shirey R. E., Ward M., 2001, *A&A* , 365, L174

Pietsch W., Truemper J., 1993, Advances in Space Research, 13, 171

Prestwich A. H., Irwin J. A., Kilgard R. E., 2003, ApJ, 595, 719

Ranalli P., Comastri A., Setti G., 2003, *A&A* , 399, 39

Read A. M., Pietsch W., 2001, *A&A* , 373, 473

Read A. M., Ponman T. J., Strickland D. K., 1997, MNRAS, 286, 626

Revnivtsev M., Churazov E., Sazonov S., Forman W., Jones C., 2007, *A&A* , 473, 783

Revnivtsev M., Churazov E., Sazonov S., Forman W., Jones C., 2008, *A&A* , 490, 37

Revnivtsev M., Vikhlinin A., Sazonov S., 2007, *A&A* , 473, 857

Roberts T. P., 2007, *APSS*, 311, 203

Roberts T. P., Warwick R. S., Ward M. J., Goad M. R., Jenkins L. P., 2005, *MNRAS* , 357, 1363

Rosa-González D., Burgarella D., Nandra K., Kunth D., Terlevich E., Terlevich R., 2007, *MNRAS* , 379, 357

Rosati P., Tozzi P., Giacconi R., Gilli R., Hasinger G., Kewley L., Mainieri V., Nonino M., Norman C., Szokoly G., Wang J. X., Zirm A., Bergeron J., Borgani S., Gilmozzi R., Grogin N., Koekemoer A., Schreier E., Zheng W., 2002, *ApJ* , 566, 667

Sarazin C. L., Irwin J. A., Bregman J. N., 2000, *ApJL* , 544, L101

Sazonov S., Revnivtsev M., Gilfanov M., Churazov E., Sunyaev R., 2006, *A&A* , 450, 117

Schreier E., Levinson R., Gursky H., Kellogg E., Tananbaum H., Giacconi R., 1972, *ApJL* , 172, L79+

Schulman E., Bregman J. N., 1995, *ApJ* , 441, 568

Seward F. D., Charles P. A., 1995, Exploring the X-Ray Universe

Shapiro P. R., Field G. B., 1976, *ApJ* , 205, 762

Shostak G. S., van der Kruit P. C., 1984, *A&A* , 132, 20

Sivakoff G. R., Sarazin C. L., Irwin J. A., 2003, *ApJ* , 599, 218

Soria R., Kong A. K. H., 2002, *ApJL* , 572, L33

Soria R., Pian E., Mazzali P. A., 2004, *A&A* , 413, 107

Soria R., Wu K., 2002, *A&A* , 384, 99

Soria R., Wu K., 2003, *A&A* , 410, 53

Stark A. A., Gammie C. F., Wilson R. W., Bally J., 1992, ApJS, 79, 77

Stauffer J. R., 1982, *ApJ* , 262, 66

Stewart G. C., Fabian A. C., Terlevich R. J., Hazard C., 1982, *MNRAS* , 200, 61P

Strüder L., Briel U., Dennerl K., Hartmann R., 2001, A&A, 365, L18

Strickland D. K., Heckman T. M., Colbert E. J. M., Hoopes C. G., Weaver K. A., 2004a, *ApJS* , 151, 193

Strickland D. K., Heckman T. M., Colbert E. J. M., Hoopes C. G., Weaver K. A., 2004b, *ApJ* , 606, 829

Strickland D. K., Heckman T. M., Weaver K. A., Dahlem M., 2000, *AJ* , 120, 2965

Strickland D. K., Stevens I. R., 1998, *MNRAS* , 297, 747

Suchkov A. A., Balsara D. S., Heckman T. M., Leitherer C., 1994, *ApJ* , 430, 511

Swartz D. A., Ghosh K. K., Tennant A. F., Wu K., 2004, *ApJS* , 154, 519

Takahashi H., Okada Y., Kokubun M., Makishima K., 2004, *ApJ* , 615, 242

Talbot Jr. R. J., Jensen E. B., Dufour R. J., 1979, *ApJ* , 229, 91

Tennant A. F., Wu K., Ghosh K. K., Kolodziejczak J. J., Swartz D. A., 2001, *ApJL* , 549, L43

Terashima Y., Ptak A., Fujimoto R., Itoh M., Kunieda H., Makishima K., Serlemitsos P. J., 1998, *ApJ* , 496, 210

Terashima Y., Wilson A. S., 2004, *ApJ* , 601, 735

Thim F., Tammann G. A., Saha A., Dolphin A., Sandage A., Tolstoy E., Labhardt L., 2003, *ApJ* , 590, 256

Trinchieri G., Fabbiano G., Paulumbo G. G. C., 1985, *ApJ* , 290, 96

Trinchieri G., Fabbiano G., Peres G., 1988, *ApJ* , 325, 531

Trudolyubov S., Kotov O., Priedhorsky W., Cordova F., Mason K., 2005, *ApJ* , 634, 314

Trümper J. E., 1991, New York Academy Sciences Annals, 647, 141

Tsunemi H., Kitamoto S., Manabe M., Miyamoto S., Yamashita K., Nakagawa M., 1989, *PASJ*, 41, 391

Tsunemi H., Kitamoto S., Okamura S., Roussel-Dupre D., 1989, *ApJL* , 337, L81

Tucker W. H., 1977, Radiation processes in astrophysics.

Tully R. B., 1974, *ApJS* , 27, 449

Turner M. J. L., Abbey A., Arnaud M., Balasini M., 2001, A&A, 365, L27

Turolla R., Mucciarelli P., Zampieri L., Falomo R., Chieregato M., Treves A., 2006, Advances in Space Research, 38, 1374

Tyler K., Quillen A. C., LaPage A., Rieke G. H., 2004, *ApJ* , 610, 213

Urbaneja M. A., Herrero A., Bresolin F., Kudritzki R.-P., Gieren W., Puls J., Przybilla N., Najarro F., Pietrzyński G., 2005, *ApJ* , 622, 862

van den Bergh S., 1991, *PASP*, 103, 609

van der Klis M., 1989, *ARA&A* , 27, 517

Vogler A., Madden S. C., Beck R., Lundgren A. A., Sauvage M., Vigroux L., Ehle M., 2005, *A&A* , 441, 491

Vogler A., Pietsch W., 1996, *A&A* , 311, 35

Vogler A., Pietsch W., Kahabka P., 1996, *A&A* , 305, 74

Volonteri M., Haardt F., Madau P., 2003, *ApJ* , 582, 559

Warwick R. S., Jenkins L. P., Read A. M., Roberts T. P., Owen R. A., 2007, *MNRAS* , 376, 1611

Watson M. G., Schröder A. C., Fyfe D., Page C. G., Lamer G., Mateos S., Pye J., Sakano M., et al. 2009, *A&A* , 493, 339

Watson M. G., Stanger V., Griffiths R. E., 1984, *ApJ* , 286, 144

Weaver K. A., Heckman T. M., Dahlem M., 2000, *ApJ* , 534, 684

Weisskopf M. C., Tananbaum H. D., Van Speybroeck L. P., O'Dell S. L., 2000, in Truemper J. E., Aschenbach B., eds, Society of Photo-Optical Instrumentation Engineers (SPIE) Conference Series Vol. 4012 of Society of Photo-Optical Instrumentation Engineers (SPIE) Conference Series, Chandra X-ray Observatory (CXO): overview. pp 2–16

Williams R. M., Chu Y.-H., Dickel J. R., Gruendl R. A., Shelton R., Points S. D., Smith R. C., 2004, *ApJ* , 613, 948

Wilson C. D., Matthews B. C., 1995, *ApJ* , 455, 125

Wilson C. D., Scoville N., Madore B. F., Sanders D. B., Freedman W. L., 1988, *ApJ* , 333, 611

Yang Y., Li B., Wilson A. S., Reynolds C. S., 2007, *ApJ* , 660, 1106

Young A. J., Wilson A. S., Mundell C. G., 2002, *ApJ* , 579, 560

Zaritsky D., Elston R., Hill J. M., 1989, *AJ* , 97, 97